POLITECNICO DI TORINO

Collegio di Ingegneria Meccanica

Master's Degree in
Mechanical Engineering

Master's Degree Thesis

Passive exoskeleton for assistance in heavy operation

Supervisors
Prof. Carlo Ferraresi
Prof. Roque J. Saltaren Pazmiño
Dr. Giovanni G. Muscolo

Candidate
Mattia Vincenzo
Lo Piccolo

July 2019

Abstract

Passive exoskeletons for industry are devices that can effectively facilitate the work performed by the wearer. One of the limitations of existing structures, used in various application fields, is not to correctly respond to normal human physiological movement, given by the non-direct correlation between robotic and human degrees of freedom. This generates discomfort, non-linear movements and often injury. To solve this problem, models based on shoulder rhythm have been presented and developed, focusing on a supporting exoskeleton for heavy operations of the upper limb member.

Several geometric models have been proposed that are able to recover the potential energy of the movement of the arm with respect to its reference position (non-activated muscular system and arms parallel to the gravity vector). The first model involves the use of a space cam system, that involves the use of compression springs, for which the law of motion was sought for the most suitable target. The remaining two models have been simplified, covering different ranges of movement with respect to the global mobility range of the arm. These models exploit the elastic energy of a pressurized fluid through the use of pneumatic muscles (McKibben muscle).

The strategy adopted was to study the natural dynamics of the shoulder and develop the energy needed to provide assistance during the flexion and abduction phases so as to reduce the metabolic consumption required by the muscles during the manipulation phases in the arm's working space, with the aim of creating an ergonomically better working condition.

A test bench was run for models involving the use of McKibben muscles in order to assess the true functioning characteristic and muscle losses.

Contents

List of Figures

List of Tables

Chapter 1

Introduction

Over the past two decades, robotic exoskeletons have been developed for the upper member for many applications ranging from heavy and light lifting, haptic and fundamental reserch of aptic devices [22], bilateral tele-robotics [4], rehabilitation and physical robotic therapy [21] and military and defense applications [33]. For the superior member, in particular, there are different categories of exoskeletons that serve as support to provide physical therapy sessions in the clinical setting, rehabilitation cases, in controlled environments such as a physiotherapy clinic. Some of these are designed to allow movement to patients who have completely lost their mobility, patients paralyzed for life. In these cases, the exoskeleton is often able to partially replace the lost human movements, and they must guarantee sufficient control to allow the full stability and safety of the user. Any type of wearable robot must have specific characteristics interfacing with the human user, in particular the main requirements it must have are safety, comfort and simple human-machine interaction[23]. Unlike the security and human-robot interaction that have been extensively discussed and become increasingly popular in the field of robotic research [28], investigations into the influence of exoskeletons on the comfort and performance of the operator wearing wearable robotic systems they are not detailed in recent literature[22]. One of the environments that today is taking greater interest is that of exoskeletons designed to assist operators in the industrial sector, allowing them to perform their activities more easily and with longer duration. These devices have been studied mainly of an active form, but the biggest challenge is to reduce their weight and the power absorbed by them. For this reason, exoskeletons are being developed for the upper member, as for the lower one, almost or totally passive to reduce energy consumption [31]. However, most of the devices currently developed are constituted by very rigid structures with numerous mechanical elements such as belts or cue pellets. On the other hand, the user who wears them extends and flexes their biological joints and these "rigid" connections add considerable inertia to the movements which in the case of active structures must be overcome by the power supplied by the electric actuators, or in the case of passive structures by the operator who wears them [31]. In the case of passive structures capable of supporting and facilitating the operator in the movements or in the shifting of weights, these effects still generate considerable natural dynamic impedance of the human body and its kinematics, and thus the metabolic power required for the locomotion. Considering the kinematic aspect of these exoskeletons, the robotic degrees of freedom are not the same as the human bone model due to the biological misalignment that reaches up to

10 cm during normal movement [27], Such misalignments between an exoskeleton and a human joint are inevitable, and can cause major tensions that affect the human limb, causing discomfort, non-linearity in movement or even injury [23]. In literature there are the effects of discomfort caused by devices in which these misalignments have not been considered [18]. In the case of rehabilitative robotics, for example, the misalignments between wearable robots and their users have proved to be responsible for less effective treatment [15] and [19].

To achieve this goal, we aimed at developing a device with sufficient degrees of freedom to allow the structure to adapt to the normal physiological movements of the individual, allowing the device to adapt to human kinematics. A possible solution that is recently being used for the lower limb, and of which prototypes are being developed is that of applying active soft insoles [31], which show great results in reducing the impedance and allowing a more natural movement to the subject who wears it. According to [24] the inclusion of passive compensating joints in the exoskeleton increases the overall working space of the human arm, which is why we have designed a kinematic design that provides passive compensation joints for this offset compensation. In [23] the effects on the subjective comfort of a group of subjects are reported by the presence/absence of passive compensation joints within the mechanical structure of exoskeletons through the indexes of the NASA rating scale TLX, and it results that the best combination of subjective and objective performance for the task can be achieved by an ergonomic exoskeleton with passive compensation joints. In our research line, we aim to develop an exoskeletal assistance device with gravity compensation that is optimally ergonomic for its users. This requirement sitems from the need for the exoskeleton to function as a tactile interface for users in suboptimal locations and assist them in heavy operations. Due to the effect of the arm's position on the shoulder, ergonomists recommend that workers sitting at a desk or table try to position their arms with 20° or less of abduction and 25° or less of flexion while workers who are required to hold their arms in a sustained position over the head for operations that can take a long time, are particularly sensitive to degenerative tendinitis in biceps and supraspinates [13], the glenohumeral joint supports the compressive forces that are estimated to reach 50% of body weight refer to [13]. These elements place very high demands on the compatibility of the device with its operators and on its comfort and ergonomics. Furthermore, an exoskeleton used by operators in the industry should allow rapid clothing and dressing and therefore reduce as much as possible the mechanical adjustments of the limbs in the event of a change in operator size. The project was carried out with the collaboration of the Polytechnic University of Madrid and two solutions will be proposed, elaborated and studied in the two universities. Two elastic active actuation systems are proposed for shoulder joint, to transform the potential energy of the arm during the main movements respect the reference posture of arm (hanging arms, parallel to gravity vector) into potential elastic energy. Kinematic models of shoulder rhythm will be presented, a more evident example of biological unalignment, and kinematic solutions will be proposed for the structure of the exoskeleton, which is therefore intended to provide gait assistance to a healthy individual but could also provide a benefit for those with partially impaired

function. The device consists of rigid links with the load-bearing load constituted by the skeletal-muscular complex of the individual allowing the transfer of the load. Models are proposed that do not want to significantly limit the wearer's movements. The strategy employed is to exploit the natural dynamics associated with the movement of the shoulder, arm and forearm by integrating a small amount of energy accumulated by the extension and adduction operation into normal positive muscle work and then returning it to the flexion and abduction phase. In particular, assuming to be able to invert the energy given by the own weight of the arm and to return it during the phase of greater effort, flexion and abduction it is possible to provide assistance to the locomotion and to reduce the metabolic cost required by the muscles both in the handling and maintenance phases in a position fixed in the space by the arm. For the rest of this document, we outline the actuator requirements for the exoskeleton, and therefore propose a redirection of the force that provides assistance implementation through a system consisting of compression springs and a drum cam that shapes the force and the moment associated with it, the second one instead based on the use of McKibben pneumatic muscles, that exploit the elastic energy of a fluid under pressure contained in deformable membranes, used as tension springs manually reloaded and not directly connected to a compressed air distribution network.

Chapter 2

Biomechanics of human upper limb

2.1 Anatomy of the Shoulder

Among all human joints the shoulder appears to be the most complex articulation of the human body, mainly because it is composed of five separate joints: the glenohumeral joint, the sternoclavicular joint, the acromioclavicular joint, the coracoclavicular joint and the scapulothoracic articulation. The glenohumeral joint is the joint between the head of the humerus and the glenoid fossa of the scapula, while the sternoclavicular and acromioclavicular joints provide mobility to the clavicle and scapula, and constitute the bones of the scapular girdl [13] that ensure that agility and dynamism of movement, which are indispensable for daily life activities; the bones of the upper limb are therefore lighter than those of the lower limb, whose primary role is to support the weight of the body and to allow locomotion.

2.1.1 Sternoclavicular Joint

The sternoclavicular joint is composed of the proximal end of the clavicle which is articulated with the clavicular notch of the sternum handlebar and with the cartilage of the first rib [13]. This joint allows the main rotation of the clavicle and scapula (Figure 2.1). The sternoclavicular joint (SC) can be imagined as a modified ball and socket, and allows free movement of the frontal and transverse plane and also allows rotation in the sagittal plane forward and backward. The articular surfaces of the bone possess a fibrocartilaginous articular disc designed to improve the contact surface between the bones and act as a shock absorber [13]. The rotation of SC allows movements such as squeezing the shoulders beyond the head, raising the shoulders and more complex movements such as swimming. During shoulder elevation, once it reaches its maximum position, the maximum approach position for the SC joint is also reached [13].

2.1.2 Acromioclavicular Joint

The articulation of the acromion of the scapula with the distal end of the clavicle is known as the acromioclavicular joint. It is classified as an irregular articulation of diarthrosis (an articulation involving bony surfaces that slide on cartilage) [13]; The structure of this joint allows limited movement on all three

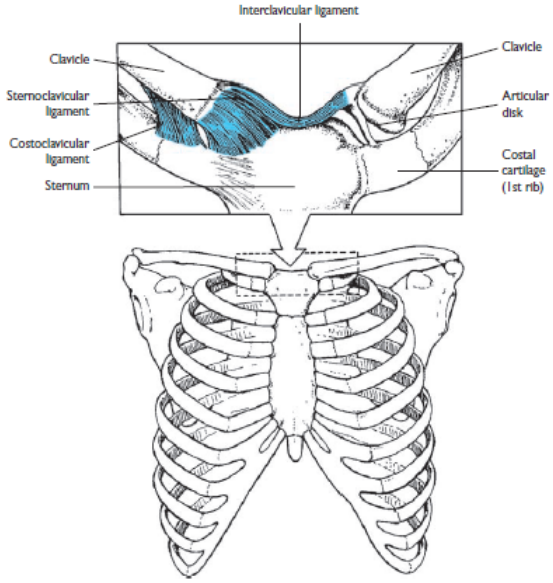

FIGURE 2.1: Human sternoclavicular joint [13]

planes. Anatomically, with respect to different individuals, there is a significant variation in the acromioclavicular joint (AC) and morphologically at least 5 different have been identified [13]. The AC joint rotates during the evasion of the arm in the flexion or abduction phases and the close position of the AC complex occurs when the humerus is abducted at 90° [13].

2.1.3 Coracoclavicular Joint

The coracoclavicular joint is a syndesmosis (a particular type of joint in which the joint cavity and the cartilage lining are missing) [13], formed by the coracoid process of the scapula and the lower surface of the clavicle and are bound together by the coracoclavicular ligament [13]. This articulation allows very small and limited movements. Acromioclavicular and coracoclavicular joints are shown in Figure 2.2.

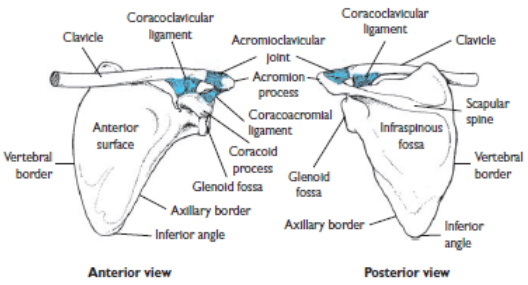

FIGURE 2.2: Human acromiocalvicular and coracoclavicular joint [13]

2.1.4 Glenohumeral Joint

The glenohumeral joint is the joint with more degrees of freedom in the human body and which allows the following movements: flexion, extension, hyperextension, abduction, adduction, horizontal abduction and adduction and medial and lateral rotation of the humerus (Figure 2.3) [13]. The head of the humerus is almost hemispherical and has from three to four times the surface quantity of the superficial glenoid fossa of the scapula with which it articulates. The glenoid fossa has a smaller radius of curvature than the humeral head, thus allowing the humerus to move almost linearly across the surface of the glenoid fossa which also provides ample rotational capacity [13]. The glenoid fossa also has variations in form from person to person; mainly two types of form can be distinguished, an oval (or egg-shaped) cavity in about 45% of the population and a pear-shaped cavity in the remaining 55% [13]. The glenoid fossa is surrounded by the glenoid labrum, a fibro-cartilaginous ring fixed around the margin of the glenoid cavity of the scapula, the tendon of the long head of the brachial biceps and the glenohumeral ligaments. This border of dense collagen tissue has a triangular shape in the cross section and is attached to the periphery of the pit [13]. The labrum deepens the pit and has the task of stabilizing the joint [13]. The capsule surrounding the glenohumeral joint is shown in Figure 2.4 [13]. With the glenohumeral capsule different ligaments are fused, including: the upper, middle and lower glenohumeral ligaments on the anterior side of the joint and the coracohumeral ligament on the upper side. The tendons of four muscles also join the joint capsule. These are known as rotator cuff muscles so called because they form a collagen cuff around the glenohumeral joint and contribute to the rotation of the humerus [13]. Among the main muscles we remember the supraspinatus, infraspinatus and teres minor that participate in the lateral rotation and the subscapularis which contributes to the medial rotation [13]. The muscles of the lateral rotator group exchange the muscle bundles with one another, which increases their ability to rapidly develop tension and functional power [13]. The rotator cuff surrounds the shoulder on the back, top and front sides. The tension in the rotator cuff muscles pulls the humeral head toward the glenoid fossa, contributing significantly to the minimal stability of the joint [13]. The muscles of the rotator cuff and biceps are activated to provide stability to the shoulders before the movement of the humerus; inside the capsule of the glenohumeral joint a negative pressure is generated which helps to stabilize the joint. The joint is more stable in its close position, when the humerus is kidnapped and turned sideways [13].

2.1.5 Scapulothoracic Joint

The scapula can move both in the sagittal plane and in the frontal plane with respect to the trunk and the region between the anterior scapula and the thoracic wall is sometimes referred to as the scapulo-thoracic joint[13]. The muscles that attach to the scapula perform two functions: they can contract to stabilize the shoulder region and can facilitate the movements of the upper limbs through the appropriate positioning of the glenohumeral joint[13].

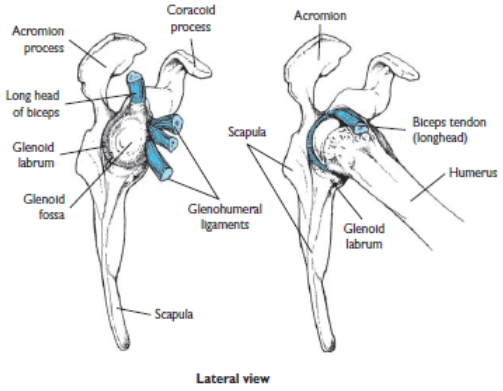

FIGURE 2.3: Human glenohumeral joint [13]

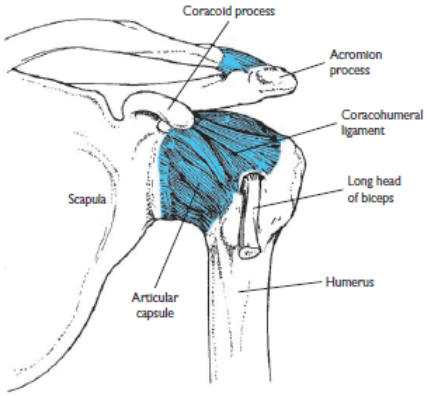

FIGURE 2.4: The capsule surrounding the glenohumeral joint contributes to joint stability [13]

2.1.6 Bursae

In the region of the shoulder there are several small pockets of fiber that secrete a synovial fluid internally similar to that of a joint capsule. These bags, known as bursae, cushion and reduce friction between layers of collagen tissue. The shoulder is surrounded by several bursae, among which are rectchal: subscapular and subcoracoid which are responsible for the management of friction of the superficial fibers of the subscapularis muscle against the scapula neck, the head of the humerus and the coracoid process. Their role is very important as the subscapularis undergoes significant changes in orientation during arm movements on the glenohumeral joint [13]. The subacromial bursae is located in the subacromial space, between the acromion process of the scapula and the coracoacromial ligament (above) and the glenohumeral joint (below), that has the task of cushioning the muscles of the rotator cuff, in particular the supraspinatus, from the overlying acromion of the bone (Figure 2.5) [13].

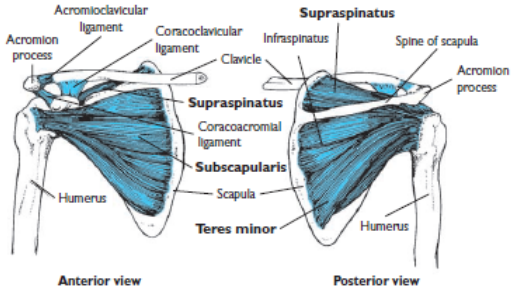

FIGURE 2.5: Muscle of rotatory cuff [13]

2.2 The shoulder complex movements

In general the movement of the humerus involves a movement to all three joints of the shoulder, although it can be verified that, during the glenohumeral movement, some joints remain still. The elevation of the humerus in abduction and flexion is accompanied by a rotation of the scapula of about 55° and represents a part of the entire range of humeral movement[13]. This movement is allowed by an important coordination of scapular and humeral movements, known as scapulo-humeral rhythm, which allows a much wider range of shoulder movement than in the case in which this was fixed. The scapulo-humeral rhythm is discussed and discussed in the next chapter[13].

2.2.1 Muscles of the Scapula

The muscles that attach to the scapula are the levator scapula, the rhomboids, the anterior dentate, the small pectoralis and the sub-cavity and the four parts of the trapezius[13]. In figures 2.6 and 2.7 the directions in which these muscles exert their force on the scapula during their contraction are highlighted. The scapular muscles have two main functions, to stabilize the scapula so that it forms a rigid base for the muscles of the shoulder during the development of the tension that generates strength and to facilitate the movements of the upper limbs by properly positioning the glenohumeral joint[13].

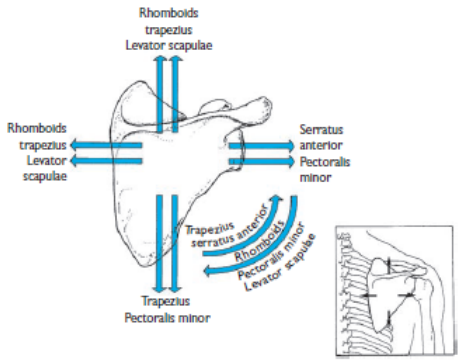

FIGURE 2.6: Actions of scapular muscles [13]

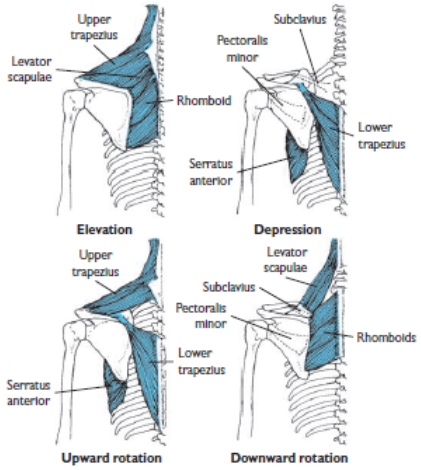

FIGURE 2.7: The muscles of scapula [13]

2.2.2 Muscles of the Glenohumeral Joint

The muscles that pass through the glenohumeral joint are much and, depending on the attachment site, contribute more or less to a generic action of the humerus. Furthermore, due to the wide range of shoulder movement, the action produced by the development of muscle tension can change with the orientation of the humerus[13]. The complexity of the glenohumeral joint structure is very unstable, and part of this instability is compensated by the muscles and tendons that pass through this joint. Furthermore, when one of these muscles develops a certain tension, it is necessary in many cases for an antagonistic tension to develop to prevent dislocation of the joint [13].

2.2.3 Flexion at the Glenohumeral Joint

The muscles that pass through the glenohumeral joint participate in flexion of the shoulder (Figure 2.8). The first muscles activated in the flexion of the shoulder are the anterior deltoid and the clavicular portion of the large pectoralis, then the small coracobrachialis and the short head of the brachial biceps also help the flexion. The long head of the biceps also crosses the shoulder, but is not active only in the movement of the shoulder but produces tension when the elbow and forearm move. Flexibility and joints limitations are shown in the figure 2.10.

2.2.4 Extension at the Glenohumeral Joint

When the shoulder is extended and the arm flexion phase begins, the gravitational force is the main engine with the eccentric contraction of the flexor muscles that take care of controlling slow down the movement [13]. When resistance is present, the contraction of the posterior muscles of the glenohumeral joint, in particular the sternocostal pectoralis, the large dorsalis and the greater teres, extends the humerus [13]. The posterior deltoid helps in the extension, especially when the humerus is rotated externally. The long head of the brachial

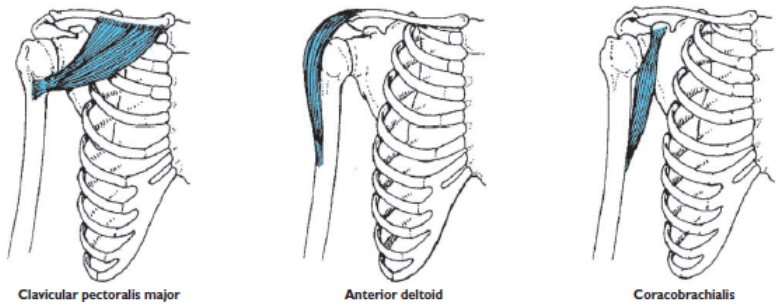

FIGURE 2.8: The major flexor muscles of the shoulder [13]

triceps helps through the elbow and therefore helps the extension, furthermore its contribution is slightly more effective when the elbow is in flexion. The shoulder extenders are shown in Figure 2.9 [13]. Flexibility and joints limitations are shown in the figure 2.10.

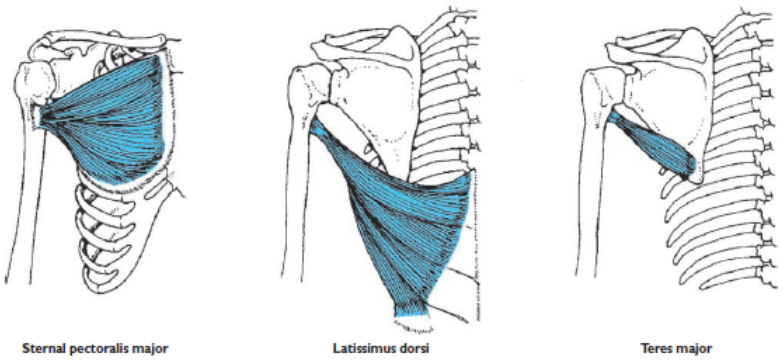

FIGURE 2.9: The major estensor muscles of the shoulder [13]

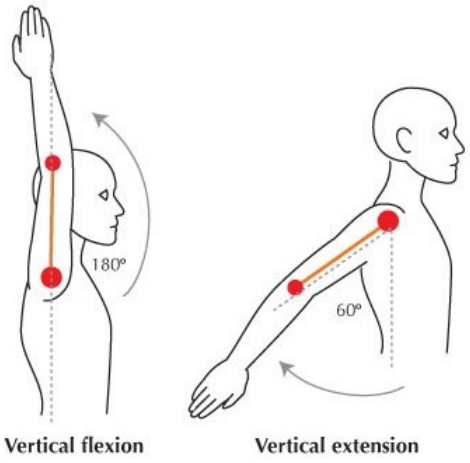

FIGURE 2.10: Glenohumeral movements - Flexion/Extension

2.2.5 Abduction at the Glenohumeral Joint

The main muscles that allow abduction of the humerus are the middle deltoid and the supraspinatus. Both muscles cross the shoulder superior to the glenohumeral joint (Figure 2.11). The supraspinatus has the task of starting the abduction and is activated for the first 110° of movement. Between the 90° and the 180° of abduction the middle deltoid is activated while the infraspinatus, subscapularis and minor teres neutralize the component of superior dislocation of the force produced by the average deltoid. Flexibility and joints limitations are shown in the figure 2.13.

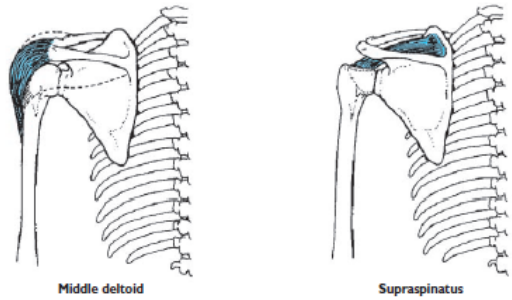

FIGURE 2.11: The major abductor muscles of the shoulder [13]

2.2.6 Adduction at the Glenohumeral Joint

As with the extension of the shoulder, adduction in the absence of resistance derives from the gravitational force while the abductors have the task of controlling the speed of movement [13]. The primary adductors are the granular dorsal, the greater teres and the sternocostal pectoral, which are located on the lower side of the joint [13] (Figure 2.12). The short head of the biceps and the long head of the triceps contribute only minimally, and when the arm is raised above 90°, the coracobrachial muscles and the subscapularis are activated [13]. Flexibility and joints limitations are shown in the figure 2.13.

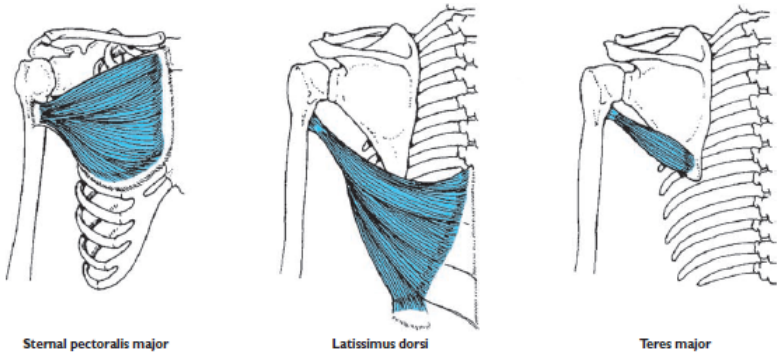

FIGURE 2.12: The major abductor muscles of the shoulder [13]

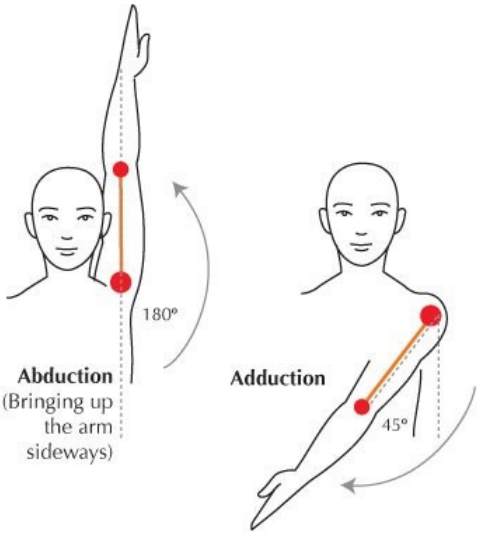

FIGURE 2.13: Glenohumeral movements - Abduction Adduction

2.2.7 Medial and Lateral Rotation of the Humerus

The medial or internal rotation of the humerus is mainly driven by the subscapularis and the greater teres, both attached to the anterior side of the humerus. The principal assistants are the portions of the great pectoralis, of the anterior deltoid, of the large dorsal and of the short head of the biceps brachialis. The muscles that attach to the back side of the humerus, in particular the infraspinatus and the minor teres with the help of the posterior deltoid that produce a lateral or outward rotation.

2.2.8 Horizontal Adduction and Abduction at the Glenohumeral Joint

The horizontal adduction is produced by the anterior articulation muscles, including both the heads of the pectoralis major, the anterior deltoid and the coracobrachialis, while the short head of the brachial biceps assists the movement. The muscles posterior to the articular axis influence the horizontal abduction. The main horizontal abductors are the median and posterior parts of the deltoid, infraspinatus and minor teres, with the assistance provided by the major teres and the large dorsalis. The main horizontal leads and abductors are shown in figures 2.15 and 2.15. Flexibility and joints limitations are shown in the figure 2.16.

2.3 Elbow Anatomy and Biomechanics

The elbow comprises three joints: the humeroulnar, omeroradial and proximal radioulnar joints, but it is often considered as a simple hinged joint. The bone structure of the elbow provides about half of its stability, while the remaining

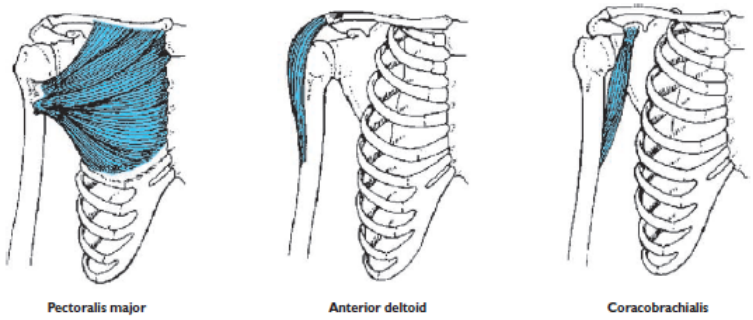

FIGURE 2.14: The major horizontal adductor muscles of the shoulder [13]

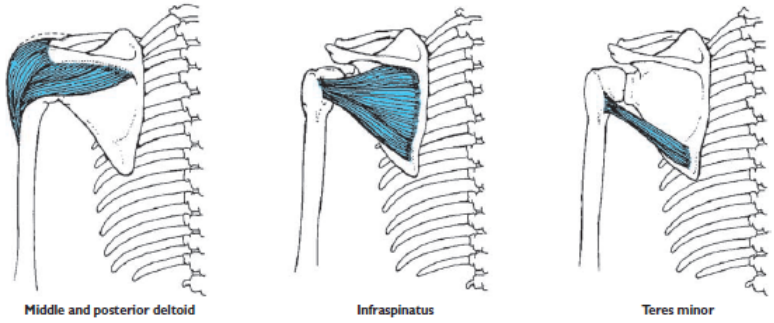

FIGURE 2.15: The major horizontal abductor muscles of the shoulder [13]

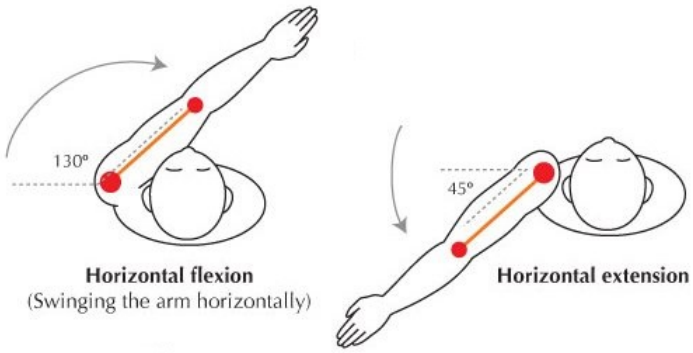

FIGURE 2.16: Glenohumeral movements - The Shoulder

part is compensated by the joint capsule and the ulnar and radial ligaments. [13]

2.3.1 Humeroulnar and Humeroradial Joint

The humeroulnar articulation is the main joint of the elbow considered as a hinge, in particular the ovarian trochlea of the humerus is articulated with the trochlear fossa which has a reciprocal shape to the ulna. In addition to bending and extending the elbow, this joint also allows for slight hyperextension in small quantities. This joint is more stable in extension than flexion. The humeroradial joint is positioned laterally to the humeroulnar joint. The humeral articulation

is classified as a sliding joint, the immediately adjacent humerouline joints restrict the field of motion in the sagittal plane, The humeroulnar articulation and the radial humerus are shown in figure 2.17. [13]

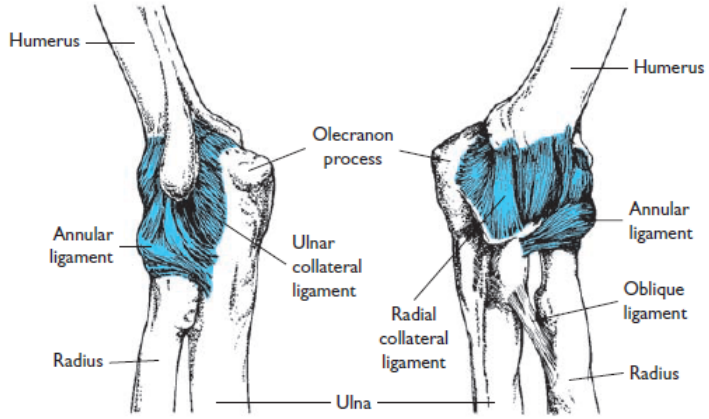

FIGURE 2.17: Human elbow anatomy

2.3.2 Proximal Radioulnar Joint

The proximal radioulnar joint is a pivot joint that allows forearm pronation and supination that occur when the radius rotates medially and laterally on the ulna (Figure 2.18). The nearest position is at 5 degree of supination of the forearm.

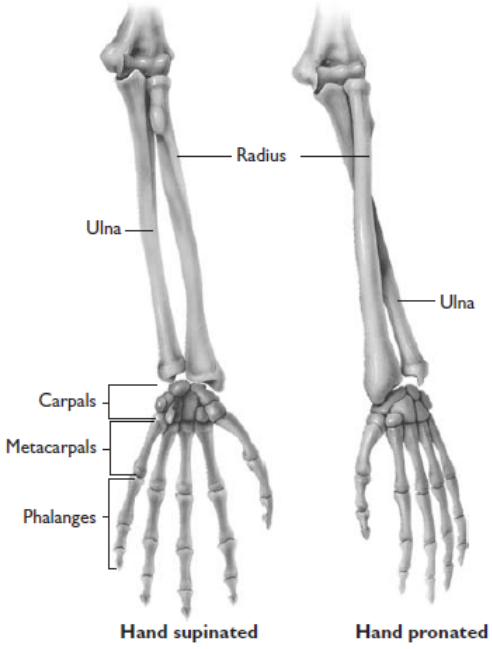

FIGURE 2.18: Bones of the elbow, forearm, wrist, and hand

2.4 Elbow movemets

2.4.1 Elbow Flexion and Extension

The front side of the elbow is crossed by the elbow flexors shown in Figure 2.19. The strongest of these is the brachialis, which is attached to the coronoid process of the ulna. This ligament allows the muscle to be equally effective when the forearm is in supination or pronation. The brachial biceps, both long and short, are attached to the radial tuberosity by a single common tendon; this muscle contributes effectively during flexion of the elbow when the forearm is supinated being slightly stretched. When the forearm is pronated instead, the muscle appears to be less tense and consequently reduces its effectiveness. [13]

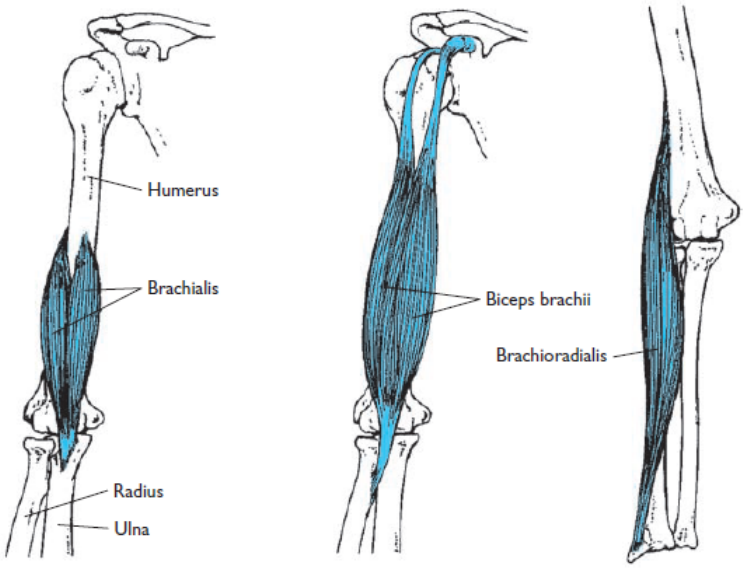

FIGURE 2.19: The major elbow flexors [13]

The brachioradialis, the third muscle that contributes to the elbow flexion, is more effective when the forearm is in a neutral position, as it is attached at the distal level to the base of the styloid process on the lateral radius. In a neutral position, the moss is slightly elongated and the radial attachment is centered in the front part of the elbow joint [13]. The triceps is the major extender of the elbow, which traverses the joint posteriorly (Figures 2.20).

The extension and flexion of the elbow are shown in the figure 2.21.

2.4.2 Elbow Pronation and Supination

Pronation and supination of the forearm are allowed by three radioulnar joints: the proximal, medium and distal radioulnar joints. The proximal and distal joints are considered as pivot joints, whereas the central radioulnar joint is an endomosis connected to an elastic membrane that allows supination and pronation, but blocks the longitudinal displacement of the bones. [13] Figure

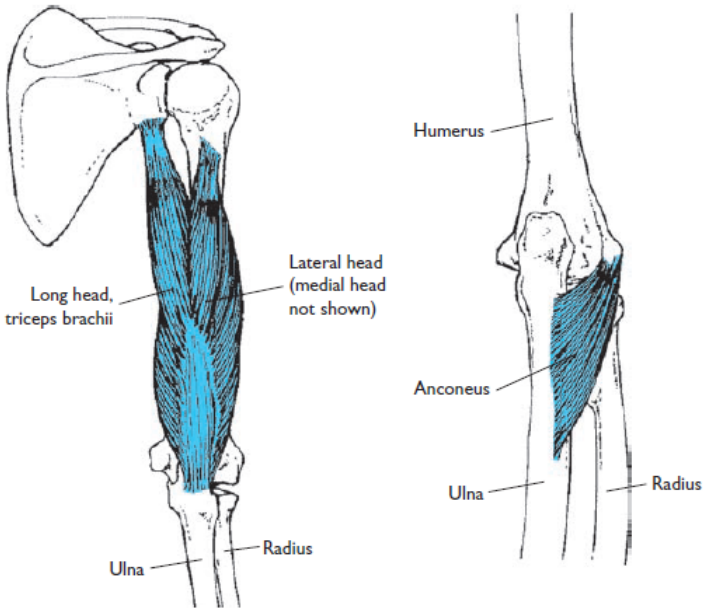

FIGURE 2.20: The major elbow extensor [13]

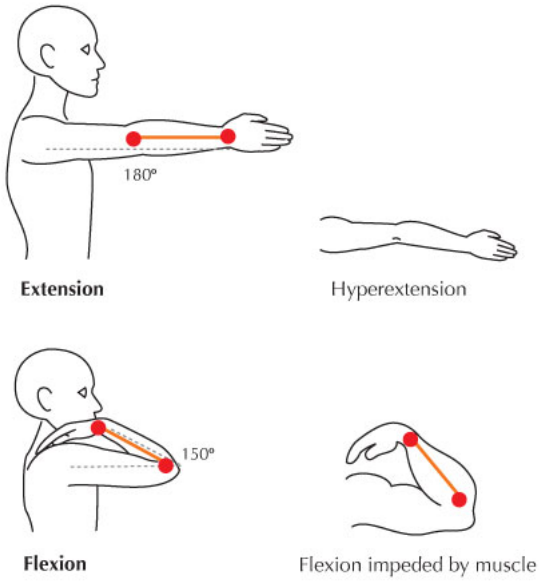

FIGURE 2.21: Human elbow movements

2.22 shows the major pronator, called pronator quadratus, which is connected to the ulna and the distal radius.

The main supinator is instead responsible for supination (Figure 2.23). It is connected to the lateral epicondyle of the humerus and to the lateral proximal third of the radius.

The pronation and supination of the elbow are shown in the figure 2.24.

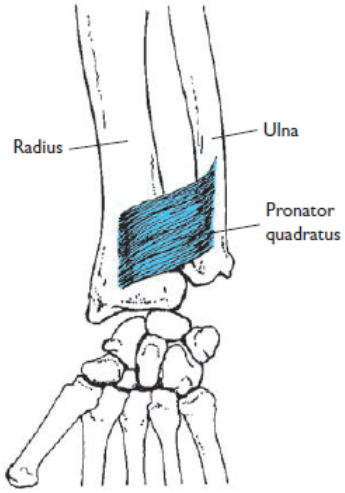

FIGURE 2.22: The major elbow pronator [13]

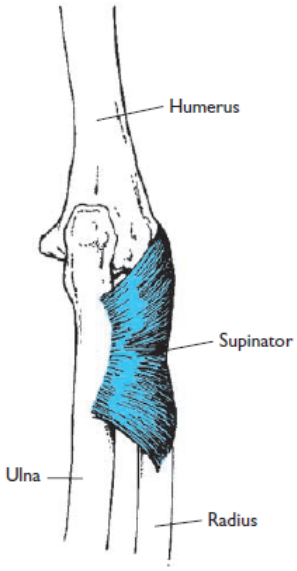

FIGURE 2.23: The major elbow supinator [13]

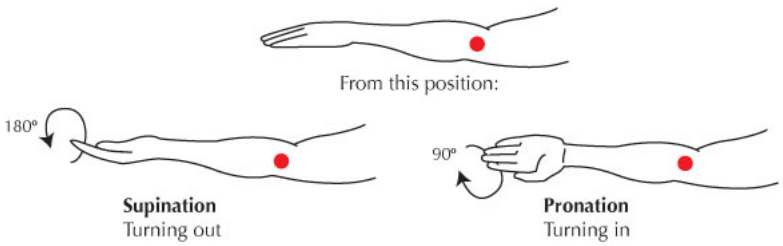

FIGURE 2.24: Human radioulna movements

2.5 Loads on the shoulder

The glenohumeral joint provides direct mechanical support for the arm supporting much greater loads than the other shoulder joints that have function to some extent as units in load-bearing loads and shock absorbers[13]. The weight of body segments is assumed to act on the segmental mass center. The arm of the moment for the entire segment of the arm with respect to the shoulder is therefore the perpendicular distance between the weight vector (which acts on the center of gravity of the arm) and the shoulder. When the elbow is in flexion, the effects of the arm and the segments of the forearm/hand must be analyzed separately [13] (Figure 2.25). Although the weight of the arm represents only about 5% of the body weight, the length of the arm extended horizontally creates large arms of moment of the segment and therefore large pairs due to the gravity that must be contrasted by the muscles of the shoulder. When these muscles contract to support the extended arm, the glenohumeral joint supports the compressive forces that are estimated to reach 50% of body weight [13]. This load is reduced by about half when the elbow is flexed to the maximum due to the shortened arm of the forearm and hand moment.

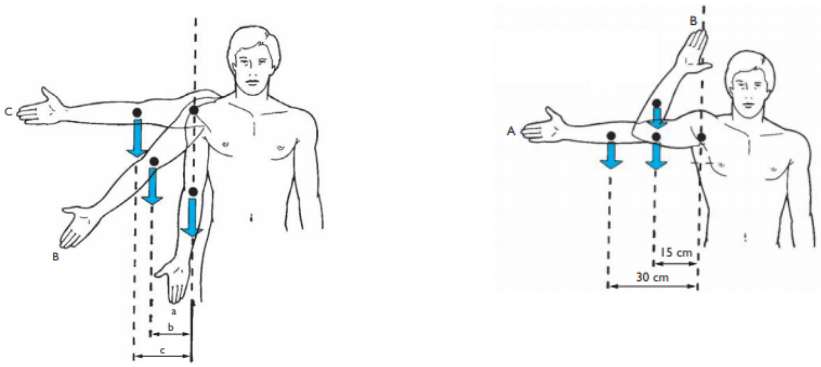

FIGURE 2.25: Variation of center of mass for global arm and moment due to gravity with respect elbow flexion/extension and shoulder arm flexion/extension [13]

The graphs in figure 2.26 show how the center of mass for an individual of halt equal to 1.80m varies considerably during flexion and extension of the forearm (elbow angle θ_2) until it becomes almost zero. The variation of the center of mass was examined in particular in the position of the arm extended to 90° and it is noticed that the peak of the moment generated by the gravitational force varies considerably with the center of mass ($\theta_1 = 90°$ and θ_2 variable between 0° and 150°). This aspect wants to find an implication of the application in the design of the exoskeleton, but above all in the dimensioning of the elastic actuators placed in the shoulder joint able to balance the weight of the arm.

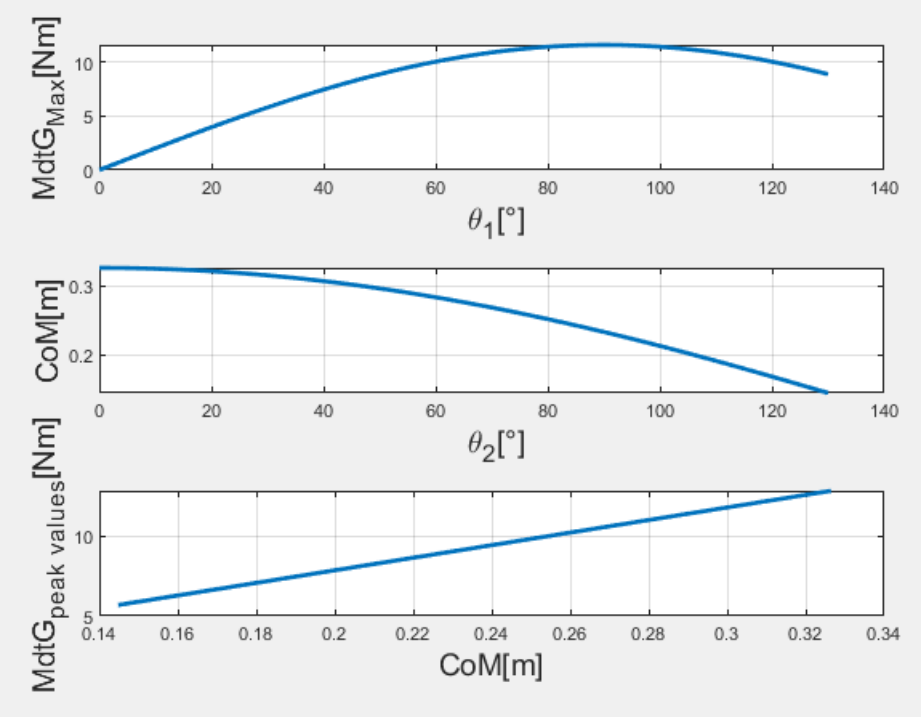

FIGURE 2.26: Human arm gravity extension torque, variation od center of mass (elbow function) and peak values of moment due to gravity

2.6 Shoulder Rhythm

The elevation movement of the humerus arm derives from the rotations of the humerus around the glenohumeral articulation (GH joint), from the rotation of the scapula around the acromioclavicular joint (AC joint) and the rotation of the clavicle around the sternoclavicular joint (SC joint). As a result, for small angles in the glenohumeral motion, the CGH articulation travels in the x and y directions and it deviates for larger motions [14] (Fig. 2.27).

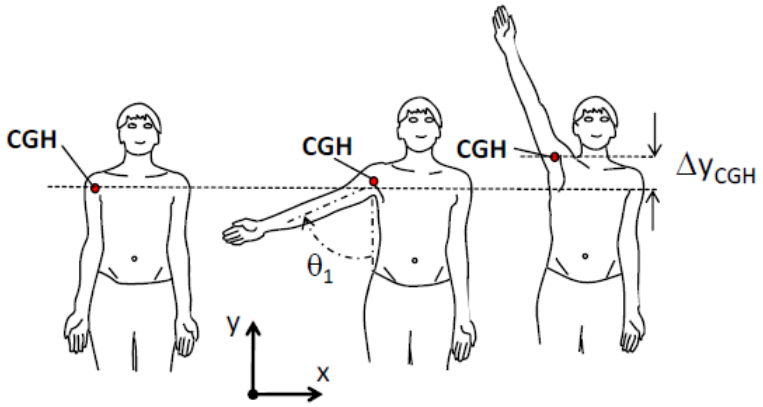

FIGURE 2.27: Location of the center of the glenohumeral joint (CGH) for three different arm elevation angles in the frontal plane [27]

The exoskeleton is fixed by the cuffs to the upper arm and the movement of the CGH center of rotation should be known, but the quantitive description is not simple; the complication is linked to the definition of the exoskeleton structure, this is because it is claimed to follow the natural movement of the CGH joint. In order to allow the development of a general model of movement of the CGH joint, the following simplifications are taken [27]:

- Individuals with the same body size have the same CGH articular movement pattern.
- Training does not affect the movement of the CGH model joint.
- Suppose that man does the movement spontaneously and without conscious control.

This allows to express the relationship between the position of the CGH joint (x_{CGH}; y_{CGH}; z_{CGH}) and the three corners of the humerus (angle of elevation of the arm θ_1, angle of θ_2 of the elevation plane, θ_3 int./est. rotation of the shoulder), the body size h of the human and additional external mass that the arm carries [27], such as:

$$\begin{bmatrix} x_{CGH} \\ y_{CGH} \\ z_{CGH} \end{bmatrix} = \begin{bmatrix} f(\theta_1, \theta_2, \theta_3, h, m_{EXT}) \\ g(\theta_1, \theta_2, \theta_3, h, m_{EXT}) \\ h(\theta_1, \theta_2, \theta_3, h, m_{EXT}) \end{bmatrix} \tag{2.1}$$

The following hypotheses where they were made [27]:

1. The additional external mass (m_{ext} does not affect the position of the scapula [9]
2. The angle θ_3 of the internal/external shoulder rotation does not affect the position of the CGH joint [30]
3. The relative movement of the CGH joint is independent of the angle of the elevation plane θ_2 [8]
4. The lengths of the bone segment are proportional to the size of the body, which makes it possible to formulate the influence of the size of the body as a linear scale factor [32]

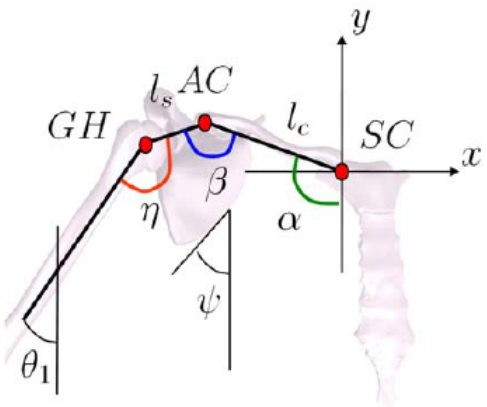

FIGURE 2.28: The human shoulder joint in the frontal plane with the three joint-angles α, β,η the arm elevation angle θ_1 and the tilting angle of the scapula ψ

According to previous hypotheses, the equation 2.1 in the frontal plane (z_{CGH}=0) can be written as [27]:

$$\begin{bmatrix} x_{CGH} \\ y_{CGH} \end{bmatrix} = \begin{bmatrix} f(\theta_1) \\ g(\theta_1) \end{bmatrix} \frac{h}{h_{ref}} = \begin{bmatrix} -l_c cos(\alpha - 90) + l_s sin(\beta + \alpha) \\ l_c sin(\alpha - 90) + l_s cos(\beta + \alpha) \end{bmatrix} \frac{h}{h_{ref}} \tag{2.2}$$

representing instead the displacement of the arm (E) for the generation of the workspace generated by it extension/flexion, the equation 2.2 can be written as

$$\begin{bmatrix} x_E \\ y_E \end{bmatrix} = \begin{bmatrix} -l_c cos(\alpha - 90°) + l_s sin(\beta + \alpha) + l_b sin(\beta + \alpha + \eta) \\ l_c sin(\alpha - 90°) + l_s cos(\beta + \alpha) - l_b sin(\beta + \alpha + \eta) \end{bmatrix} \frac{h}{h_{ref}} \tag{2.3}$$

In equation 2.3, the angles α and β vary with the angle of elevation of the arm θ_1 [27]. To find this relationship [27], the concept of shoulder rhythm [8] or scapular-humeral rhythm is used [9]. In phase 1 ($\theta_1 = [0°; 30°]$), rotation occurs mainly in the GH-joint. In phase 2 ($\theta_1 = [30°; 80°]$), the rotation of the SC rotation around the GH-joint occurs. In phase 3 ($\theta_1 = [80°; 140°]$), the rotation

of the scapula around the AC-joint dominates the movement and phase 4 (θ_1 = [140°; 180°]) is again characterized by a rotation in the articulation GH. The corresponding angles are taken from the literature and presented in table 1 [11], [3], [6] and [27].

TABLE 2.1: Scapulahumeral rhythm ([11], [3], [6] and [27])

θ_1	$\Delta\ \alpha$	$\Delta\ \beta$	$\Delta\ \eta$
0° - 30°	0° - 26°	0°	0°-4°
30°-80°	26°-65°	0°	4°-15°
80°-140°	65°-90°	0°-35°	15°
140°-180°	90°-121°	35°	15°-24°

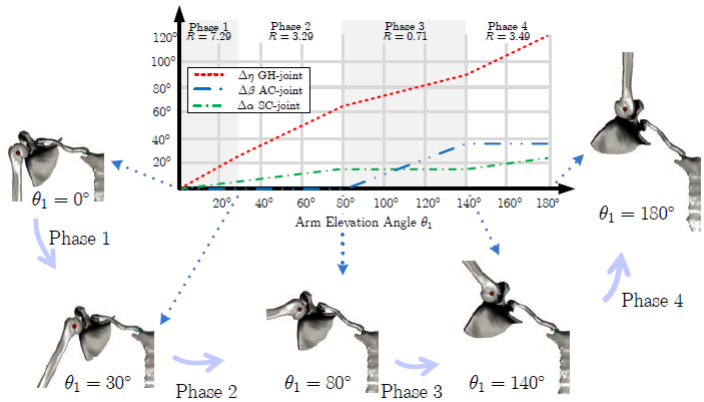

FIGURE 2.29: Four phases of the scapula-humerus rhythm with the graphical representation in the frontal plane [27]

Combining the angular values of table 2.1 [27], assuming a linear behavior between the limits of each corner, with the initial angles (measured in the CT data) [27]:

$$\alpha = \alpha_0 + \Delta\alpha = 99° + \Delta\alpha \tag{2.4}$$

$$\beta = \beta_0 + \Delta\beta = 143° + \Delta\beta \tag{2.5}$$

$$\eta = \eta_0 + \Delta\eta = 118° + \Delta\eta \tag{2.6}$$

Considering a subject with a height (h) of 180 cm (href = 180 cm) and with the lengths of the segment lc = 149,4 mm and ls = 66,8 mm (both measured in the CT data) [27], the movement of the CGH joint it can be derived, using the equation 2.2 [27] and the wrist movement with equation 2.3. Figure 2.30 shows the cartesian coordinates of the CGH during the arm estension or abduction movement.

By implementing the equations in MATLAB environment, it is possible to visualize, besides the CGH displacement of the shoulder center, the work space

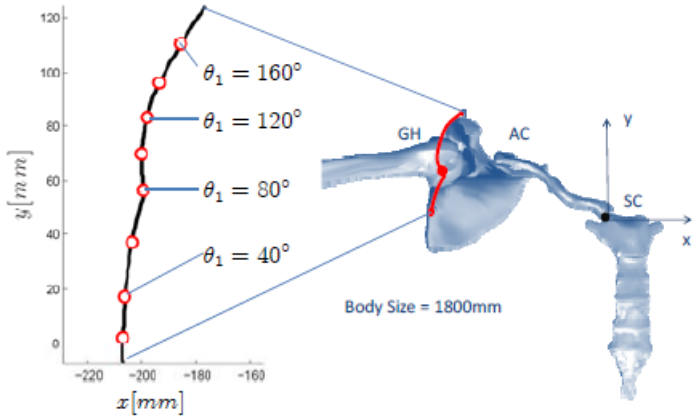

FIGURE 2.30: Movement of the CGH joint during arm elevation [27]

performed by the end-effector considered as the center of the wrist. Given the gleno-homeral shift, it appears that during the extension or abduction phase of the arm, it is able to reach a greater space than that granted by the only extension given by the angle of elevation θ_1 (Fig. 2.31).

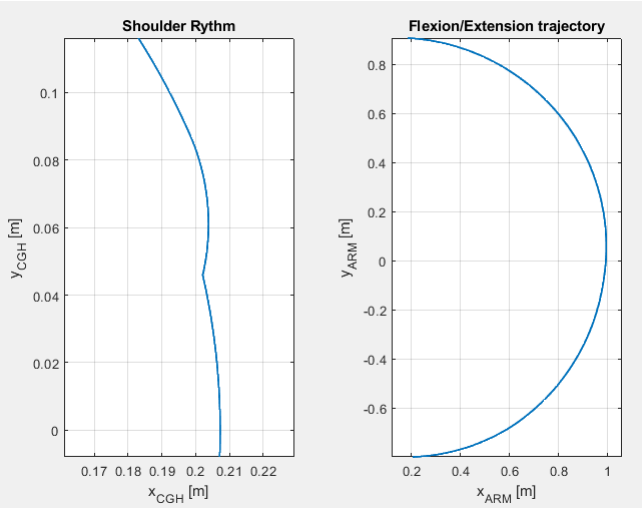

FIGURE 2.31: Movement of the CGH joint and end-effector (wrist) during arm elevation with workspace (x-y) generation

2.7 Human reference system

The three cardinal planes (Figure 2.32), two-dimensional imaginary surfaces defined by the spatial coordinates of three different points, dissect the mass of the body in three dimensions. The saggittal plane divides the body in half vertically dividing it into a left and a right side and each half contains the same mass by symmetry. The frontal plane also divides the body into two halves, of the same mass. Finally, the horizontal or transverse plane separates the body in the upper and lower halves, dividing it into equal mass. These reference

planes are fixed with respect to the human body, therefore at a rotation of this, they will follow it thus maintaining the same hours of intent with respect to the human body [13].

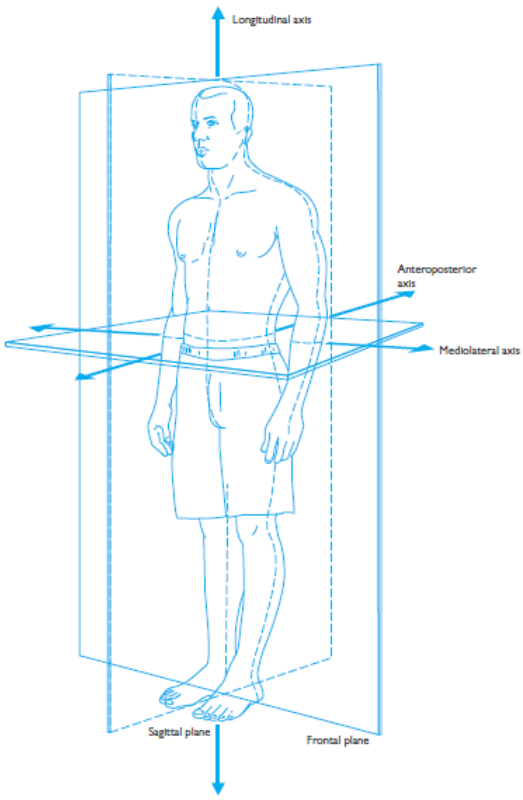

FIGURE 2.32: Human cardinal reference [13]

The three cardinal planes all intersect in a single point which is known as the body's center of mass or also called the center of gravity. The movements of the individual body segments can also be described as movements of the sagittal plane, movements of the frontal plane and movements of the transverse plane. This happens when the movements reside in a plane parallel to one of the cardinal planes.

However the human body is made up of many movements that are not oriented in the cardinal planes but the three main reference planes are still useful; The gross movements of the body, in particular the movements that occur in the joints are described with respect to the main planes, and therefore as predominantly frontal, sagittal or transverse movements [13]. The segments of the human body rotate around an imaginary axis of rotation, along the joint involved in the movement. There are three main reference axes oriented perpendicularly to one of the cardinal planes of reference and orthogonal to each other, used to describe human movement. The mediolateral axis is perpendicular to the sagittal plane, the anteroposition axis or the sagittal-horizontal axis for the rotations that occur in the frontal plane, and finally the longitudinal or vertical axis, for rotations that take place in the transverse plane [13].

Relevant terms with respect human reference system

Sagittal plane: plane in which the forward and backward movements of the different body segments reside

Frontal plane: plane in which the lateral movements of the body and its segments reside

Transverse plane: plane in which the horizontal movements of the body and its segments reside when it is in an upright position

Reference posture of arm: Hanging arms, no muscle activation. Parallel to gravity vector (0°)

Upper arm vector: Imaginary line with origin in the shoulder (glenoid cavity) directed at the elbow (reference in the middle point of the lateral and medial epicondyle)

Arm elevation angle: Angle between the upper arm vector and the gravity vector (between 0 and 180°)

2.8 Individual's fiosionomic data

The individual's fiosionomic data have been derived as a function of the ratio between the size of the body segments on the nominal height, and likewise the weights and centers of mass of each segment, relating them to the global mass of the individual (table 2.2).

For an average weight of 70 kg and an average height of 1.72 from the table 2.2 it results that the arm weighs 2.24 kg, the forearm 1.28 kg, and 0.48 kg for the hand. The length of the segments and the position of the centers of mass are respectively 0.33 m and 0.16 m for the extended arm, 0.26 m and 0.44 m for the forearm and 0.19 m and 0.66 m for the hand with the flexed shoulder at 90° and the arm fully extended. From the data available in the literature starting from field measurements, the average angular velocity of the upper arm flexion/extension ranging from 100 to 220°/s for detergents, and from 30 to 120°/s for employees in the measurements of the whole day. There are also angular velocity distributions of the upper arm ranging from 2°/s at the 10th percentile to 286°/s at the 99th percentile for fullday measurements on hairdressers, and from 20°/s to 152°/s for postal workers.As regards the speed of flexion/extension, the data [12] were taken as reference. The figure 2.33 shows the elevation angles of the arm with respect to time obtained through three different accelerometer techniques, a combination of accelerometer and gyroscope and an extremely precise optical system [12], during three different frequencies and arm movements. The subject performed oscillations of the arm in the sagittal plane with three different amplitudes and frequencies: 6 oscillations per minute, 24 oscillations per minute and 48 oscillations per minute. The graph shows 10 seconds of flexion and the average angular velocity is 32, 152 and 274°/s respectively for the 3 different tests.

For our simulations we chose a high working frequency with an average angular speed of 200°/s.

TABLE 2.2: Body segment lengths and masses and mass densities of body segments [26]

Segment	Segment length-/body heigth	Segment mass/-total body mass	Mass density [g/cm^3]	Distance of the center of mass from segmnt end (proximal)/segment length	Distance of the center of mass from segment end (distal)/segment length
Head	0.130	0.081	1.11	1	/
Neck	0.052	0.081	1.11	1	/
Shoulder width	0.259	/	/	/	/
Upper arm	0.186	0.028	1.07	0.436	0.564
Forearm	0.146	0.016	1.13	0.430	0.570
Hand	0.108	0.006	1.16	0.506	0.494
Chest width	0.174	/	/	/	/
Hip width/leg separation	0.191	/	/	/	/
Upper leg (thingh)	0.245	0.1	1.05	0.433	0.567
Lower leg (calf)	0.246	0.0465	1.09	0.433	0.567
Ankle to bottom of foot	0.039	/	/	/	/
Foot breadth	0.055	0.0145	1.10	0.5	0.5
Foot length	0.152	0.0145	1.10	0.5	0.5
Trunk	/	0.497	1.03	0.5	0.5

Human parameter I_{arm} is difficult to measure, as they are non-constant values as physical properties of human muscle characterized by changes [10]. In general, these models are treated leaving I_{arm} at zero for simplicity, and the variation of these variables was managed as modeling uncertainties. To obtain an estimate of the inertias with respect to the shoulder joint, the following approximate equations have been used:

$$I_{xx} = \frac{-250.7 + 1.56 body_{mass} + 1.152 body_{size} 100}{10000} [kgm^2] \tag{2.7}$$

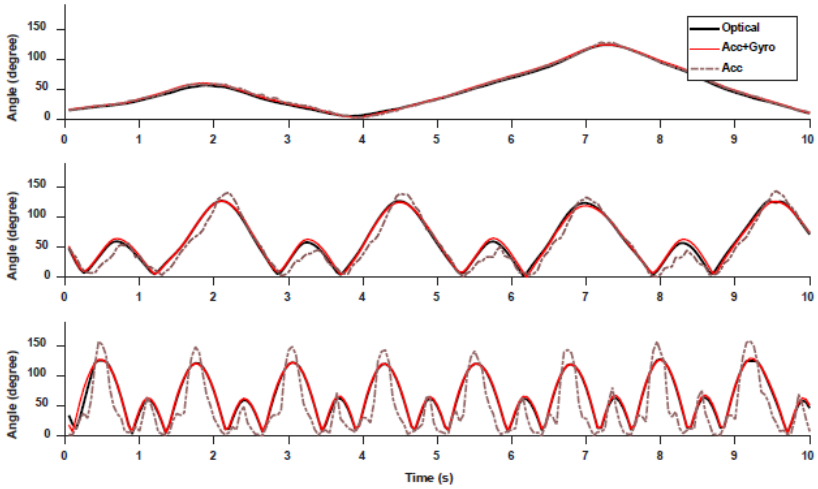

FIGURE 2.33: Estimated arm elevation angles with three different frequencies and arm movements, during arm flexion/extension movements [12]

$$I_{yy} = \frac{-232 + 1.525 body_{mass} + 1.343 body_{size} 100}{10000} [kgm^2] \tag{2.8}$$

$$I_{zz} = \frac{-16.9 + 0.306 body_{mass} - 0.088 body_{size} 100}{10000} [kgm^2] \tag{2.9}$$

The physiological movements of the shoulder and elbow are summarized in table 3.3.

TABLE 2.3: Physiological movements of the shoulder and elbow

Movements of the shoulder and elbow	Mobility range
Vertical flexion	0° - 180°
Vertical extension	0° - 60°
Abduction	0° - 180°
Adduction	0° - 45°
Horizontal flexion	0° - 130°
Horizontal extension	0° - 45°
Elbow flexion/extension	150° - 180°
Elbow pronation	0° - 180°
Elbow supination	0° - 90°

2.9 Comparison of arm elevation at work

The evaluation of the risk due to the exposure of the lifting of the arm and its maintenance over time in a fixed position can be attracted by variables calculated from temporal lines of elevation of the arm measured by technical

means. These variables can be used in the comparison in the different different conditions such as the performance of different tasks, jobs or working conditions in order to be able to give a qualitative risk assessment, that is "a low risk of physical disturbance, no action is required "; "A high risk of physical disturbance are preventive measures" [29].

In the literature there are some guidelines suggested in the ISO and EN standards that are based on a consensus of experts, it should be emphasized that the numerical characteristics of postural angles or temporal aspects are not established on the basis of epidemiological tests. The selection of elevation angles in scientific studies is based on visual observation that allows you to divide the right angle into two or three roughly equal parts, with high accuracy for 45°, 30°, 60° or 90° angles but with lower precision for 10° or 20° due to the difficulty of observation. However, the figures of the standards must be interpreted with caution as the numerical values of the risk limits are based on less accurate measurements than those obtained with the use of technical devices [29].

2.9.1 Static working positions (ISO 11226)

ISO 11226 [17] was developed to evaluate and evaluate the biomechanical load of static workstations, without forces taking into account external applied forces (eg the use of work tools); the legislation provides guidelines for the physical load on the trunk, neck, shoulders, arm. The legislation is divided into two phases, in the first one the joint angle for each body region is considered in order to assess whether it is acceptable for almost all healthy adults. In the second phase, instead, the duration of maintaining the same posture is analyzed to take into account the static muscle load. Every effort must be followed by a recovery time, while the duration limits correspond to 20% of the maximum maintenance time. A pain score of 2 is assigned on a visual analog scale (0-10). The load on the shoulder is determined during arm movement by comparing the vertical line (reference position) and the line passing through the acromion-clavicula and humerus-radius joints (Table 2.4).

2.9.2 Working positions and movements (EN 1005-4)

EN 1005-4 [1] carries out the analysis of each articulation / body region. The model of health risks associated with postures and movements is parabolic as shown in figure 2.34.

The evaluation of the load on the shoulder is carried out considering the static and dynamic loads as indicated in Table 2.5.

Where (1) indicates the condition of acceptability if full arm support is provided, if it is not, acceptability depends upon the duration of the posture and period of recovery. (2) Indicates the condition of not acceptability if the machine may be used for long durations by the same person. (3) Indicates the condition of not acceptability if frequency is $\geq$ 10/min or if the machine may be used for long durations by the same person [1].

TABLE 2.4: Static arm elevation assessment table [17]

Arm movements	Values	Duration
Extension- Flexion Vertical flexion	20° - 20°	acceptable
Flexion with full arm support	20° - 60°	acceptable
Flexion without full arm support	0° - 60°	20°:4', 40°:2'30, 60°:1'
Flexion	more than 60°	Not recommended
Other positions of the arm (eg extension (> 20°), adduction, external rotation, high shoulders)	-	Not recommended

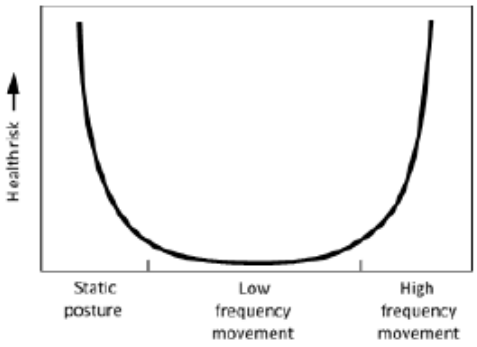

FIGURE 2.34: Physical health risks [1]

TABLE 2.5: Static and dynamic loads for arm elevation [1]

Arm movements	Values	Static (>4 sec)	Dynamic (<2 min)	Dynamic (>2min)
Flexion	0° - 20°	Acceptable	Acceptable	Acceptable
Flexion	20° - 60°	Conditionally acceptable (1)	Acceptable	Conditionally acceptable (3)
Flexion	>60°	Not acceptable	Conditionally acceptable (2)	Not acceptable
Extension	<0°	Not acceptable	Conditionally acceptable (2)	Not acceptable

2.9.3 Repetitive work (ISO 11228-3)

The ISO 11228-3 standard deals with regulating repetitive work [2]. It proposes two methods for risk assessment. The simplest method uses a checklist based

on the following factors: repetitiveness, effort, recovery periods and other additional factors. Different observation methods and consequent checklists can be used (eg OWAS, RULA, REBA or the OCRA index [2]).

Chapter 3

Degrees of freedom in the shoulder–elbow complex

The shoulder complex is made up of three moving bodies, each of which has 6 DoF thus giving the shoulder 18 DoF of possible movement. In the three spherical joints such as sternoclavicular, acromioclavicular and glenohumeral, 3 DoF are removed by the constraints of the joints, which reduce the degrees of freedom to 9 possible movements of the shoulder complex [26]. The scapulothoracic joint can be considered as a planar joint or as a simple ball joint with an infinite center of curvature, so this joint also creates restrictions by removing a further 3 degrees of freedom, bringing the shoulder to 6 DoF[26]. There are two further degrees of freedom constituted by the spinning of the clavicle and the humeral one. The humeral one in particular is similar to a robotic roller of the end effector that does not influence the orientation of the humerus. It therefore appears that to represent the shoulder complex 5 DoF are sufficient, 2 additional DoF are given by the elbow, so 7 DoF are sufficient to represent the complex elbow shoulder.

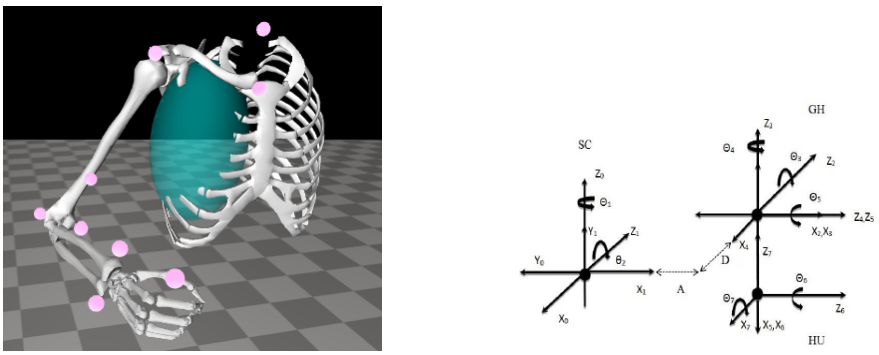

FIGURE 3.1: Degrees of freedom of the shoulder elbow complex. Upper Limb DoF (2 DoF SC + 3 DoF GH + 2 DoF HU)

The figure below shows the kinematic structure of the elbow-shoulder complex thus defined as the direction of the elbow axis; the axis is influenced by the movement of the shoulder during its natural movement. It consists of two subsets, namely the shoulder girdle and the serial arm. In particular, the shoulder belt consists of two revolute joints that intersect orthogonally. The arm, on the other hand, consists of the glenohumeral joint centered on the intersection of three orthogonal revolute joints, and finally the elbow joint, consisting of two revolute joints. The kinematic equations are derived using the Denavit

and Hartenberg (DH) theorem and its relative parameters presented in table 2 in the base frame is located in the thorax and the frame of the end effector is located in the elbow.

TABLE 3.1: Denavit and Hartenberg parameters for the shoulder-elbow complex

Link i	θ_i	d_i	a_{i-1}	α_{i-1}
1	$q_1 + \pi/2$	0	0	$\pi/2$
2	q_2	0.216	0.02	0
3	q_3	0	0	$-\pi/2$
4	$q_4 + \pi/2$	0	0	$\pi/2$
5	q_5	0	0	0

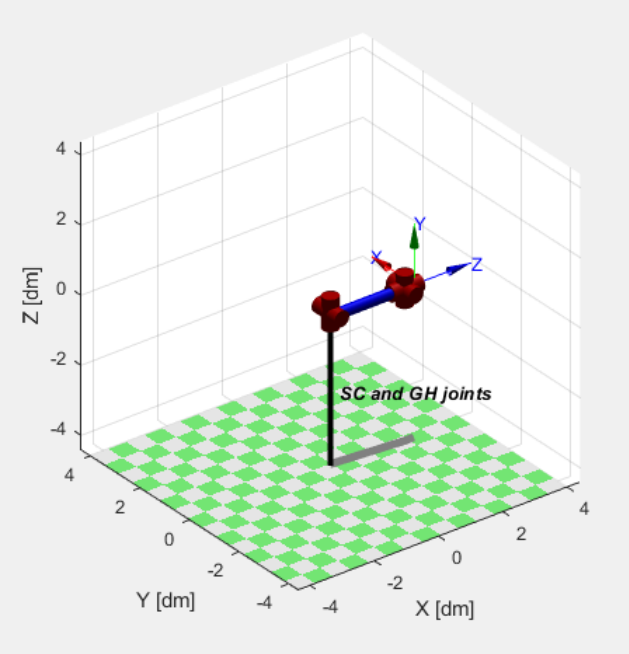

FIGURE 3.2: Sternoclavicular-glenohumeral complex kinematic chain

3.1 Degrees of freedom of the passive exoskeleton

The Denavit-Hartenberg convention was used to analyze the problem of direct exoskeleton kinematics. The kinematics of the exoskeleton has been assumed with 5 articulations, in particular 3 revolute DoF, 2 with incident axis in the middle shoulder, and 2 prismatic DoF, respectively to correct the shoulder rhythm and allow abduction in the horizontal plane, thus generating a kinematic chain open and correcting the phase shift caused by the shoulder. For the workspace analysis, only 4 DoF of the kinematic chain will be examined, in particular the prismatic joint related to abduction in the horizontal plane of the arm is removed. The reference kinematic chain is visible in figure 3.3.

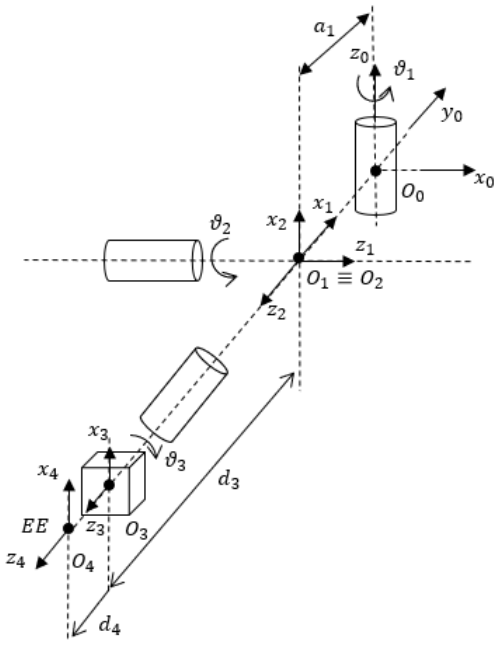

FIGURE 3.3: Reference frames positions according to DH convection

Once the reference systems have been fixed, following the DH procedure it is possible to define the table 3.2 containing the DH parameters

TABLE 3.2: Denavit and Hartenberg parameters for the passive exoskeleton

Link i	θ_i	d_i	a_{i-1}	α_{i-1}
1	$\theta_1 + \pi/2$	0	12	$\pi/2$
2	$\theta_2 + \pi/2$	0	0	$-\pi/2$
3	θ_3	15	0	0
4	0	d_4	0	0

Given the structure of the exoskeleton with 4 degrees of freedom, the working space is checked with the degrees of freedom allowed to the user who wears it. Some of the positions that can be reached by the end-effector may not be physically reachable due to variable articular range limits, collisions with obstacles in the environment, mechanical interference between the connections and in particular the physiological limits of human biomechanics. In particular, the full 360 ° rotation range on the rotating joints and the arbitrary travel on the prismatic joints are not possible due to the limitations of the natural joints of our body, the limits imposed by the tensioning of the springs and by the mechanical structure itself. The limitation of the articulations corresponds to a limitation on the positioning as well as on the amount of the displacement that significantly affects the working space. The study of the working space concerns only the articulations 1 and 2. In the following images the working space is shown when the degrees of freedom of the joints vary the degree of freedom of the shoulder in the horizontal plane and in the saggittal plane, with two successive variations of the degree of freedom of translation of the arm respectively the lower and upper limit given by the structure. The disadvantage is that the complexity or difficulty of closed-form solutions increases with the increase in the number of possible solutions. Increasing the amount of calculations makes it more difficult to control the exoskeleton. For this reason, the different solutions have been studied by varying the degrees of freedom of two joints at a time while maintaining the remaining constant.

The physiological movements of the shoulder are summarized in table 3.3.

Table 3.3: Physiological movements of the shoulder

Movements of the shoulder	Mobility range
Vertical flexion	0° - 180°
Vertical extension	0° - 60°
Abduction	0° - 180°
Adduction	0° - 45°
Horizontal flexion	0° - 130°
Horizontal extension	0° - 45°

Instead, vertical extension, adduction and extension are not included in this study, while the remaining three movements are limited, in the case of the cylindrical cam mechanism, by the geometry of the cam which limits vertical bending and abduction to 120° and the presence of the preloaded elastic elements that do not limit the work space but determine an optimal operating range with the lower imitation for vertical bending and 25° abduction, so the movements granted are shown in table 3.4.

The working space turns out to be a spherical cap (figures 3.4 3.5), varying the prismatic articulation it is possible to perform a volumetric optimization of the work space with respect to the limited variable intervals and the intermediate positions of the interval, and the work space is transformed into a volume of spherical cap with variable radius.

TABLE 3.4: granted movements of the working space

Limits	Mobility range
Vertical flexion	25° - 120°
Abduction	25° - 120°
Horizontal flexion	0° - 130°

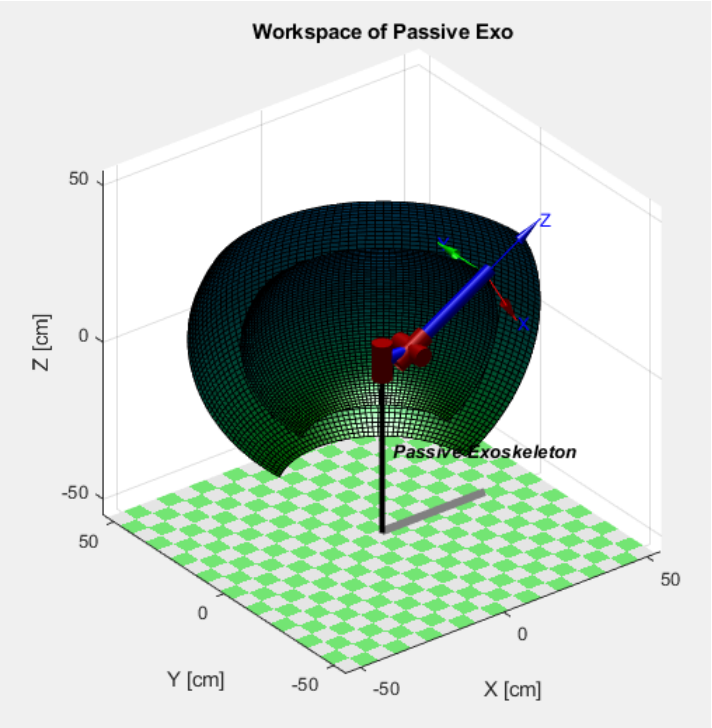

FIGURE 3.4: Passive Exo kinematic chain and workspace

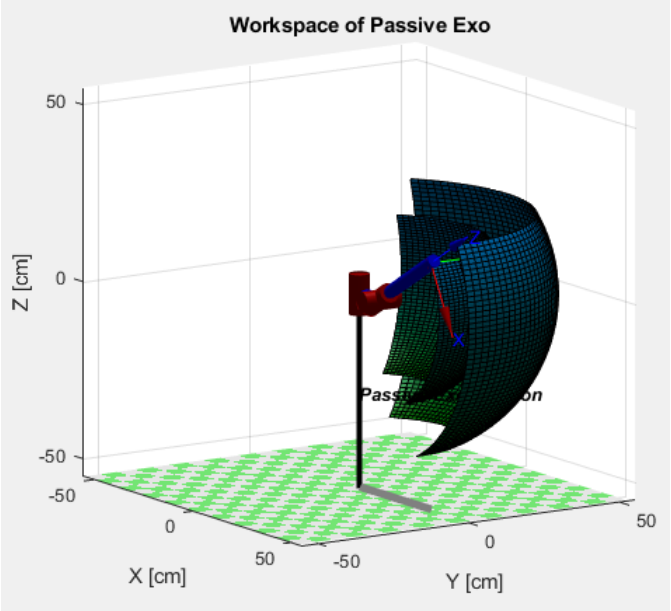

FIGURE 3.5: Rotate exo kinematic chain and workspace

Chapter 4

Spatial cam mechanism

Cam mechanism are used to convert rotary to linear motion (reciprocating). A cam and follower mechanism is a profiled shape that is mounted on a shaft, as the cam rotates, the follower rises and falls in a process known as reciprocating motion.The cams are called spatial when the transferor does not move in axes perpendicular to the directional axis of the cam, so the relative motion is not a plane motion. Spatial cams are subdivided into cup and drum cams which achieve the coupling of strength and shape. The coupling of footprint is obtained by a drum that runs inside a groove that acts as a guide, or by two rollers that embrace a rib (which eliminates the problem of the internal impact). The basic radius of the cam R_b is defined as the radius corresponding to the midpoint of the contact line.The kinematic design of these mechanisms is performed through the equivalent shape of the cam, in fact it is possible to obtain a spatial cam by wrapping an equivalent translational shape defined as the riser diagram on a cylinder of radius R_b . Mechanisms of this type are visible in the figure 4.1.

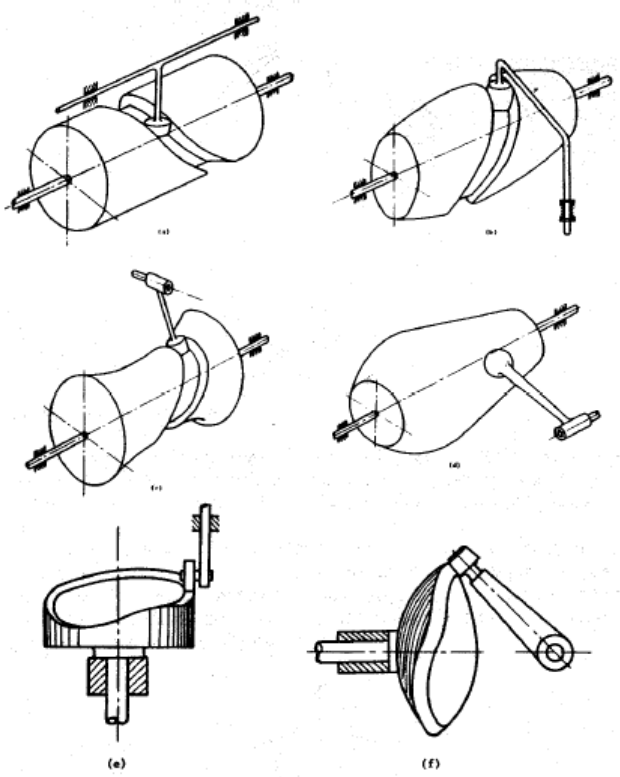

FIGURE 4.1: Types of spatial cams

Assuming a coordinate x along the cylinder of radius R_b , the pressure angle is given by

$$tg(\theta) = \frac{dy}{dx} \tag{4.1}$$

the radius of curvature of the primitive profile holds

$$\rho_0 = -\frac{\left[1 + \frac{dy}{dx}^2\right]^{\frac{3}{2}}}{\frac{d^2y}{dx^2}} = -\frac{1}{cos^3\theta \frac{d^2y}{dx^2}} \tag{4.2}$$

the x coordinate can be written as

$$x = R_b\theta \tag{4.3}$$

and therefore the pressure angle and radius of curvature results

$$tg(\theta) = \frac{y'}{R_b} \tag{4.4}$$

$$\rho_0 = -\frac{{R_b}^2}{cos^3\theta y''} \tag{4.5}$$

the base radius R_b is chosen by imposing that it does not exceed the maximum value of the theta pressure angle. Maximum value of y' defined as:

$$y'_{max} = \frac{c_v h}{\theta_s} \tag{4.6}$$

from equation 4.4, the design formula of the base radius is

$$R_b \geq \frac{c_v h}{\theta_s tg\theta_{max}} \tag{4.7}$$

to avoid undercutting the following inequality must be satisfied

$$|\rho_0| > R_r \tag{4.8}$$

where R_r is the radius of the wheel. Since the maximum value of y" is given by

$$y''_{max} = -\frac{c_a h}{(\theta_s)^2} \tag{4.9}$$

placing in a precautionary manner cos(θ)=1 on 4.5, from 4.8 is obtained

$$R_b \geq \frac{\sqrt{R_r c_a h}}{\theta_s} \tag{4.10}$$

In general, a cutter with the same diameter as the wheel is used for the construction of space cams. Execution takes place by moving the cam of rotary motion while the axis of the cutter simulates the prescribed movement for the

transferor. Therefore, once the transfer law of the transferor has been fixed, the calculation of the coordinates of the cutter center is immediate.

4.1 Law of motion

For the design of the cam, the diagram of the risers was drawn, thus establishing the succession, duration and width of the elements in accordance with the function that the mechanism must perform. The law of motion is a polynomial law imposing a constant ratio between the pressure angle and the angle of advancement. The constants constituting the polynomial have been derived as a function of the constraints imposed on the system.

Generally the laws of motion are given in dimensionless form, from which it is possible to trace the geometric quantities (as a function of the angle of the motive) and also as a function of time. The terminology used for the description of the system and the relationships between the various quantities are shown below.

Geometric quantities:

Law of motion according to the angle of the motive [mm]

$$y(\theta) \tag{4.11}$$

Geometric speed [mm/rad]

$$y(\theta)' = \frac{dy}{d\theta_1} \tag{4.12}$$

Geometric acceleration [mm/rad^2]

$$y(\theta)'' = \frac{d^2y}{d\theta_1^2} \tag{4.13}$$

Sizes as a function of time:

Law of motion [mm]

$$y(t) \tag{4.14}$$

Follower speed [mm/s]

$$\dot{y(t)} = \frac{dy}{dt} = \omega y' \tag{4.15}$$

Follower acceleration [mm/s^2]

$$\ddot{y(t)} = \frac{d^2y}{dt^2} = \omega^2 y'' \tag{4.16}$$

Shape or dimensionless sizes:

Dimensionless riser (corresponding to the shape of law of motion diagram)

$$Y = y/h \tag{4.17}$$

Dimensionless velocity (corresponding to the shape of the velocity diagram)

$$Y' = \frac{dY}{d\tau} = \frac{\frac{\dot{y}}{h}}{\frac{}{t_s}} = \frac{\frac{y'}{h}}{\frac{}{\theta_{1s}}} = \frac{t_s}{h}\frac{dy}{dt} = \frac{\theta_{1s}}{h}\frac{dy}{d\theta_1} \tag{4.18}$$

Dimensionless acceleration (corresponding to the form of the acceleration diagram)

$$Y'' = \frac{d^2Y}{d\tau^2} = \frac{\frac{\ddot{y}}{h}}{\frac{}{t_s^2}} = \frac{\frac{y''}{h}}{\frac{}{\theta_{1s}^2}} = \frac{t_s^2}{h}\frac{d^2y}{dt^2} = \frac{\theta_{1s}^2}{h}\frac{d^2y}{d\theta_1^2} \tag{4.19}$$

Dimensionless jerk is defined as

$$Y''' = \frac{dY''}{d\tau} = \frac{dy''}{d\theta_1}\theta_{1a}\frac{t_a^2}{h} \tag{4.20}$$

Dimensionless time/dimensionless angle

$$\tau = \frac{t}{t_s} = \frac{\theta_1}{\theta_{1s}} \tag{4.21}$$

By imposing a linear relationship between the transmission angle and the angle of advancement of the cam (Figure 4.2), the function that guarantees the required pressure angle is determined 4.22 .

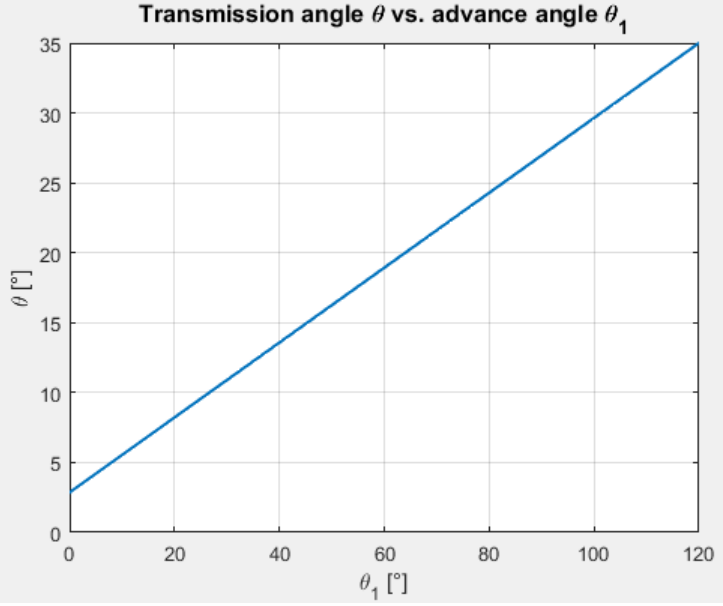

FIGURE 4.2: linear relationship between the transmission angle and the angle of advancement

$$y(\theta, \theta_1) = \frac{d_{average}}{2}\frac{\theta_{1i}}{cos(\theta_i)}k_i \tag{4.22}$$

In order to obtain a law as a function of the advancement angle only, the curve obtained was approximated to a 7th degree polynomial, defined as

$$y(\theta_1) = C_0\theta_1 + C_1\theta_1 + C_2{\theta_1}^2 + C_3{\theta_1}^3 + C_4{\theta_1}^4 + C_5{\theta_1}^5 + C_6{\theta_1}^6 + C_7{\theta_1}^7 \quad (4.23)$$

The coefficients were obtained through the MATLAB curve fitting toolbox software 4.1.

TABLE 4.1: 7th degree polynomial coefficients

Coefficients	Values
C_7	0005
C_6	-0.0013
C_5	0.0054
C_4	0.0256
C_3	0.0253
C_2	1.0069
C_1	0.3745
C_0	0.0000

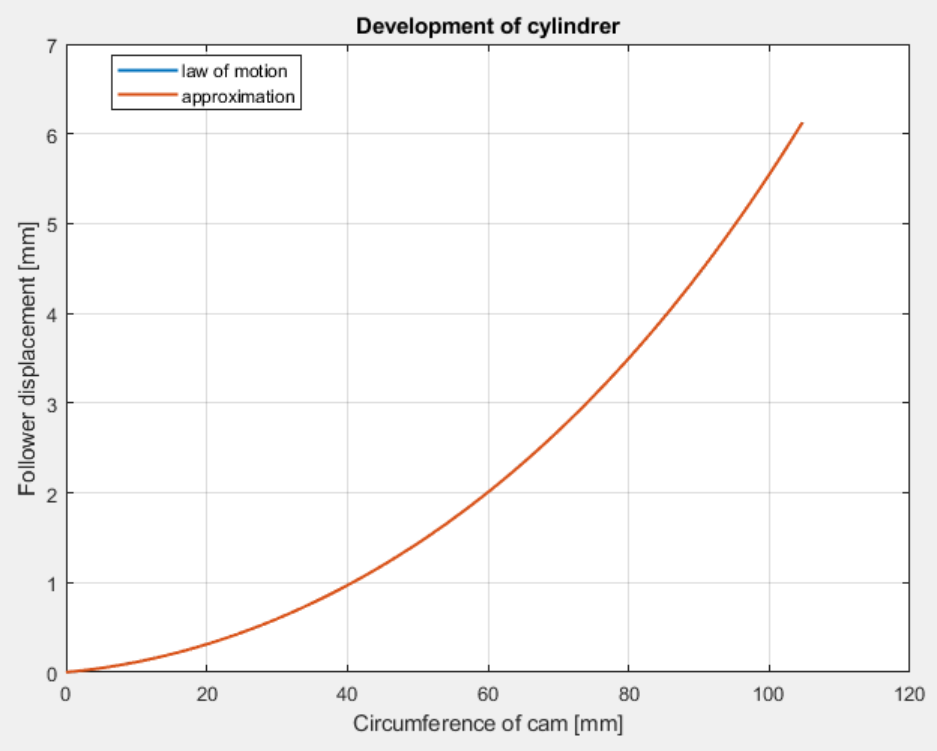

FIGURE 4.3: Development of cylindrer

The dimensionless quantities according to 4.17, 4.18, 4.19 and 4.20 are instead reported on figure 4.4.

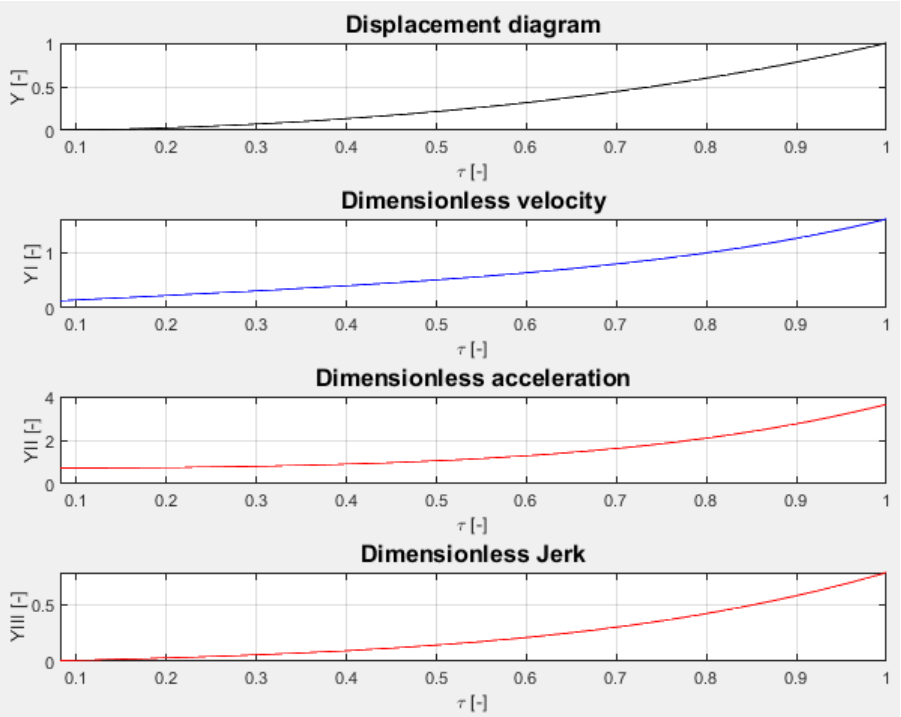

FIGURE 4.4: Dimensionless characteristics

4.2 Static analysis of mechanism

For the first sizing of the mechanism the static analysis of the mechanism is used. In particular, the two stages of movement of the mechanism are reported, the first in the phase of reloading the elastic elements (compression springs) and the second representing the phase of releasing the stored elastic energy. Depending on the relative motion existing between motive and transferor, the angle of friction between the roller and cam that characterizes the two stages of motion becomes predominant.

The mechanical system is constitutive of several springs placed in parallel with each other. Due to the complexity of the resulting system it is preferable to convert it into an equivalent mechanical system. In this way it is a matter of studying a mechanical system considering only a single spring of equivalent elastic constant. It is possible to generalize the concept for a number n of springs. A set of springs in parallel can be treated as a single spring of equivalent elastic constant, from which it is necessary to calculate the equivalent elastic constant. Considering a generic displacement y_i, the deformation will be the same for all the springs placed between them in parallel:

$$y_0 = .. = y_i = .. = y_n = y \tag{4.24}$$

The equation of a generic dynamics due to elastic forces acting on a mass m is defined as:

$$m\ddot{y} = k_e y \tag{4.25}$$

Where k_e is the quivalent elastic constant defined as:

$$k_e = \sum_{i=0}^{n} k_i \tag{4.26}$$

For which a 18N/mm k_i stiffness was considered, with a y_i deformation equal to 9mm with a preload of about 3 mm. The elastic force generated by the deformation of the springs is shown in figure 4.5.

The figures 4.6 and 4.7 show a schematization of the contact between the grooved track of the drum and the pin where the conversion of the elastic force takes place in a torque necessary to rotate the drum of the cam which is instead integral with the shoulder joint. The schematization is based on the method of equivalent wedges used in screw transmissions. The translation in the vertical direction of the transferor (pin) corresponds to an equivalent rotation of the drum and therefore also of the joint integral with it.

The static balance will be equal to:

$$O_c = F_m tg(\theta - \varphi) \tag{4.27}$$

Where θ is the angle of inclination of the groove on the drum while φ is the angle of friction between the two surfaces which is a function of various parameters, in particular of the materials in contact and the presence of lubrication. To obtain the torque M_{ert} generated by the force of the spring it is sufficient to multiply the force O_p by the average radius of the drum r_m.

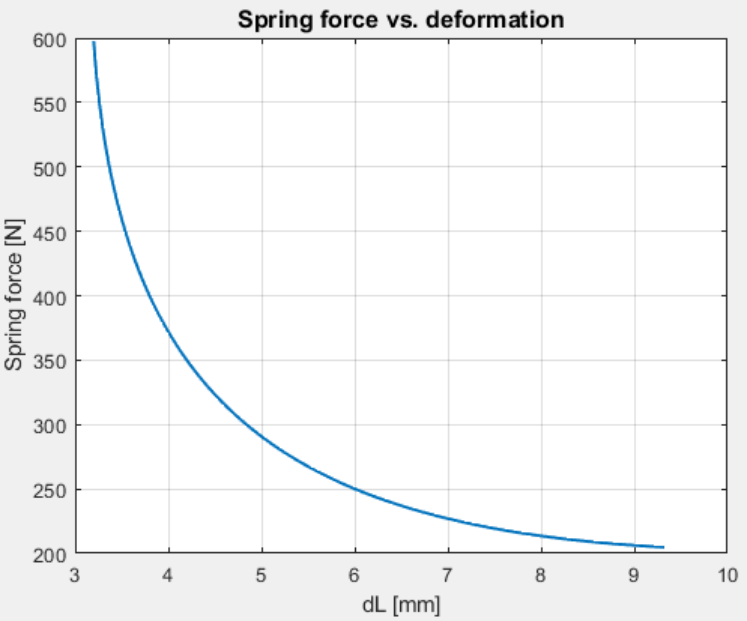

FIGURE 4.5: Spring force vs. deformation

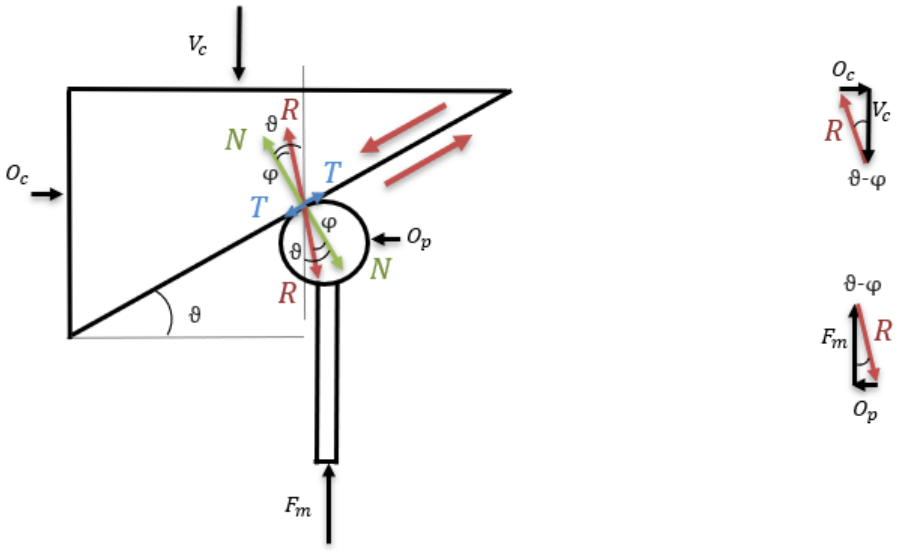

FIGURE 4.6: Elastic released torque static scheme

The elastic released torque will be:

$$M_{ert} = \frac{d_m}{2} F_m tg(\theta - \varphi) \tag{4.28}$$

Equation 4.28 is valid only in the ascending section of the transferor, ie when the elastic energy of the springs is released. Conversely, in the energy storage phase, there is the true compensation process, and the friction between the drum and pin is an important parameter.

In fact according to the scheme 4.7, The static balance will be equal to:

$$O_c = F_m tg(\theta + \varphi) \tag{4.29}$$

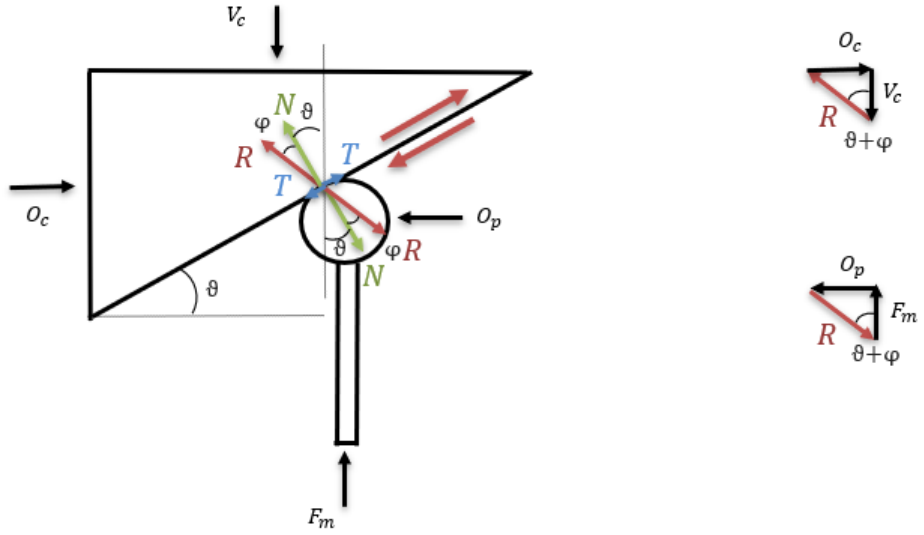

FIGURE 4.7: Torque compensation static scheme

Where the angle of friction φ is added to the horizontal component and not subtracted. This generates more torque than the energy release phase thus generating more resistance in the compression of the springs.

The static torque compensation will be:The elastic released torque will be:

$$M_{stc} = \frac{d_m}{2} F_m tg(\theta + \varphi) \tag{4.30}$$

The trends of the moment generated by gravity and of the resistant torques 4.30 and 4.28 are shown in figure 4.8.

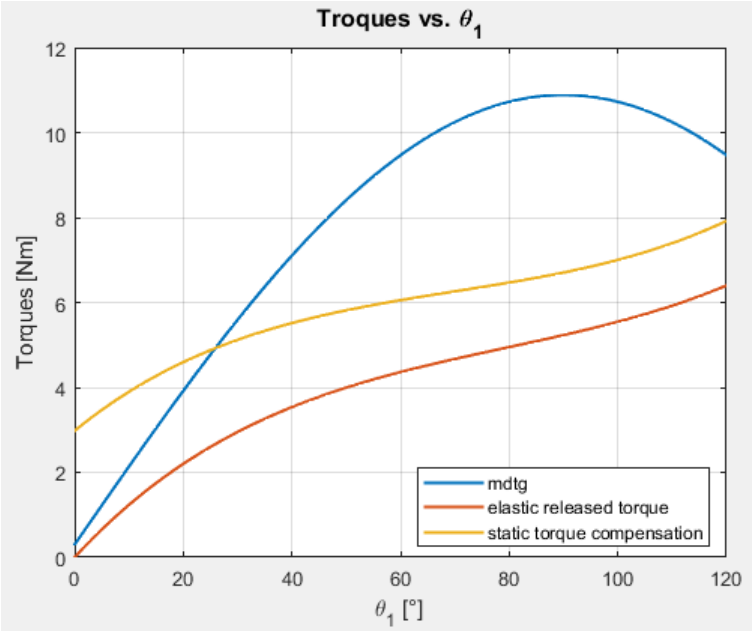

FIGURE 4.8: Torque compensation static results

The residual torque borne by the operator in static conditions, ie when the

individual during a generic operation will remain in a fixed position with the arm flexing, is shown in figure 4.9.

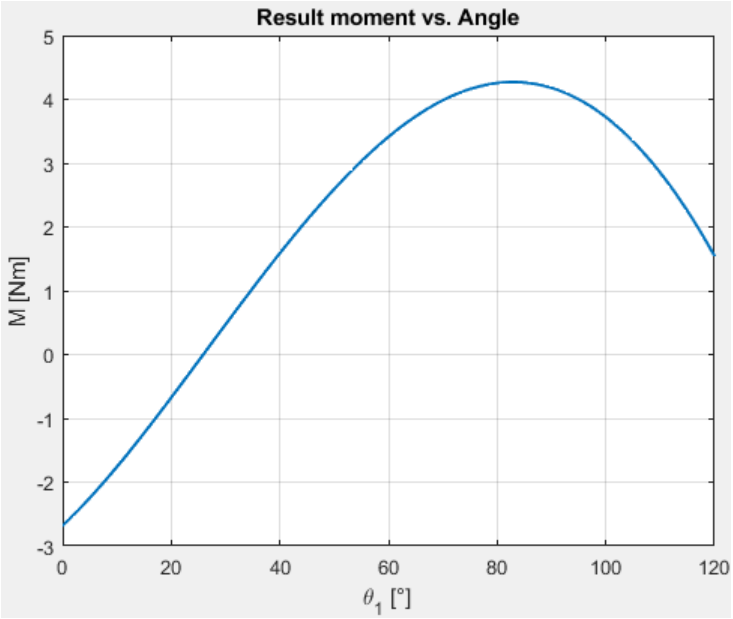

FIGURE 4.9: Result moment vs angle

In addition to having reduced the torque due to gravity up to 63% compared to the total cup (90° arm position), the residual torque results to have a smooth trend, reported on Figure 4.10.

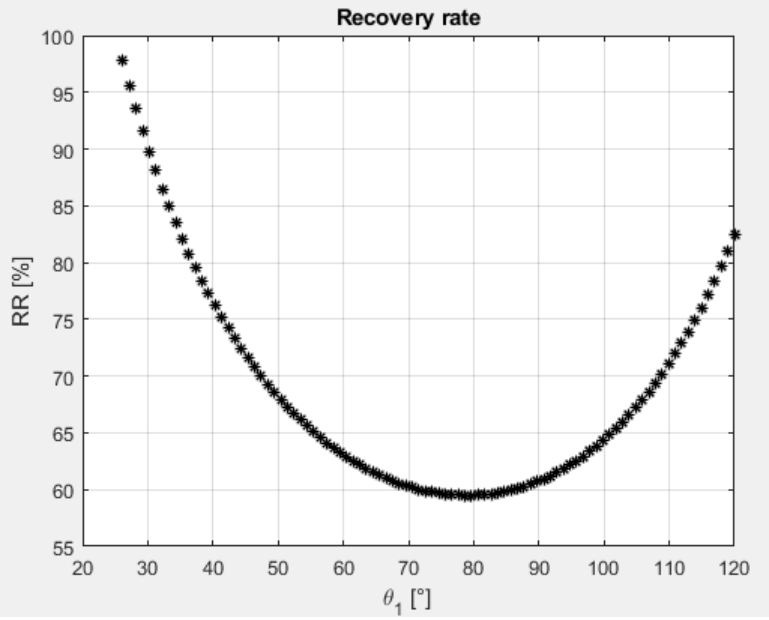

FIGURE 4.10: Recovery rate

TABLE 4.2: Main parameters of models

Parameters	Values
$d_{average}$ [m]	0.10
f (lubricated steels)	0.05
k_i [N/mm]	18
k_e [N/mm]	72
θ [°]	0-35

4.3 Mechanical stresses

The contact between cam and follower is rolling, so that generally needle pins are used with needles provided for this specific application, or alternatively the wheel can be made by averages of a ring mounted on common rolling bearings. The bearings are normally chosen from the catalog based on the load and the expected life taking into account that the rotating ring is the external one. It is therefore necessary to check that the maximum pressure p_{amm} exercised between the cama and the transferor does not exceed the allowable value pamm to avoid wear and tear with uperficial fatigue. An indicative permissible load value for cast iron and steel can be derived from

$$p_{amm} \simeq \frac{HB}{5} \tag{4.31}$$

where HB is the Brinell hardness of the cam surface. While for case-hardening steel it can be used

$$p_{amm} \simeq 2HRC \tag{4.32}$$

where HRC is the Rockwell C hardness of the cam surface.

The maximum pressure exerted on the contact area between the two surfaces is calculated using the Herz formula:

$$p = \sqrt{\frac{S\left(\frac{1}{R_r} + \frac{1}{\rho}\right)}{\pi b\left(\frac{m_1^2 - 1}{m_1^2 E_1}\frac{m_2^2 - 1}{m_2^2 E_2}\right)}} \tag{4.33}$$

where R_r is the radius of the wheel, rho the radius of curvature of the cam profile, S the mutual thrust, b the width of the wheel, m_1 and m_2, E_1 and E_2, are the Poisson modules and the modulus of elasticity of the material. In particular, in the formula 4.33 ρ must be inserted with its sign (+ if the point of the cam has convexity, - in the opposite case). Taking on $m_1 = m_2 = 10/3$ and $E_1 = E_2 = E$, the equation 4.33 can be written as

$$p = \sqrt{0.175\frac{ES}{bR_r}\left(1 + \frac{R_r}{\rho}\right)} \tag{4.34}$$

since S and ρ vary from point to point in the profile, it must be verified that

$$p \leq p_{amm} \tag{4.35}$$

it must be done at the points of danger, adopting the corresponding values of S and ρ. An approximate allowable thrust value can be obtained, regardless of the shape of the profile, referring to the extreme case in which the wheel rotates on a rectilinear profile ($\rho \to \infty$), from equation 4.33 is obtained

$$\frac{S}{2bR_r} \leq p^* \tag{4.36}$$

with

$$p^* = \frac{p_{amm}^2}{0.35E} \tag{4.37}$$

p* values for steel in the case of pure rolling are shown in the table 4.3.

TABLE 4.3: Main properties of seel - mechanical stresses

HB	HRC	σ_{amm} [kg/mm^2]	p$_{amm}$ [kg/mm^2]	p* kg/mm^2]
200	-	70	40	0.22
250	23	88	50	0.34
300	30	105	60	0.49
350	36	123	70	0.67
400	41	159	80	0.87
450	46	159	90	1.10
500	50	-	100	1.36
-	55	-	110	1.65
-	60	-	120	1.96
-	65	-	130	2.30
205-210	65	-	400-420	-
210-220	65	-	500-520	-
300-320	65	-	600-650	-

at the points where the R_r/ρ ratio is not negligible with respect to the unit, the allowable thrust must be divided by $(1 + R_r/\rho)$. In particular it should be noted that for $\rho = 3R_r$ the permissible thrust is halved, for $\rho = 2R_r$ it is reduced by 33%, for $\rho = 3R_r$ is reduced by 25%. As a good design rule it is advisable that the radius of curvature does not fall below the value $\rho \simeq 1.5R_r$.

Another expedient is that relating to assembly errors, especially with regard to the alignments, which generate distributions of non-symmetrical pressures in the wheel which generates a concentration of stress at one end of the contact line. This phenomenon can be avoided by imposing that the length b is not excessive, and in the case of cantilever wheels this phenomenon also occurs for the bending of the pin under load, a solvable problem with a pin held by a fork. In any case, to limit the concentrations of stress due to misalignments it is possible to use convex wheels which generates an increase in contact pressure even in the case of perfect assembly, but this is largely compensated by the certainty that this value does not undergo alterations due to uncontrollable geometry variations.

The radius of curvature according to equation 4.5 is shown in figure 4.11.

While the trend of the contact pressures is shown in figure 4.12 according to equation 4.34. In order to respect the condition imposed by the sizing (equation 4.35), the choice of a C40 tempered steel was hypothesized.

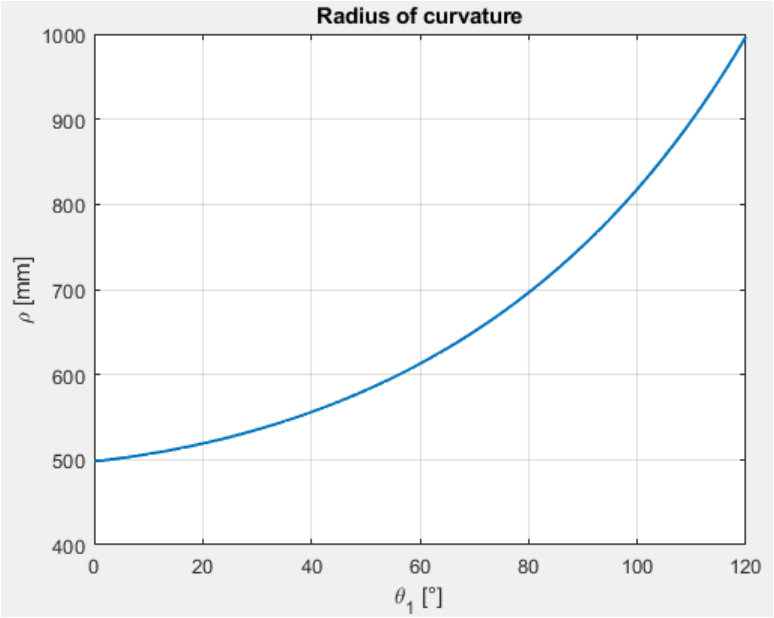

FIGURE 4.11: Radius of curvature

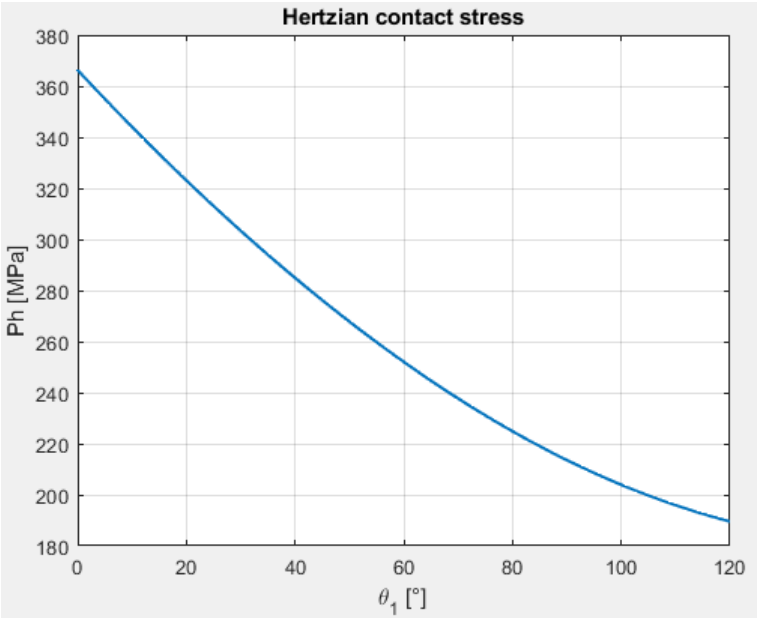

FIGURE 4.12: Herzian contact stress

4.4 Force coupling

In the cam mechanisms it is very frequent the case in which the contact between motive and transferor is assured by the forces acting on the transferor, which hold it at all times on the motive. The forces acting on the transferor are:

- The generally small amount of own weight that can be used to maintain contact between the two members. In the case in question, it is perpendicular to the direction of motion, so its action on the motive is zero.

- Friction resistances, or the resultant of forces opposing the motion of the transferor.
- Useful resistances are the forces that the transferor must overcome to perform his functions, in many cases they can be high but generally maintain a constant line. In the case studied, there are no forces acting directly on the transferor, except the driving force given by the elastic elements.
- Inertia actions due to the accelerations generated by the cam; in the case studied, being the coupler coupled with the upper surface of the cam, they tend to maintain contact when $\ddot{y}<0$ and tend instead to cause detachment when $\ddot{y}> 0$. In particular the inertia actions correspond to the square of the angular velcoity according to equation 4.16. They can in many cases become very large.

The overall trend of inertia and friction forces is shown in figure 4.13 and 4.14. often the determination of F_m and F_{m0} is carried out by neglecting the external charge, the weight and the frictions, and therefore it is simply necessary that the force of the spring in each point exceeds the inertia force, therefore it results

$$F_s + R = F_{s0} + ky + m\omega^2 y'' > F_{min} \tag{4.38}$$

with F_{min} minimum permissible safety load.

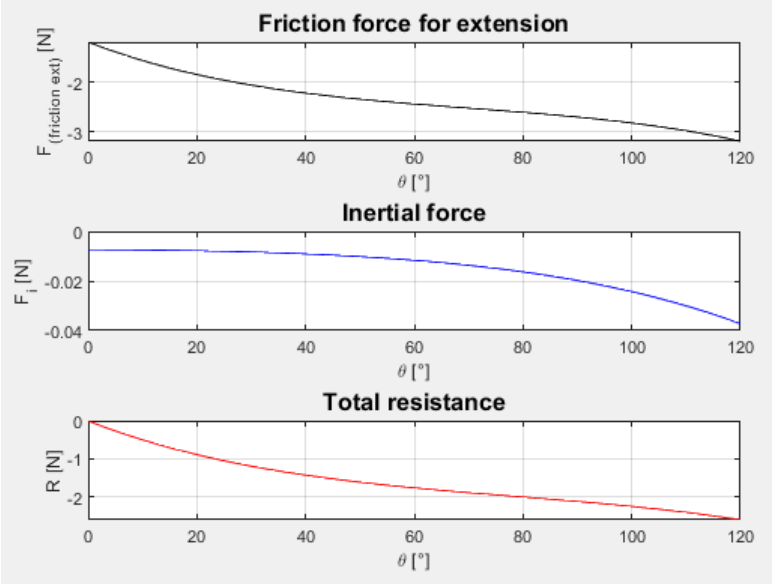

FIGURE 4.13: Total resistant force for extension

The resistant torque of the cam pin according to the equation was also evaluated, which depends on factors such as the load, speed and type of wheel and the state of lubrication and the friction of the seals. Given the multiplicity of these factors, the moment of friction for wheels with non-creeping seals, as a first approximation can be calculated as:

$$M_r = f_{Mr} F_r \frac{d_{average}}{2} \tag{4.39}$$

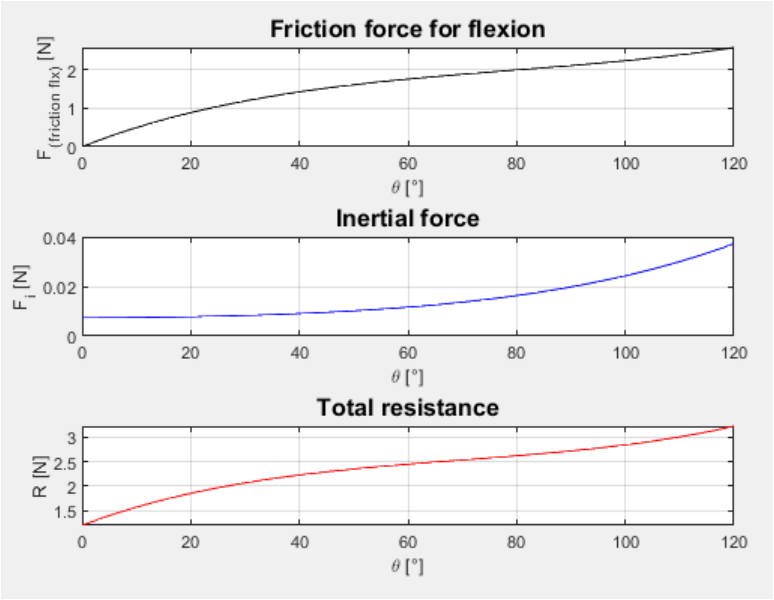

FIGURE 4.14: Total resistant force for flexion

where M_r [Nm] is the wheel friction moment, f_{Mr} is the friction coefficient (table 4.4), F_r [N] is the radial load [N], and $d_{average}$ the average wheel diameter (d + D)/2 [m].

TABLE 4.4: Main friction coefficients for pins

Wheel type	friction coefficient
Single row ball bearings	0.0015 - 0.002
Double row ball bearings	0.002 - 0.003
Full complement cylindrical roller bearings	0.002 - 0.003
Needle roller bearings with cage	0.003-0.004
Full complement needle roller bearings	0.005 - 0.007

Its trend is shown in figure 4.15.

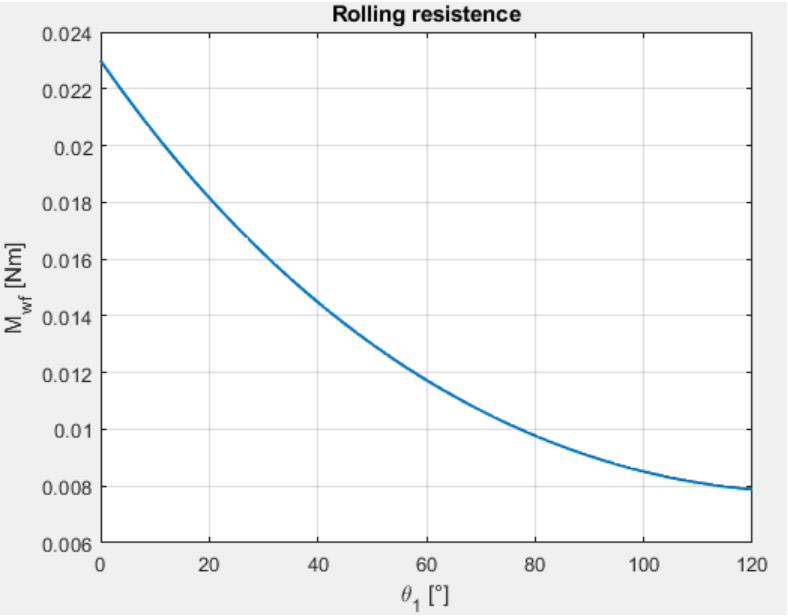

FIGURE 4.15: Rolling resistance

4.5 Mechanical design

Through 3D CAD modeling, realized through SolidWorks (software used in the fields of mechanical and industrial design for the creation of three-dimensional prototypes), a first approximate dimensioning of the components of the device was made to transform the potential energy of the arm into potential elastic energy.

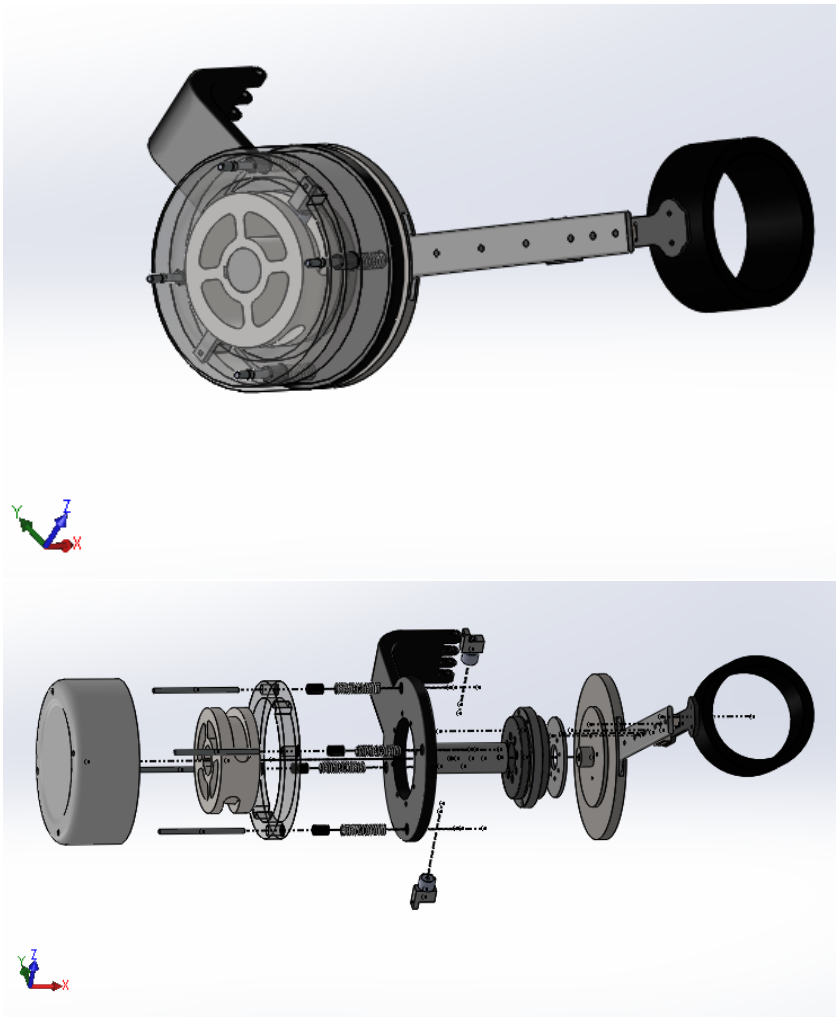

FIGURE 4.16: Device CAD model

The device (Figure 4.16) is composed of the arm support, sliding with respect to the shoulder joint given the presence of a prismatic connection joint. The rotary shoulder joint is integral with a shaft onto which the spatial cam is keyed. At the same time the connection shaft is fixed, compared to a rotary platform bearing, which functions as a classic bearing but with considerably lower weight. the outer ring of the rotary support is fixed to the exoskeleton arm support, allowing the loads to be unloaded into the structure. In the cam operate four compression springs, seated in the exoskeleton arm support and in an outer ring. Along the axial direction of the springs there are linear guides made up of steel bars and linear bearings that allow only the axial translation of the device and therefore the deformation of the springs. The cam wheels are

keyed in the outer ring, thus allowing the transmission of the thrust given by the elastic elements which generates the torque perfectly in the shoulder joint.

In figure 4.17 it is possible to observe in greater detail the Spatical CAM EXO model.

FIGURE 4.17: Spatial CAM EXO model

The CAD model provides a first overview of the device to be built, indicating its main features:

- The cam mechanism acts directly on the shoulder joint, generating the required pair of compenation;

- The prismatic joint decouples the implementation of the shoulder from the rhythm of the shoulder, allowing an adequate response to the physiologic movements of the individual.

From Figure 4.16 it is intuitive that the most stressed components are those relating to the support of the elastic elements (springs) and the transformation cam.

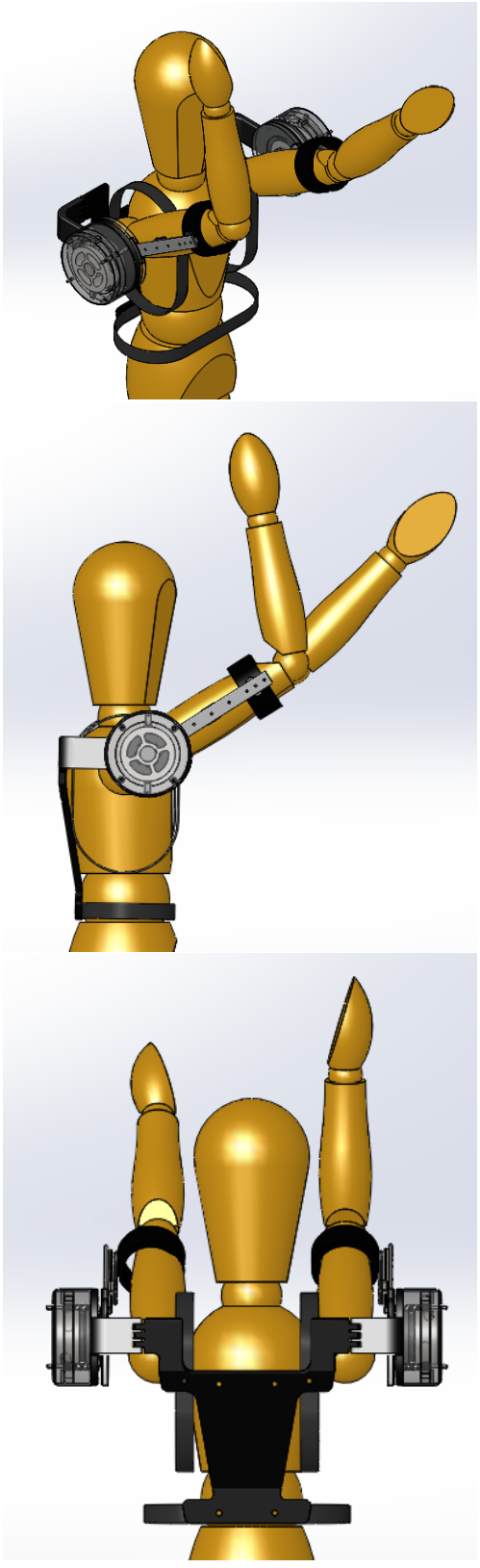

FIGURE 4.18: EXO model with respect to human dimensions

4.5.1 Exo weight

With the aim of estimating the overall weight of the exoskeleton, a vision of the assembly with a chromatic scale in order of weight has been proposed. Figure 4.19 shows the net weights of the exoskeleton with a scale from red to blue to indicate respectively from the heaviest element to the lightest one.

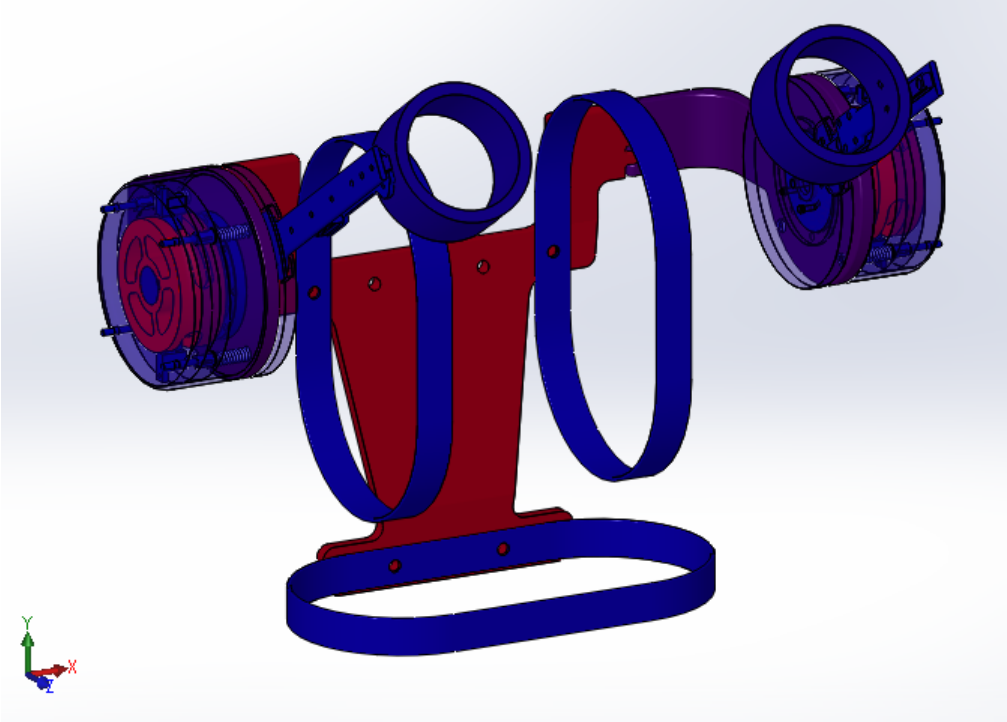

FIGURE 4.19: EXO components weght

The weights of the individual elements are shown in table 4.5.

The total weight of the device is 9 kg (Table 4.5), with a tolerance of 1 kg considering additional mechanical elements (screws and support nuts).

TABLE 4.5: Main weight elements of the exoskeleton

Element	Quantity	Weight [kg]
Spatial cam	2	1.31
Support structure	1	1.14
Shoulder joint shaft	2	0.8
Horizontal movements link	2	0.51
Support file	2	0.4
Shoulder Joint	2	0.24
belt and shoulder support	1	0.20
External cam support	2	0.19
Device cover	2	0.16
Arm support	2	0.16
Device Spacer	2	0.05
Prismatic joint guides	2	0.08
compression springs	8	0.04
Device support bars	8	0.01

4.6 FEM analysis

Through the use of Siemens NX, a further CAD software used for the design of prototypes, a FEM analysis of the exoskeleton structure was carried out, using the values detected by the model developed through MATLAB software as stresses. As an example of FEM analysis the main components subjected to the action of the springs and the resistance opposed by a subject to a movement of the limb are reported. The resisting forces (approximate) detected by the model, and therefore the input parameters of the simulation, are:

- Simulation: Only arm weight support
- Loads: 30N average arm weight (arm completely extended horizontally)
- Local and global constraints: Fixed arm link in the joint such as internal constraints of the system, screws supporting the prismatic joint and screws fixing the arm to the shoulder joint
- Material: carbon fiber material, with the exception of the prismatic joint supports which are made of steel and reinforced chrome
- Mesh: tetrahedral (variable for each element according to the geometry and dimension) - convergence analysis
- Simulation Object Type: Surface-to-Surface gluing. Is a simple and effective method for joining meshes that are dissimilar available in FEMAP with NX Nastran. It correctly transfers shifts and loads with consequent accurate stress and stress conditions at the interface, where the grid points on glued edges and surfaces do not necessarily have to coincide.

The contribution of gravity is also taken into account.

Of particular interest is the displacement to which the device is subjected caused by the deformation of the components with respect to the forces acting on them. (Figures 4.20). The displacements are of the order of millimeter, and are to be considered acceptable at this level of design.

The main supports of the elastic elements of the cam device, in particular the support ring for springs and pins, and the support link of the device have also been analyzed.

For the external device support, the simulation input parameters are:

- Simulation: External spring internal support
- Loads: 600N elastic forces divided with geometric subdivisions for the spring seats
- Constraints: Fixed arm link in the joint
- Material: carbon fiber material
- Mesh: tetrahedral 6 mm - convergence analysis

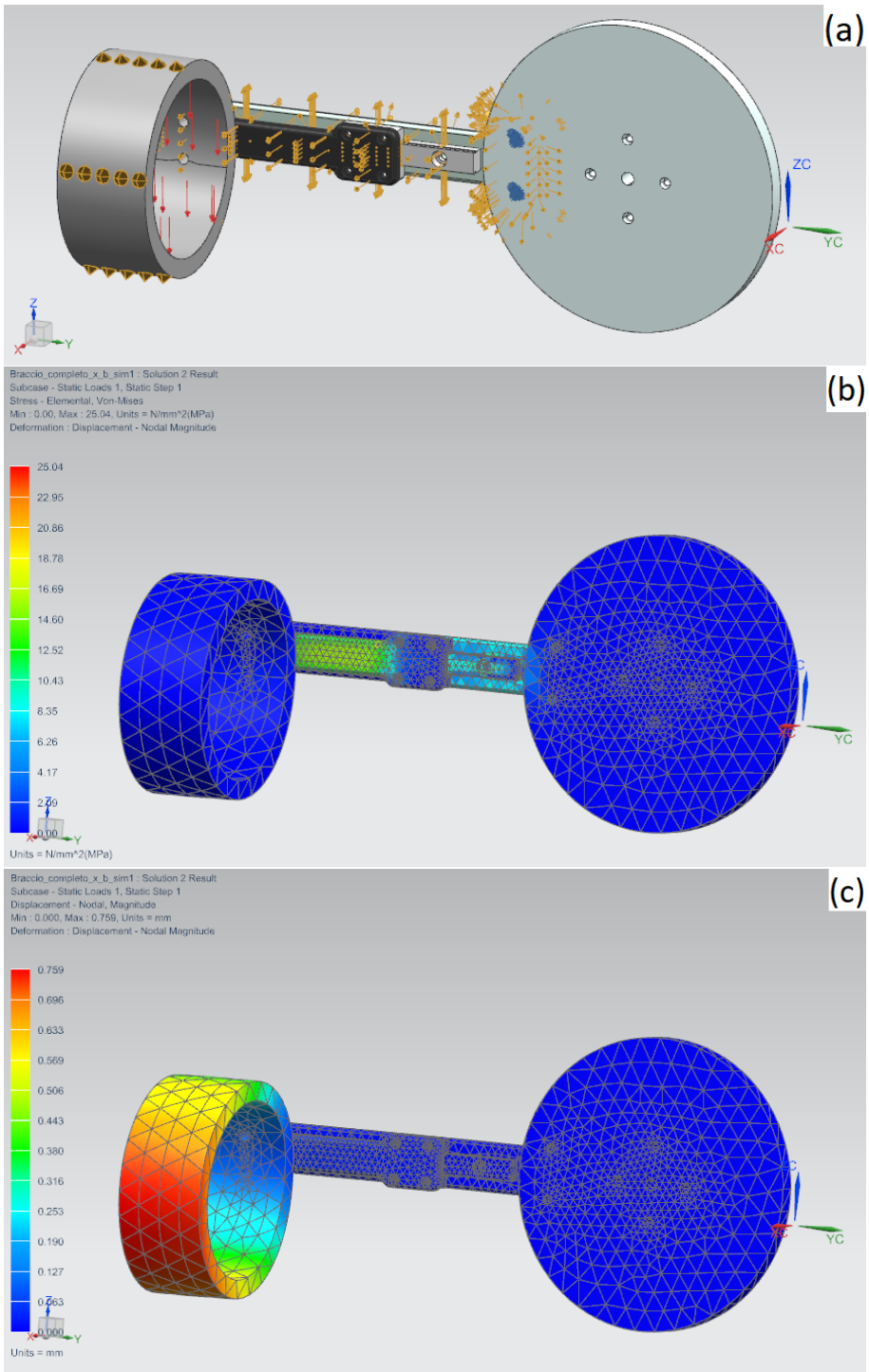

FIGURE 4.20: EXO arm link model: a) forces and contraints b) von Mises Stress c) Displacement

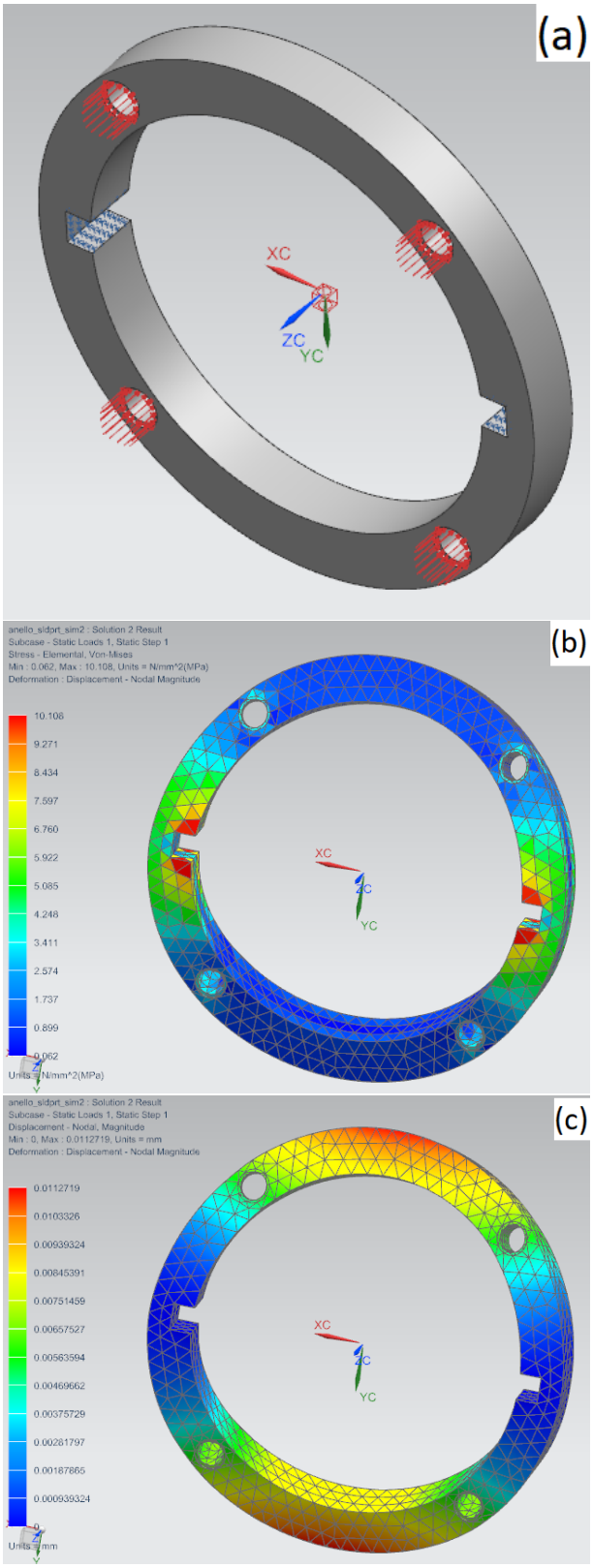

FIGURE 4.21: External device support: a) forces and contraints b) von Mises Stress c) Displacement

For the external internal support, the simulation input parameters are:

- Simulation: Compressed spring internal support
- Loads: 600N elastic forces divided with geometric subdivisions for the spring seats
- Constraints: Fixed arm link in the horizontal flexion and extension joint
- Material: carbon fiber material
- Mesh: tetrahedral 6 mm - convergence analysis

Also in this case, the displacements of the elements turn out to be of a few millimeters, considered acceptable for this level of definition.

In figures 4.20, 4.21 and 4.22 the tendency of tensions according to the equivalent stress of Von Mises is reported. With the choice of the aforementioned materials, comparing for each element its elastic limit, it is inferred that the developed values of the tensions are remarkably low; this guarantees a minimum safety coefficient of 4 in the structure as a whole. The best solution would be to produce the fixed part of the exoskeleton (bars and supports) in carbon fiber given the low density and its high strength the exoskeleton would be remarkably light distributed between the waist and shoulders of the operator.

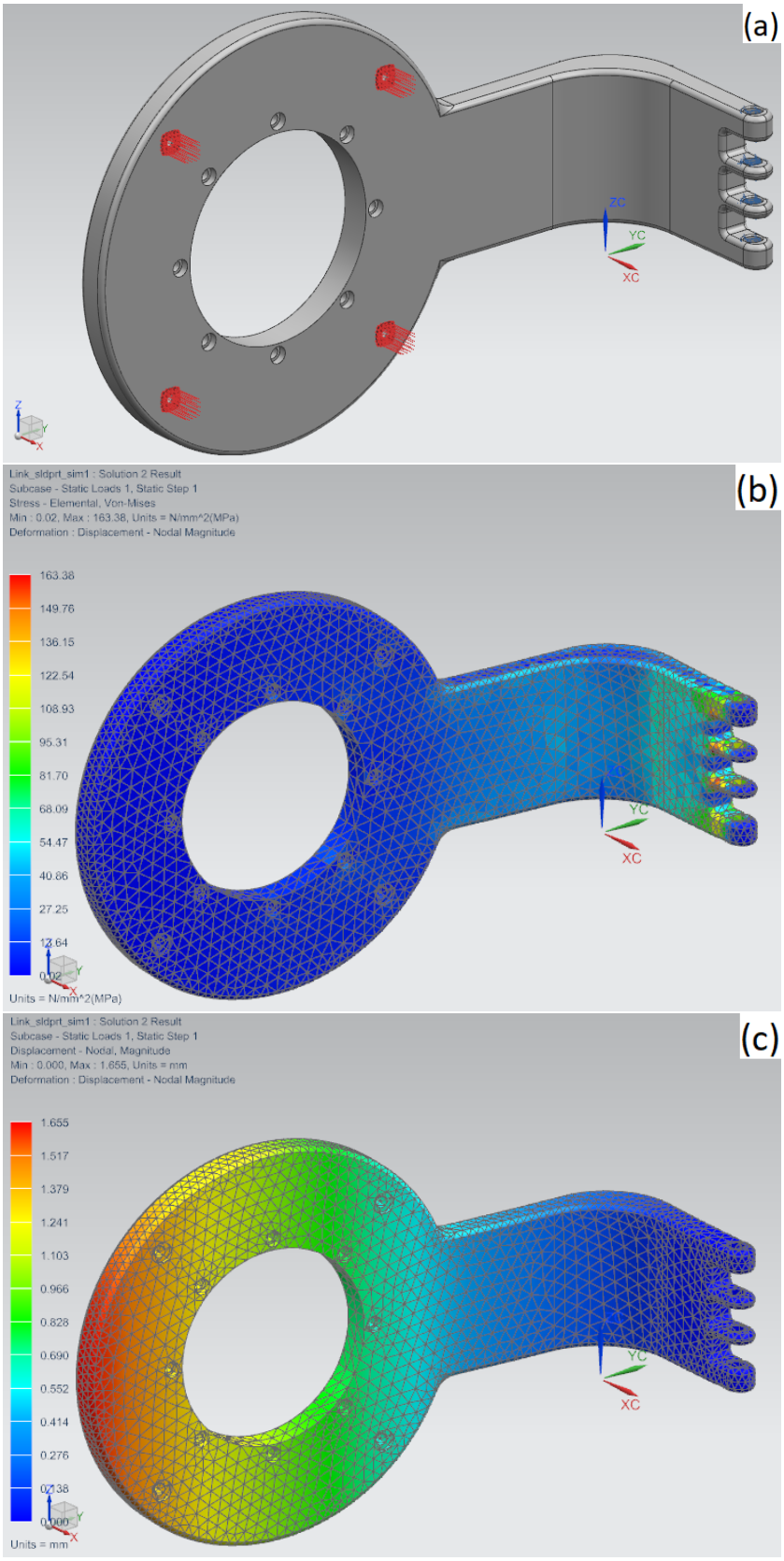

FIGURE 4.22: Internal device support: a) forces and contraints b) von Mises Stress c) Displacement

Chapter 5

Fluidic Muscles

The fluidic muscles are driven by a compressed gas, in our case is air, which acts on an inflatable internal bladder sheathed by a twisted double-wave braided mesh which contracts its longitudinal length as it expands in a radial direction. During contraction, the artificial muscle generates a useful force, and by working at compression, the force generated will be able to pull the tendon element of the muscle, the function principle of a pneumatic muscle is described in more details for example in [5].The most used muscle in practice is McKibben's braided muscle (sleeved bladder muscle) but there are different types, such as: netted muscles such as the Yarlott muscle, ROMAC, and the Kukolj muscle, pleated muscles (PPAM muscle),Paynter knitted muscle, Paynter hyperboloid muscle visible in figure 5.1. Other types are embedded muscles (Morin muscle, Baldwin muscle, muscle under pressure, the Kleinwachter torsion device) and finally the special muscles (rotational muscle, 3-DOF muscle, single action elastic tube and combination). [7], [20].

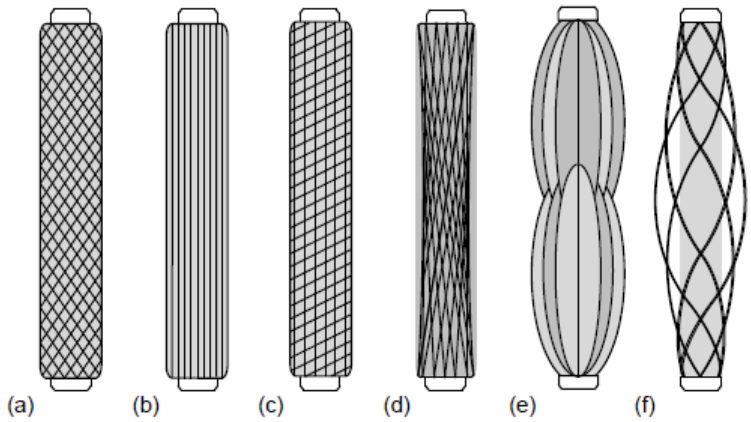

FIGURE 5.1: Types of pneumatic actuators: a) McKibben muscle, b) Pleated muscle, c) Yarlott netted muscle, d) Paynter hyperboloid muscle, e) ROMAC muscle, f) Kukolj muscle [20]

McKibben's muscle can be simulated through a static model proposed by Ching-Ping Chou and Blake Hannaford in 1996, using virtual works. The model is based on the relationships existing between the pressure actuator and the length of the mesh [5].The main geometric parameters for the generation of the static characteristic are the number N wrapped by single fibers and half of the nylon thread length L, the initial muscular length l_0, the effective length of the

muscle l, the initial angle α_0, the effective angle α, the initial radius at the center of the muscle r_0 and the effective radius in the middle of the muscle r (figure 5.2).

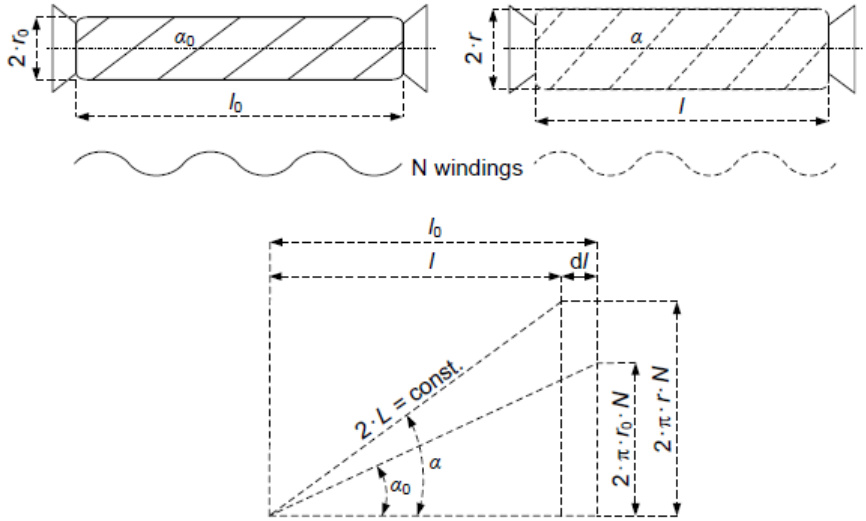

FIGURE 5.2: Correlation between geometric parameters of fluid muscle [16]

Muscles of this type are those produced by the Shadow Robot of London which will later be characterized. For stadard measurements of these muscles it is possible to represent their operating points as a function of their contraction and thus generate the static operating characteristic. Characteristics of pressure, length and force for a muscle with a diameter of 20 mm, active length 210 mm and a weight of 40g are given below:

TABLE 5.1: Percentage contraction of active length for 210 mm air muscle

Pressure	0 [kg]	5 [kgf]	10 [kg]	15 [kg]	20 [kg]	25 [kg]
0 bar	N/A	8%	6%	2%	1%	0%
2 bar	35%	29%	23%	17%	12%	10%
4 bar	36%	33%	29%	25%	23%	20%
6 bar	37%	34%	31%	29%	26%	24%

The tensile force generated by the muscle decreases with increasing contraction under constant pressure. The maximum strength that the muscle can exert at a given pressure is obtained when the muscle is pulled out as much as possible, and if the muscle is not tense it will not produce all its strength. So if the muscle is not totally stretched at the beginning of its movement then the initial strength will be lost and the muscle will undergo a significant useful strength reduction. The relationship between force and pressure is linear at constant extensions, by adjusting the system pressure it is possible to adjust the distance of movement. In figure 5.3 the static characteristic of the muscle

in which the force is reported vs length, contraction and variation in length respectively.

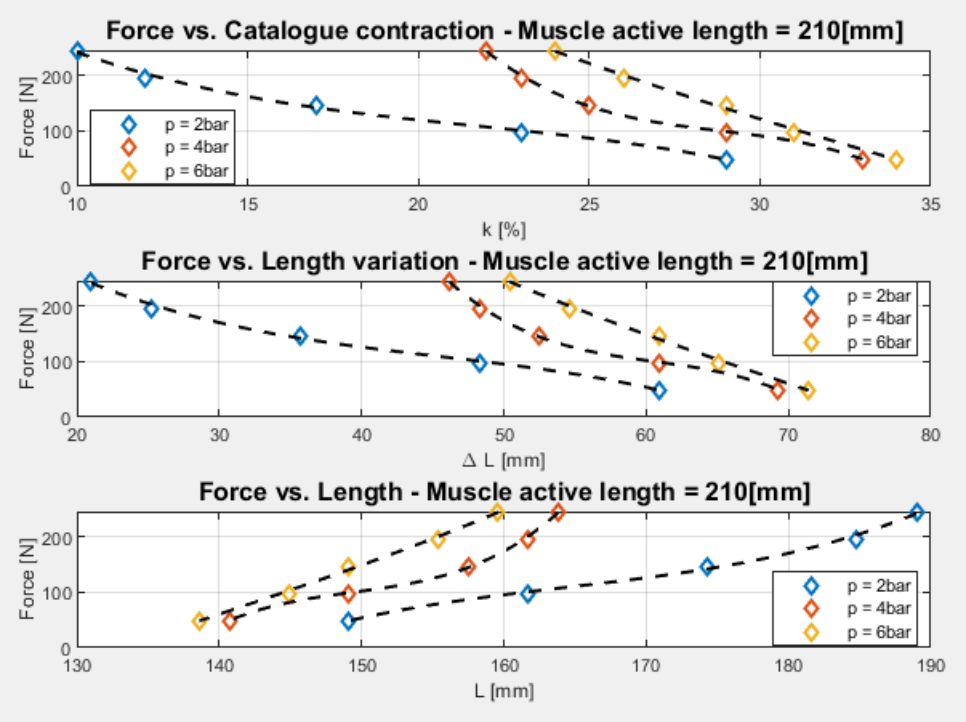

FIGURE 5.3: Shadow Robot muscle force vs. contraction, force vs. length and force vs. length variation

5.1 Approximation of static characteristics of pneumatic muscle

In the literature there are several basic approximations for the description of the static characteristics of a pneumatic muscle. An approximation is then used through an exponential function characterized by two variables with six coefficients, with a determination coefficient R = 0.9996, and is therefore an excellent approximation of the static characteristic [16].

Force F depends on muscle contraction k and constant pressure p, equation 5.1 [25]:

$$F(k,p) = (a_1 p + a_2)e^{(a_3 k + a_4)} + (a_5 p + a_6)k + a_7 p + a_8 \tag{5.1}$$

Equation 5.1 has universal application for different pressures, in order to reduce the number of parameters the force also can be calculated with an approximation algorithm with only six different unknown parameters [25]:

$$F(k,p) = (a_1 p + a_2)e^{a_3 k} + a_4 kp + a_5 p + a_6 \tag{5.2}$$

where a_1, a_2, a_3, a_4, a_5 and a_6 are unknown coefficients which values are also found using Matlab Curve Fitting Toolbox [25] or through genetic algorithms

[16] and are shown in the table 5.2, while k is muscle contraction and p is pressure.

TABLE 5.2: The values of coefficients from 5.2 of Fluidic Muscle type MAS-20-200N using Matlab Curve Fitting Toolbox [25]

Coefficients	Values
a_1	0.11210
a_2	263.70000
a_3	-0.35150
a_4	-0.08619
a_5	2.62400
a_6	-245.60000

The result of approximation according to equation 5.2 of the static characteristics of Fluidic Muscle type MAS-20-200N by FESTO is shown in figure 5.4 and 5.5 for an active length of 400mm, created using Matlab.

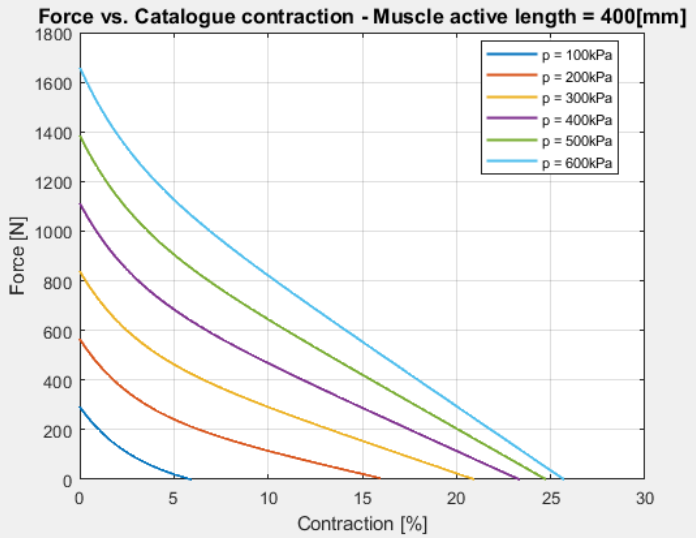

FIGURE 5.4: Force-contraction relation approximated by (5.2) for various pressures (type MAS-20-200N by FESTO - active length 400mm)

While approximated surface is shown in figure 5.6 created using Matlab.

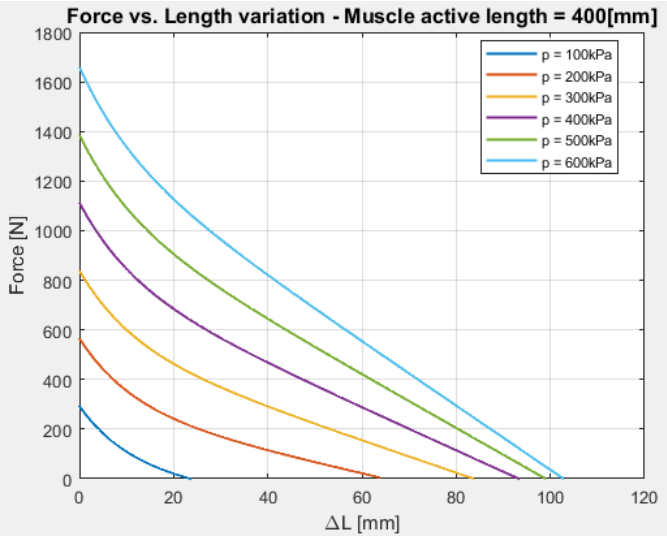

FIGURE 5.5: Force-length variation relation approximated by (5.2) for various pressures (type MAS-20-200N by FESTO - active length 400mm)

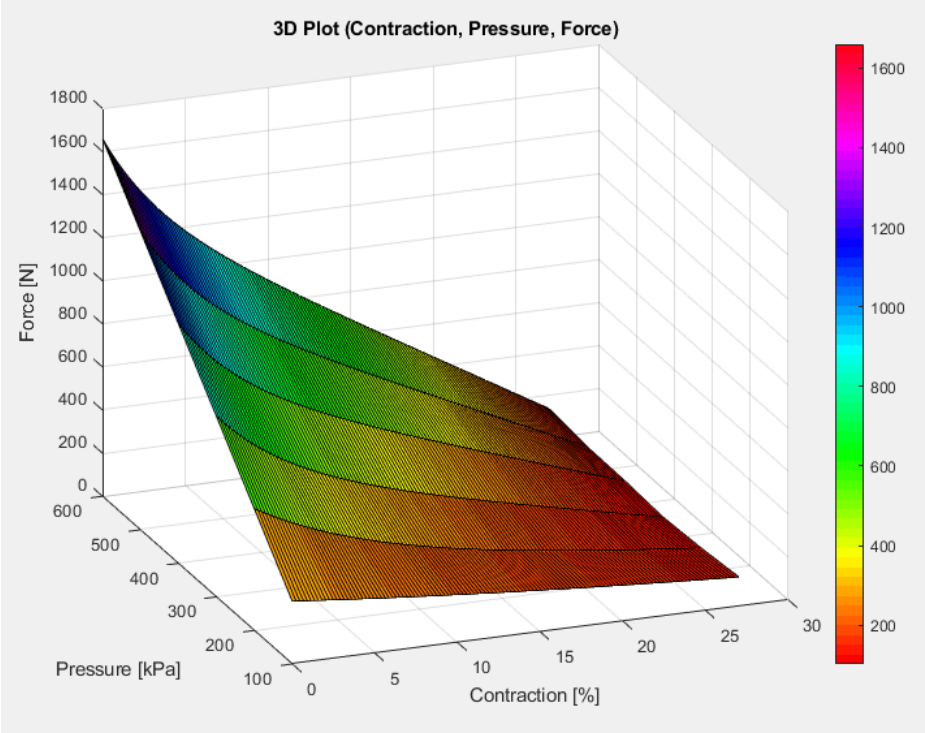

FIGURE 5.6: Force-contraction-pressure relation approximated by (5.2)

Chapter 6

Supporting geometry and pulley-cable modeling

6.1 Mechanical design

In order to carry out a rough dimensioning of the main components of the exoskeleton, a 3D CAD model is provided, realized through SolidWorks, software used in the mechanical and industrial design sectors for the creation of three-dimensional prototypes.

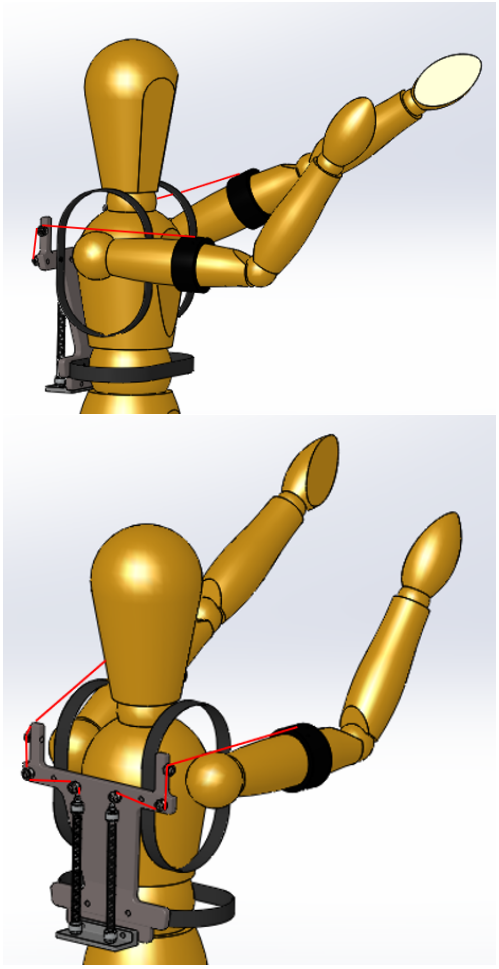

FIGURE 6.1: CAD model

Through the CAD model (figure 6.1) it is possible to obtain a first global view of the device and its main features:

- The pneumatic actuators, positioned in the rear part of the structure, act directly on the arm through a rotary joint;
- The transmission of motion takes place via cable transmission.

In figure 6.2 it is possible to observe in greater detail the cable transmission through pulleys transmission.

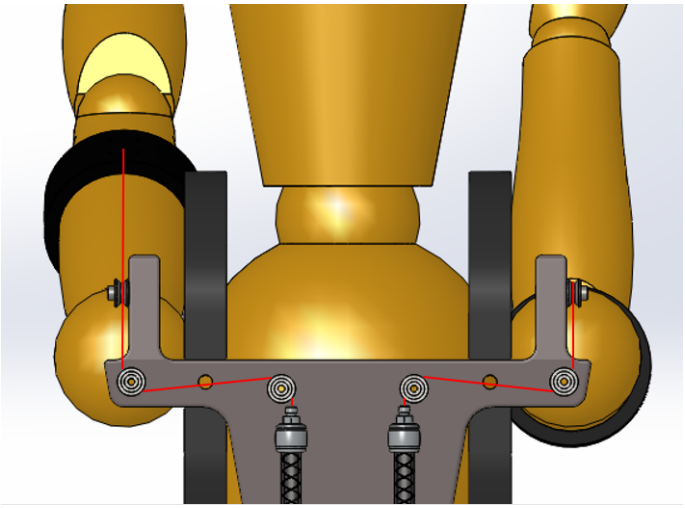

FIGURE 6.2: CAD model - Transmission pulleys with ropes

6.2 Supporting geometry modeling

The characteristic of the fluidic muscles turns out to be opposite to the desired one, since we know that these muscles work exclusively in traction, to achieve the compensation of gravity, these must extend in the extension or abduction of the shoulder and facilitate the phases of flexion or adduction. As the basis for the exoskeleton project, the target motions are defined by imposing the rotations that it can control through the active joints:

1. Flexion/extension and Abduction/adduction of the shoulder (θ_1 angle) from 90° to 125°, in particular the Abduction/adduction of the shoulder is controlled by the same joint through horizontal flexion/extension from outside to forward (and forward to outside) of the shoulder

2. Flexion/extension of the elbow (angle θ_2) from 0° to 150°

With reference to figure 6.3, the characteristic quantities of the system will be defined below. They will follow the represented schemes of only the quantities of interest to facilitate the understanding of the system.

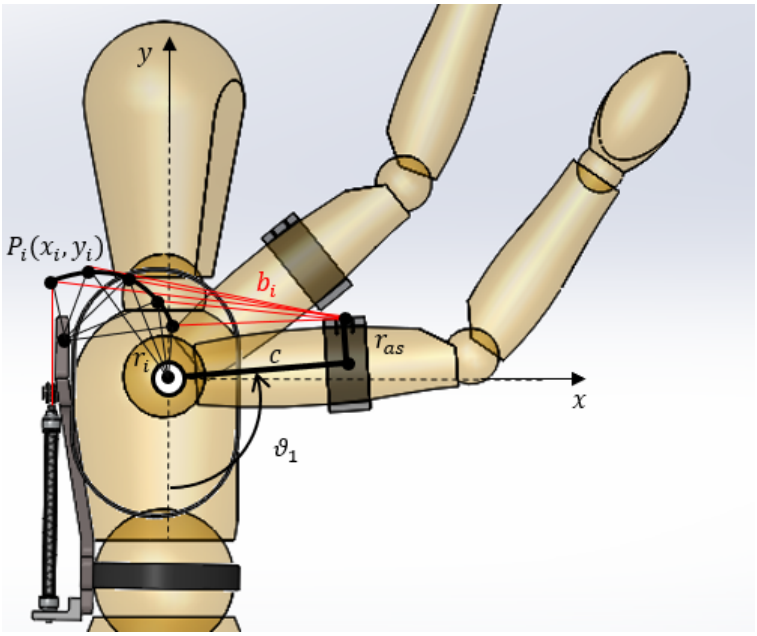

FIGURE 6.3: Representation of the system with respect to the operator who wears it. The points P_i represent the points of tangency of the wire with respect to the geometry sought, while the quantity c is the point of attachment of the cable in tension along the humerus with respect to the point of tangency, θ_1 the characteristic angle of elevation of the arm in the different planes, r_{as} is the radius of the arm support, finally b is the tension cable

Considering the maximum static torque to be balanced, a project recovery percentage is defined as p_r parameter. Since the exoskeleton is passive, the control of which must be guaranteed to the operator. It is required that the

design torque to be balanced does not exceed a limit set at 80% of the total torque, thus leaving 20% of the operator's sustained torque (project conditions).

$$p_r = 80\% \tag{6.1}$$

With respect figure 6.4, the static equilibrium results

$$m_{arm} g l_g cos(\theta_i)(1 - p_r) + F(k,p) c cos(\gamma_i - 90 - \theta_i) - m_{arm} g l_g cos(\theta_i) \leq 0 \tag{6.2}$$

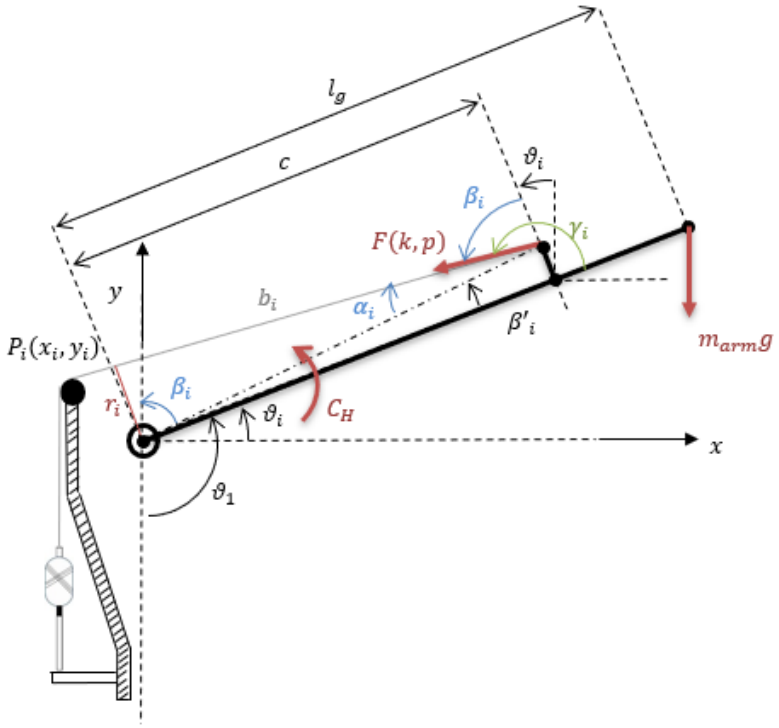

FIGURE 6.4: Static equilibrium of the system with respect to a generic point P_i of the geometry sought. In red the characteristic parameters of the static equilibrium, in blue and black, indicate the internal and external quantities to the triangles respectively, useful in the geometry characterization

Where θ_i is the elevation angle of the shoulder, m_{arm} is the human arm mass, c' is the attack distance of the cable with respect the shoulder joint and c is the distance between the arm support and the shoulder joint, instead

$$r_i = c' cos(\alpha_i - 90 - \theta_i) \tag{6.3}$$

is the useful radius of the geneated torque. So, the useful radius can be written as (from 6.2):

$$r_i \leq \frac{m_{arm} g l_g p_r cos(\theta_i)}{F(k,p)} \tag{6.4}$$

The graphic methods for designing and/or tracing the profile of the geometry of interest are based on the repeated drawing of the different configurations assumed by the mechanism during its movement. For graphic requirements it is useful to imagine that the geomtry is fixed with respect the shoulder joint, while the arm rotates around it. The profile obtained will be given by the envelope of the subsequent positions taken by the connection cable to the rotation of the arm (Figure 6.5). The geometry of the wire support can be determined in various ways. In particular, we want to get points by drawing the geometry in different positions, drawing the point of tangency of the wire with the surface of the geometry. To accomplish this operation, the points of tangency of the individual thread are traced an characteristic angle φ_i with respect to the horizontal axis. From simple geometric considerations, the γ_i angle relative to kinematic inversion can instead be derived as:

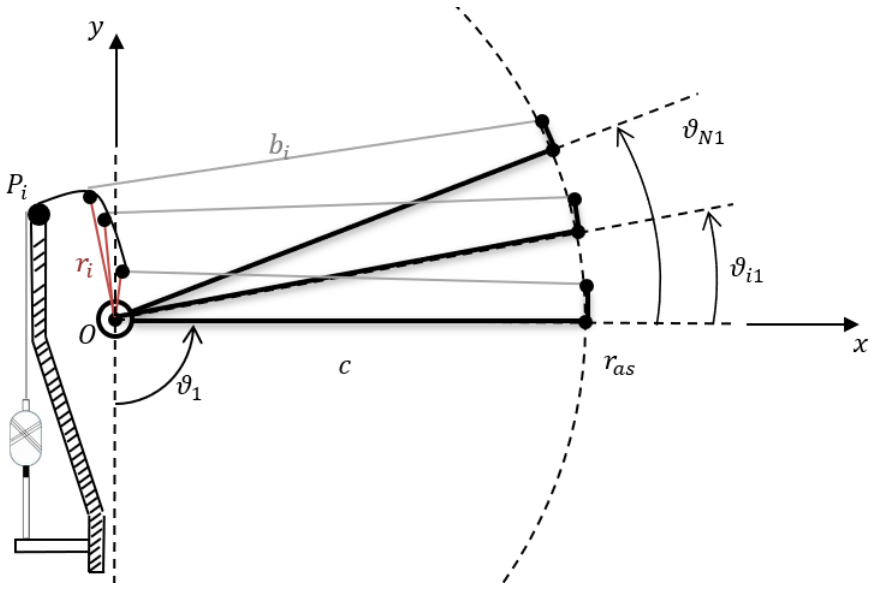

FIGURE 6.5: Three different system positions with indication of the different points of tangency of the wire on the support geometry. The radius re useful in the generation of the moment is indicated with the red color

$$\gamma_i = acos(\frac{p_r m_{arm} g l_g cos(\theta_i)}{F(k,p)c}) + 90 + \theta_i \tag{6.5}$$

By analyzing the system (figure 6.6), one can express the relations that link the right-angled triangles with sides r, c' and b. From simple geometric considerations the following relations are derived:

$$b_i = \sqrt{c'^2 - r_i^2} \tag{6.6}$$

$$\beta_i = asin(\frac{b_i}{c'}) \tag{6.7}$$

$$\alpha_i = 180 - \gamma_i - \beta_i \tag{6.8}$$

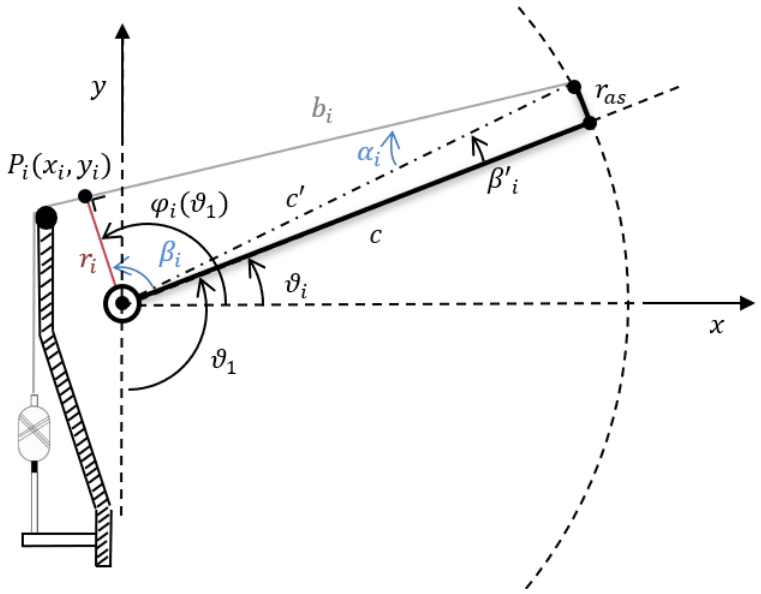

FIGURE 6.6: Triangle i-th description. The rotation of the arm around the shoulder joint varies the area with particular reference to the dimensions ri and bi, respectively the arm of the moment and the length of the cable with respect to the point of tangency

$$\varphi_i = \theta_i + \beta_i + \beta'_i \tag{6.9}$$

The polar coordinates of the system with respect to the origin of the axes are therefore

$$\begin{cases} r_i = \dfrac{p_r m_{arm} g l_g cos(\theta_1)}{F(k,p)} \\ \varphi_i = \theta_i + \beta_i + \beta'_i \end{cases} \tag{6.10}$$

And instead the cartesian coordinates result

$$\begin{cases} x_i = r_i cos(\varphi_i) \\ y_i = r_i cos(\varphi_i) \end{cases} \tag{6.11}$$

Therefore, considering a plane curve which is a graph of a function, the function y=f(x) with x$\in$ $[p_1,p_2]$, f(x) must be derivable and its equation for calculating the length is

$$\zeta(f, [p_1, p_2]) = \int_{p_1}^{p_2} \sqrt{1 + f'(x)^2} dx \tag{6.12}$$

The main input data are show in table 6.1.

By imposing design contractions (figure 6.7), due to the different working pressures, depending on the minimum and maximum working force, the trend of the arm was obtained, useful for generating the required torque according to equation 6.4 .

TABLE 6.1: main model INPUT data

Data	Value
ras - arm support radius [cm]	5
pr - torque recovery rate [%]	80
c - cable connection distance [cm]	20

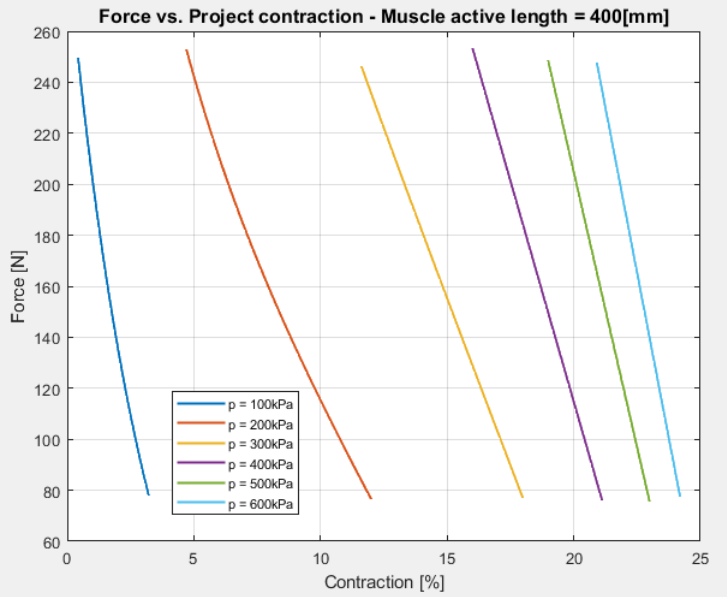

FIGURE 6.7: FESTO muscle - design contractions

To which correspond the variations of length of the muscle reported in figure 6.8.

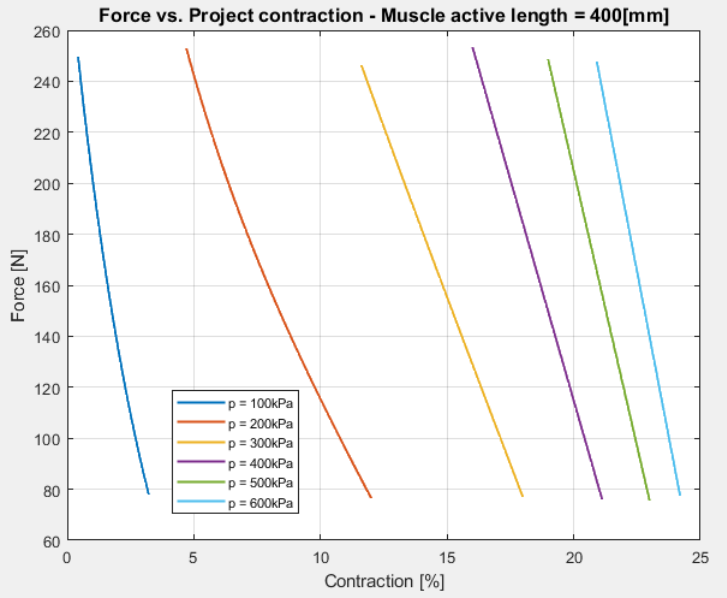

FIGURE 6.8: FESTO muscle - design length variations

The useful arm for generating the compensation moment is shown in figure 6.9 for the different working pressures.

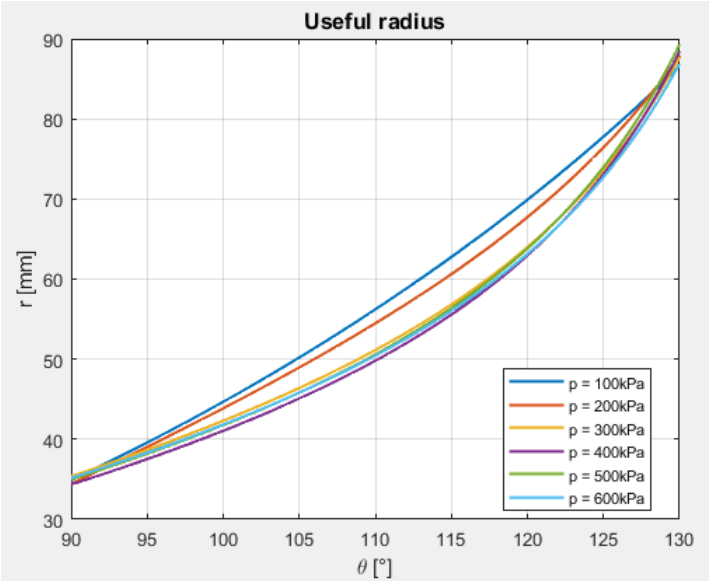

FIGURE 6.9: Useful arm for compensation pair

While the variation in the length of the cable with respect to the point of tangency with the support geometry is shown in figure 6.10.

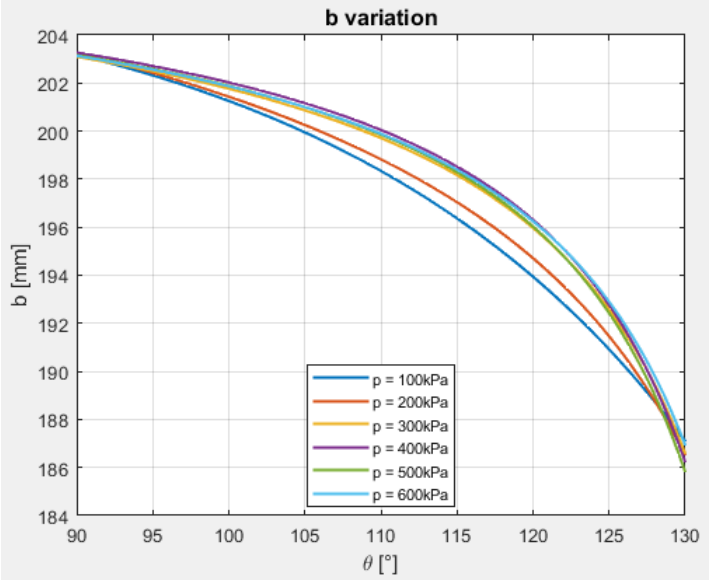

FIGURE 6.10: Cable change in length

Therefore, 6 possible geometries have been obtained, shown in figure 6.11. Excluding geometries with a convex nature, which cannot be physically coupled with the cable that should be placed on them, the geometries generated at the reference pressures of 100kPa and 200kPa are chosen.

The geometries were approximated through 4th degree polynomials with equations in the form

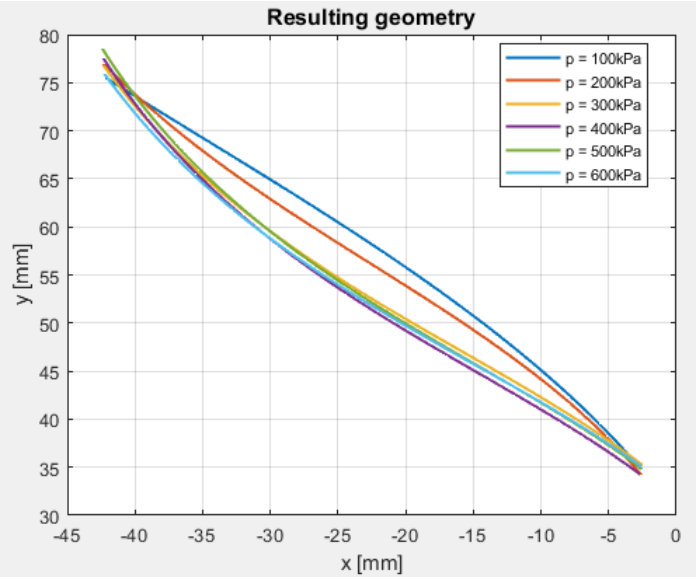

FIGURE 6.11: Resulting support geometry for different pressures

$$y_{th} = C_0 + C_1 x_{th} + C_2 x_{th}^2 + C_3 x_{th}^3 + C_4 x_{th}^4 \tag{6.13}$$

The coefficients were obtained through the MATLAB polyfit function 6.2 .

TABLE 6.2: 4th degree polynomial coefficients

C	100kPa	200kPa	300kPa	400kPa	500kPa	600kPa
C_4	-0.4391E-05	-0.3660E-05	0.3404E-05	0.5247E-05	0.5615E-05	0.3644E-05
C_3	-0.6365E-03	-0.8214E-03	-0.1791E-03	-0.0566E-03	-0.0272E-03	-0.1489E-03
C_2	-0.0352	-0.0440	-0.0148	-0.0105	-0.0097	-0.0130
C_1	-1.7480	-1.7740	-7.0850	-1.0234	-1.0177	-1.0299
C_0	30.5459	30.0183	32.6699	31.6795	32.3968	32.5522

Through the surface integral (equation 6.12) the lengths of the curves can be calculated (table 6.3).

TABLE 6.3: Lengths of the geometries [mm]

Lengths [mm]	100kPa	200kPa	300kPa	400kPa	500kPa	600kPa
ζ	57.0062	58.2800	57.7475	59.1710	59.4765	57.2783

It is therefore possible to calculate the variation in the useful length of the cable (equation 6.14) due to the contraction admitted by the muscle (table 6.4).

$$dl_u = \zeta_i + b_i(1) - b_i(N) \tag{6.14}$$

The new operating contractions are shown in figure 6.12, choosing the geometry obtained at a pressure of 100kPa.

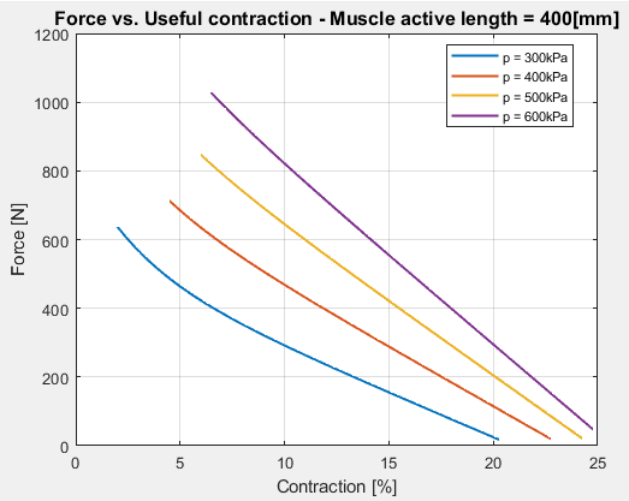

FIGURE 6.12: FESTO muscle - useful contractions

TABLE 6.4: Useful lengths variation [mm]

Lengths [mm]	100kPa	200kPa	300kPa	400kPa	500kPa	600kPa
dl_u	73.0908	75.0463	74.2494	76.2254	76.8356	73.4764

Finally, by comparing the length of the cable with the active length of the muscle (equation 6.15), it is possible to obtain the maximum percentage of contraction, and then check the range of functioning of the muscles in conjunction with useful contractions, functions of work pressure.

$$k_{max} = \frac{dl_u}{Muscle_{al}} 100 \tag{6.15}$$

Resuming the equation of the static equilibrium of the system (equation 6.2), and inserting the new contractions of work it is necessary to increase the range of functioning of the hypoised project, this mains that the initial forces are much higher than those of the project and therefore, compensation pairs too high (figure 6.13).

But the variations obtained (table 6.4) lend themselves well to the penmautical muscles of Shadow Robot as the range of force delivered by the muscle similar to that of design for FESTO muscles.

Finally, it is possible to define a torque recovery coefficient due to gravity compared to that actually compensated, whose trend is shown in figure 6.15.

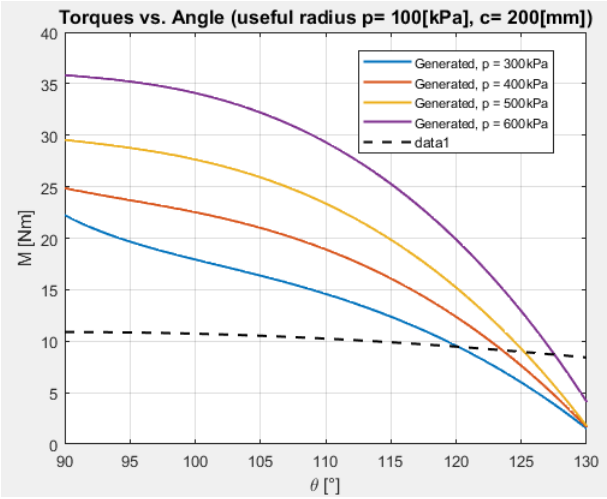

FIGURE 6.13: Moment due to gravity and FESTO muscle Moment gravity compensations

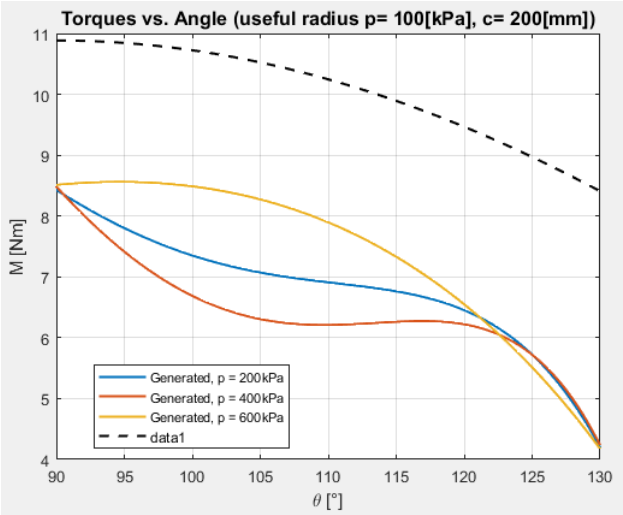

FIGURE 6.14: Moment due to gravity and Shadow Robot msucle Moment gravity compensations

There is an 80% recovery in the maximum torque situation (90° arm position), with a gradual recovery reduction up to 50% at the end of the mobility camp.

Analyzing the equations 6.10 and 6.6 for the Shadow Robot muscle in our possession with the design contractions shown in table 5.1 we obtain the following the results highlighted in figures 6.16 and 6.17.

The resulting geometry turns out to be (figure 6.18):

Also in this case the geometries were approximated through 4th degree polynomials, expressed in the form

$$y_{th} = C_0 + C_1 x_{th} + C_2 x_{th}^2 + C_3 x_{th}^3 + C_4 x_{th}^4 \tag{6.16}$$

And the coefficients (table 6.5) have been generated with MATLAB polyfit function.

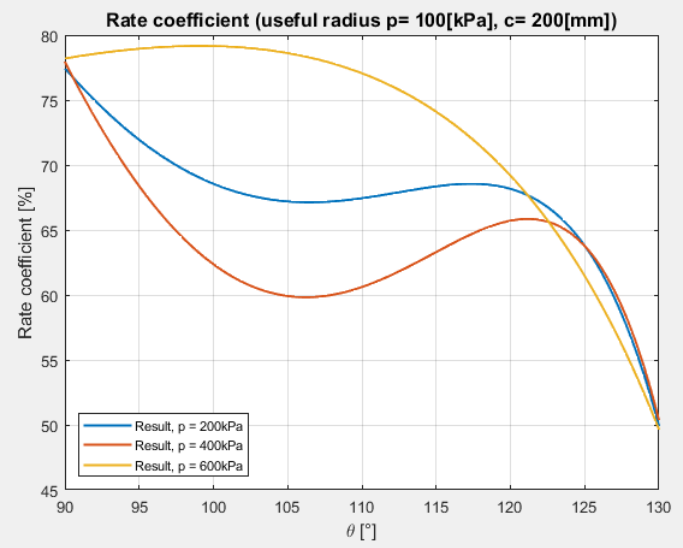

FIGURE 6.15: Recovery rate

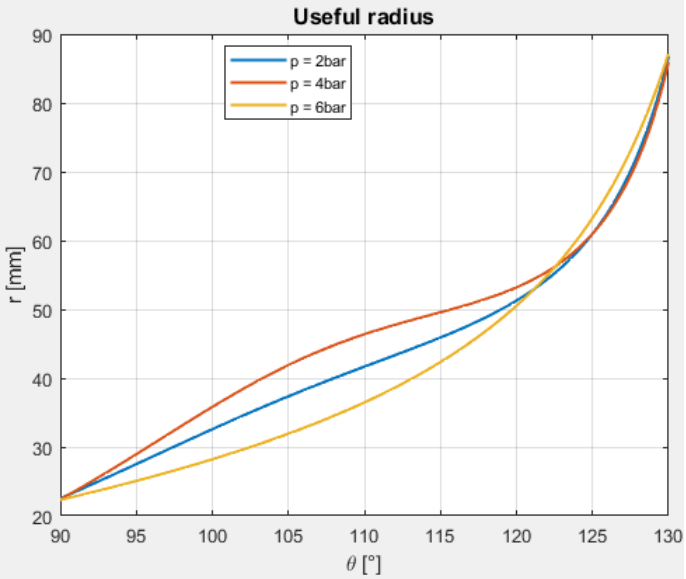

FIGURE 6.16: Shadow roboitcs muscle - useful radius

TABLE 6.5: Shadow Robot - 4th degree polynomial coefficients

C	2 bar	4 bar	6 bar
C_4	0.0181E-04	0.0297E-04	0.1220E-04
C_3	-0.0017	-0.0024	0.003
C_2	-0.1047	-0.1626	-0.0027
C_1	-2.7127	-3.9480	-1.0273
C_0	15.2604	11.3220	19.2038

The geometries lengths (equation 6.12) for the different pressures are shown in table 6.6.

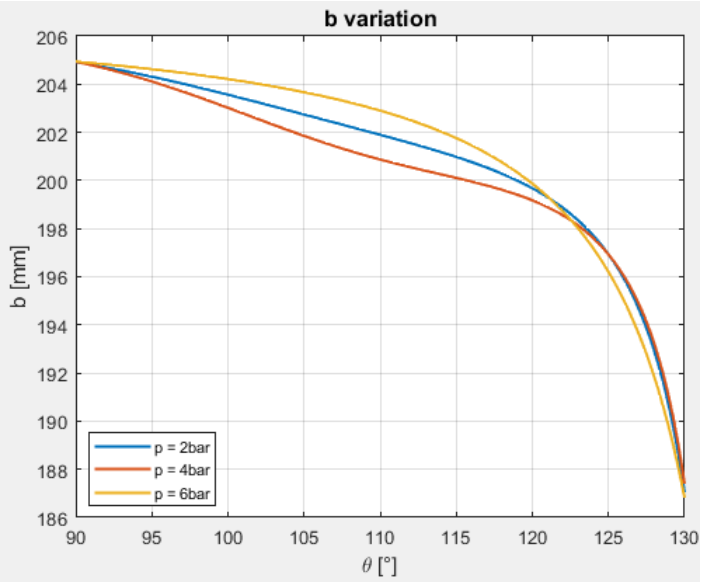

FIGURE 6.17: Shadow roboitcs muscle - Cable change in length (b) varition

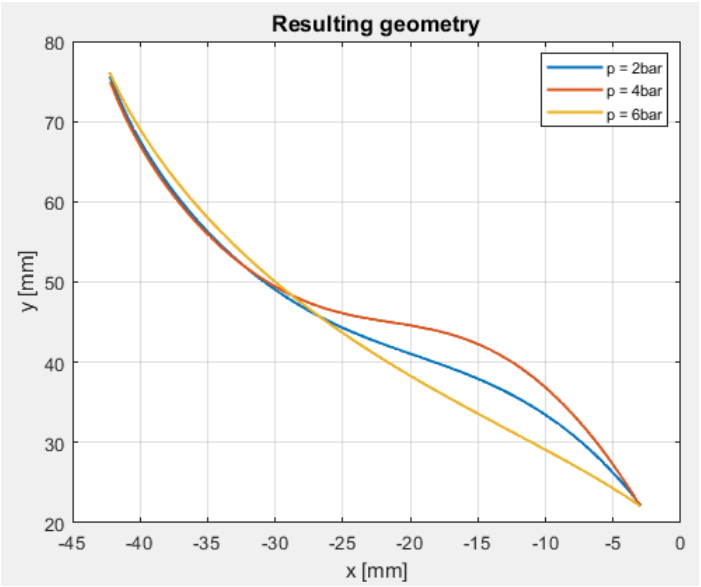

FIGURE 6.18: Shadow roboitcs muscle - Resulting geometry

TABLE 6.6: Shadow Robot - Lengths of the geometries [mm]

Lengths [mm]	2 bar	4 bar	6 bar
ζ	151.5406	201.1336	69.2056

Instead, the variations in the useful length of the cable with respect to the various geometries and pressures are shown in table 6.7.

Therefore none of all the geometries obtained allow a muscle contraction of about 4 cm.

TABLE 6.7: Shadow Robot muscle - Useful lengths variation [mm]

Lengths variation [mm]	2 bar	4 bar	6 bar
dl_u	169.4254	218.6926	87.3416

6.3 Pulley-Cable sistem modeling

With reference to figure 6.19, the characteristic quantities of the system will be defined below. They will follow the represented schemes of only the quantities of interest to facilitate the understanding of the system.

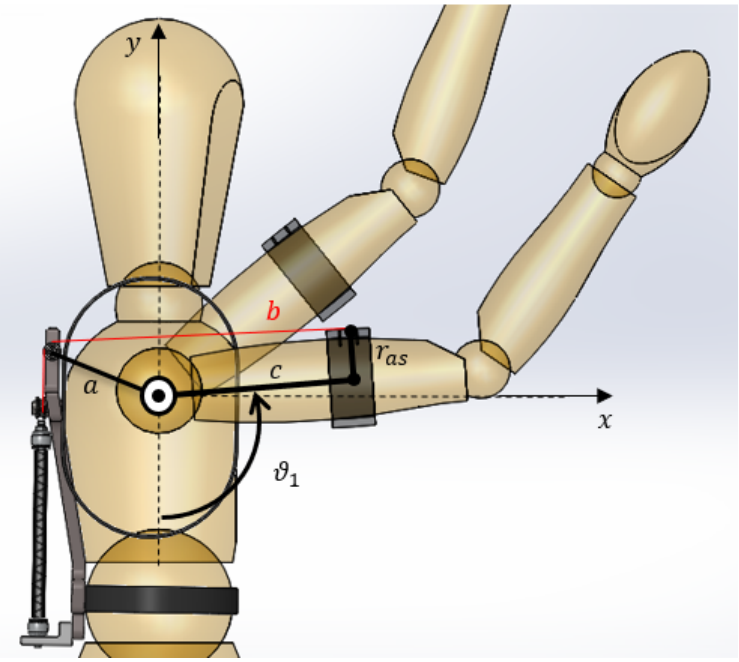

FIGURE 6.19: Representation of the system with respect to the operator who wears it. Dimension a is the distance of the pulley with respect to the center of rotation of the humerus, while the quantity c is the point of attachment of the cable in tension along the humerus, θ_1 the characteristic angle of elevation of the arm in the different planes, r_{as} is the radius of the arm support, finally b is the tension cable

Since the use of a support ageometry was not useful for the proposed purposes, a simpler model was proposed based on the definition of a fixed support point for the connection cable between muscle and human arm. The following model was therefore proposed (figure 6.20):

Where r_{sa} is the attachment distance with respect to the axis of the operator's arm, and β is the characteristic angle of the thread attachment point with respect to the shoulder joint, a is the distance between the pulley joint and the shoulder joint, fixed to the frame, c is the distance between the shoulder joint and the exoskeleton fixing point to the variable user's arm, θ_1 the flexion/extension or abduction/adduction angle of the shoulder, and r is instead the arm of the moment generated by the variable muscle with respect to θ_1 and c. From simple geometric considerations, the equaton of b result:

$$b^2 = c_I^2 + a_I^2 + 2ca_I cos(\theta_1 - \alpha + \beta_I + \beta) \tag{6.17}$$

Where c_I is the distance of the cable attachment point from the shoulder joint; With a_I the distance from the point of attachment of the wire with respect

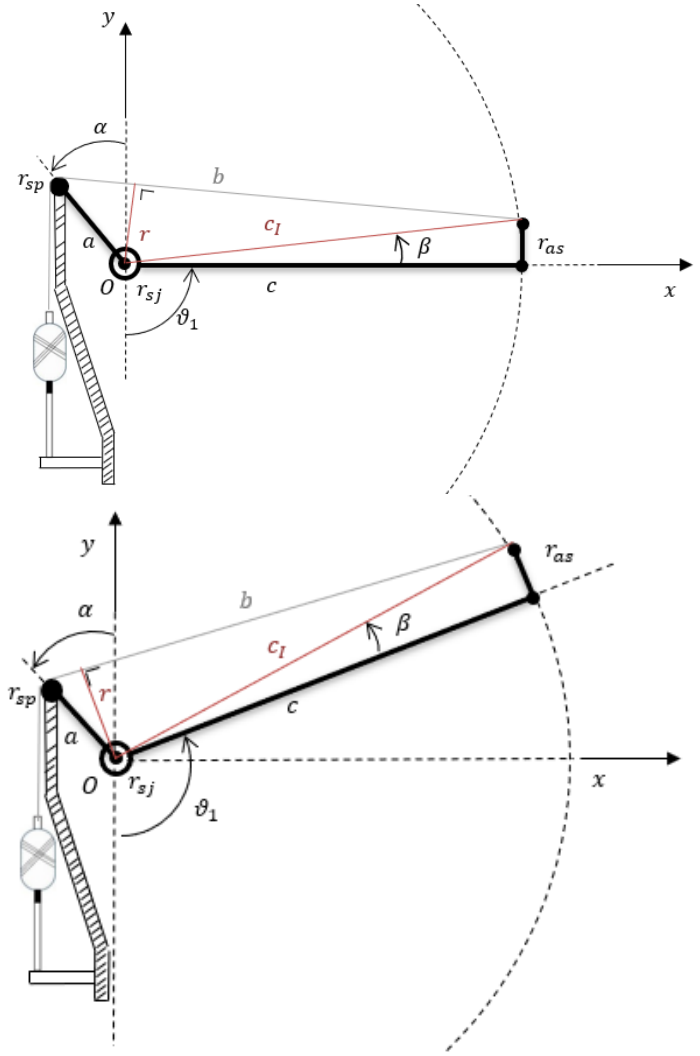

FIGURE 6.20: Representation of the limit configurations of the system (90° - 125°) with respect to the fixed support pulley in the structure located in the back of the individual

to the shoulder joint and β_I is the angle that thisa from with considering the winding of the wire in the support pulley. Through the Heron formulation the semiperimeter and the area of the triangle c, a_I, result

$$A = \sqrt{S(S - a_I)(S - c_I)(S - b)} \tag{6.18}$$

and from the definition of area for a triangle the distance $r(\theta_1)$ results

$$r = 2\frac{\sqrt{S(S - c_I)(S - a_I)(S - b)}}{b} \tag{6.19}$$

In particular, the function b and therefore the useful arm for the transmission of the torque r, are influenced by the relative position of the support arm with respect to the support pulley r_{sp}. Variations of b and r are shown in figures 6.21 and 6.22 for different values of c (point of application of the cable on the upper arm). The input data for the model are reported in table 6.8.

Table 6.8: main model INPUT data

Data	Value
rsp - support pulley radius [cm]	0.7
ras - arm support radius [cm]	5
a - pulley distance [cm]	15
c - cable connection distance [cm]	20, 25, 30
α [°]	80

Depending on the input parameters of the model, in particular of c parameter, there are different variations of the cable useful for the range of motion chosen in the design phase, which are (table 6.9):

Table 6.9: Cable length variation

c [cm]	Cable length variation [cm]
20	4.1
25	4.2
30	4.3

Considering admitted an error on the millimeter in the performed calculations and in the real deformation of the muscle all three choices are possible.

The limit of the fluidic muscles is their compression with respect to the length which is very limited. Not being able to apply a muscle with excessive active length, thus limiting its variation in length to just a few centimeters, it is necessary to activate it only after a defined and controlled theta angle. It is possible to compensate the gravitational effects from 90° to 125° only partially, but almost totally in the most severe phase located at 90° of arm flexion.

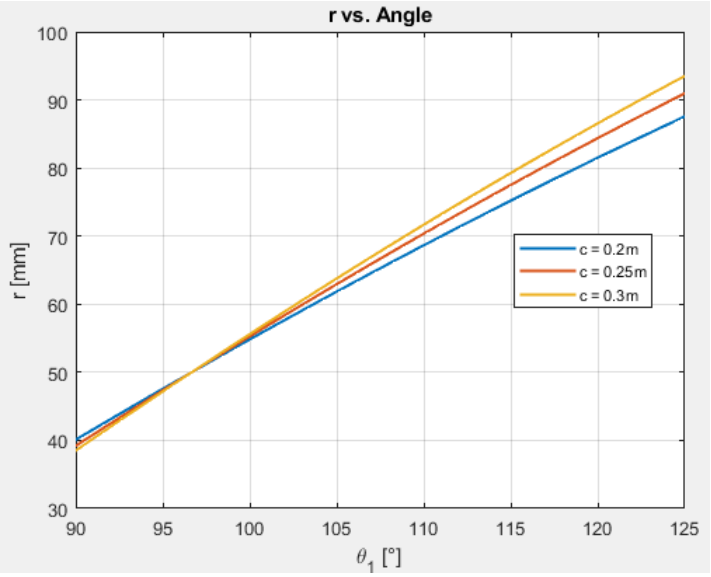

FIGURE 6.21: Moment useful arm vs. θ_1

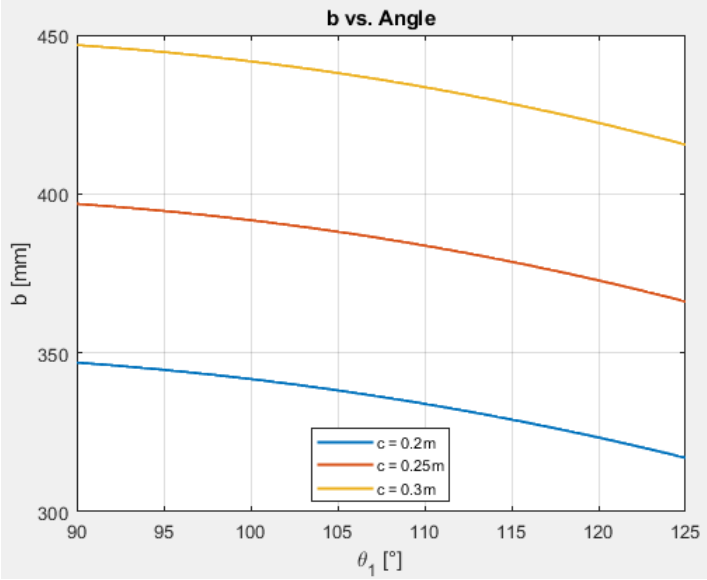

FIGURE 6.22: Cable change in length (b) vs. θ_1 angle

From the characteristics obtained previously regarding the MAS-200N muscles by Festo it is possible to reduce the admissible contractions respect a minimum and a maximum through a contraction correction coefficient c_k, so as to obtain a residual force at the maximum of the contraction and limit the initial pulling force. In particular, defining the maximum contraction allowed by the muscle as a function of the useful variation of the tensioning cable is defined as:

$$k_{max} = \frac{db}{L_a} 100 + c_k \tag{6.20}$$

$$k_{min} = c_k \tag{6.21}$$

Where k_{min} and k_{max} are the maximum and minumum admissible contraction for the muscle, db the variation of length of the cable and L_a the active length of the muscle while c_k on percentage, is the contraction correction coefficient. In terms of length variations for a pneumatic muscle of length 400mm the results are visible in the figure 6.24 and 6.23.

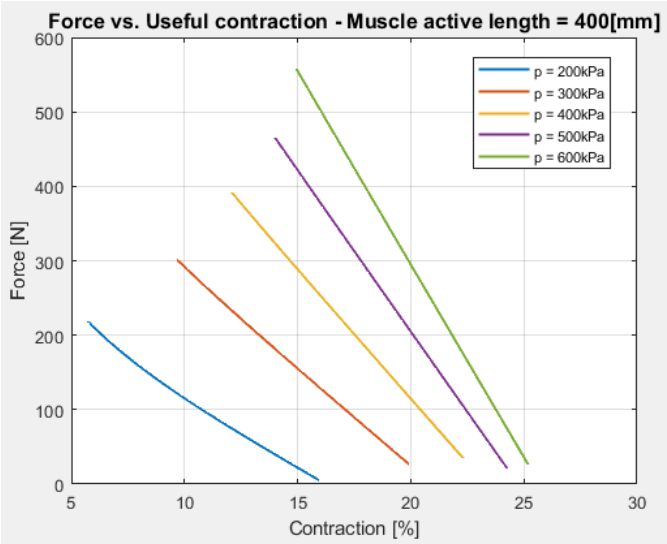

FIGURE 6.23: Useful contraction vs. Force for fluidic muscle FESTO MAS-200N

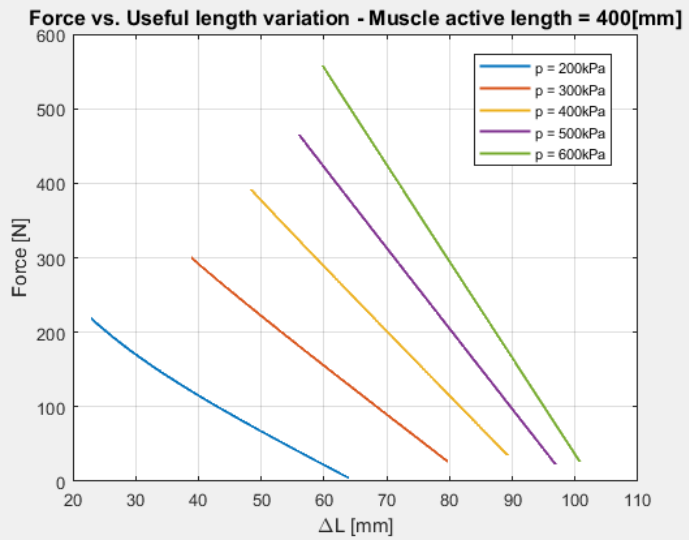

FIGURE 6.24: Change in length from contractions k for fluidic muscle FESTO MAS-200N

The strength of the muscle is transferred to the lifting lever by a rope and pulley mechanism. The figure 6.25 shows the dynamics on the arm.

To find the relationship between the torque generated by the fluidic muscle and the flexion/extension angle of the arm θ_1, the system is modeled as follows:

$$F(k,p)r(\theta_1,\alpha) = I_{arm}\ddot{\theta}_1 + m_{arm}gl_1 sin(\theta_1) - C_H \tag{6.22}$$

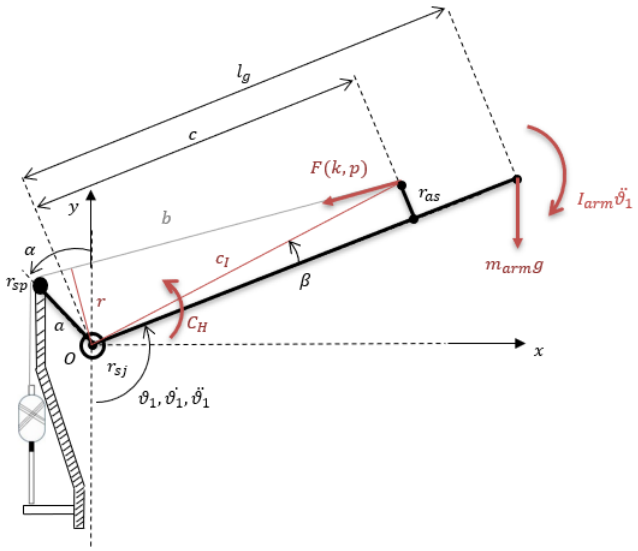

FIGURE 6.25: Dynamic equilibrium of the system with respect the support pulley according to the α angle. In red the characteristic parameters of the dynamic equilibrium, in blue and black, indicate the internal and external quantities to the triangles respectively

$$C_m = F(k,p)r \tag{6.23}$$

With I_{arm} is the human inertia, θ_1 is the elevation angle of the shoulder, C_H is the resulting human torque, m_{arm} is the human arm mass.

Considering the static characteristic of the muscle in our possession (Shadow Robotic, table 5.1) and the main input data (shown in table 6.8), in figure 6.25 is shown the torque due to gravity (black dotted line) with the compensation torque for the value of c chosen on the shoulder joint as a function of shoulder flexion and extension. There is a sub-regulation in which the torque generated by the pneumatic muscles is less than gravity, this is because the arm must tend downward induced by his own weight when muscle stimulation is deactivated. The amount of compensation can be adjusted through the change of the link attachment distance, or in the case of FESTO muscles, in which the change in operating pressure allows not only the variation of the contractions useful to the muscle but also the maximum allowable load, and therefore the pulling force exerted.

Also in this case it is considered the static characteristic of the muscle in our possession (Shadow Robotic, table 5.1) in figure 6.25 is shown the torque due to gravity (black dotted line) with the compensation torque for the value of c chosen on the shoulder joint as a function of shoulder flexion and extension.

Following the new compensation of gravity, the resulting net moment is shown in figure 6.27.

To establish the quality of the model studied, a recovery coefficient is obtained by comparing the torque generated with that to be compensated (figure 6.28). It can be seen how it is possible to compensate the torque very effectively between about 90 and 115 degrees (from 90% to 75% of the total torque) with

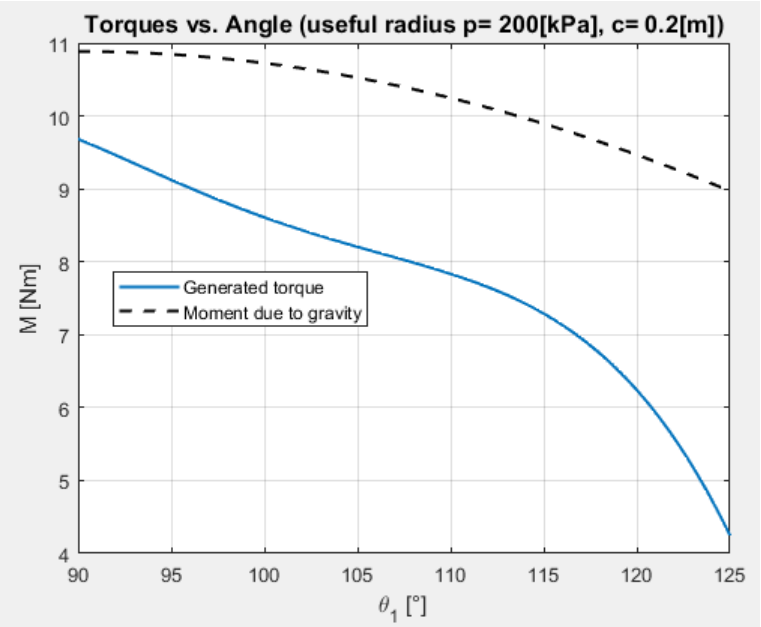

FIGURE 6.26: Moment due to gravity and Moment gravity compensation

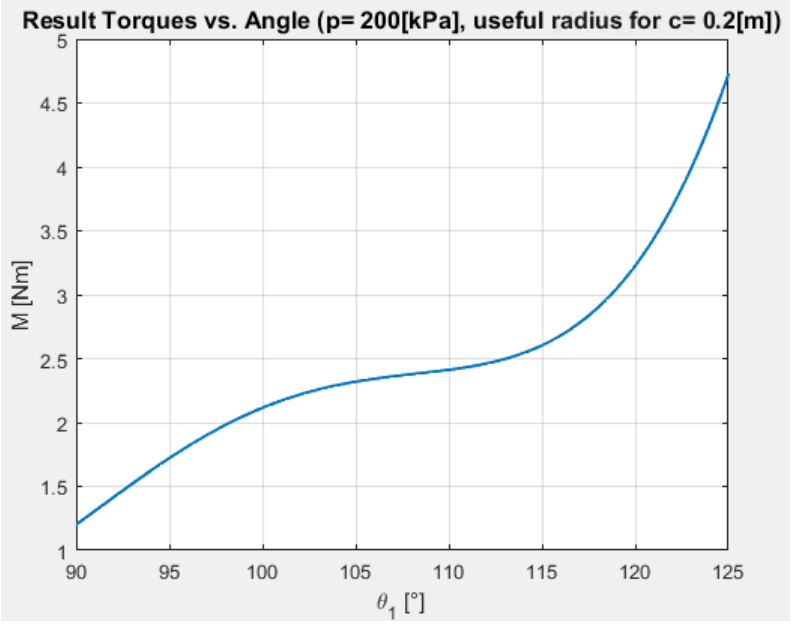

FIGURE 6.27: Torque after gravity compensation

a reduction of up to 50% of the remaining mobility range with a deformation of the muscle of about 4 cm.

The solution with a fixed pulley with respect to the shoulder is the most adequate and simple solution for the objectives set.

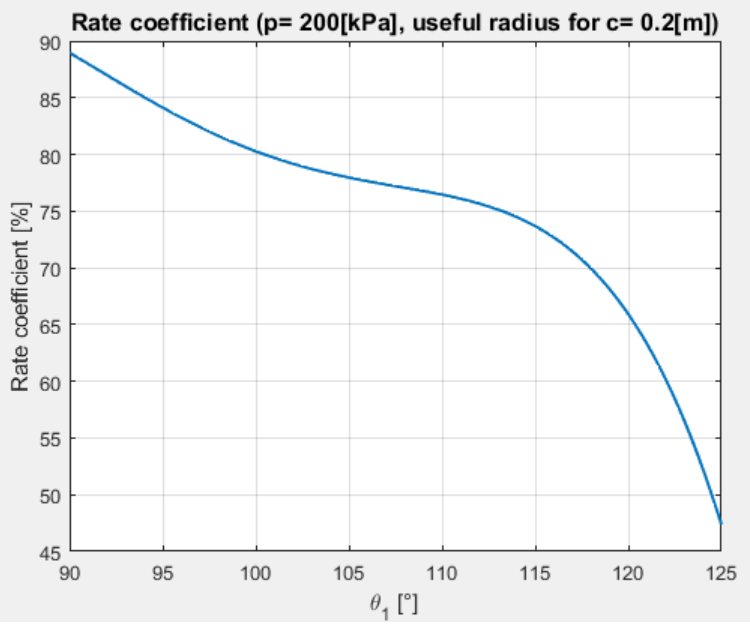

FIGURE 6.28: Recovery Coefficient with 210mm Shadow Robot muscle

6.4 Experimental tests

The measurements were carried out through the definition and construction of a test bench consisting of

- Shadow Robot penumatic muscle (size: 210 mm catalogue active length, 20 mm catalogue diameter)
- Loads (1.3 kg, 2.4 kg, 3.5 kg, 4.5, 5.5 kg), rod weight included (243.8 g)
- Compressed air supply unit
- Measurement scale
- Connecting pipes and splitters
- Non-return valve
- Pressure gauge for pressure check

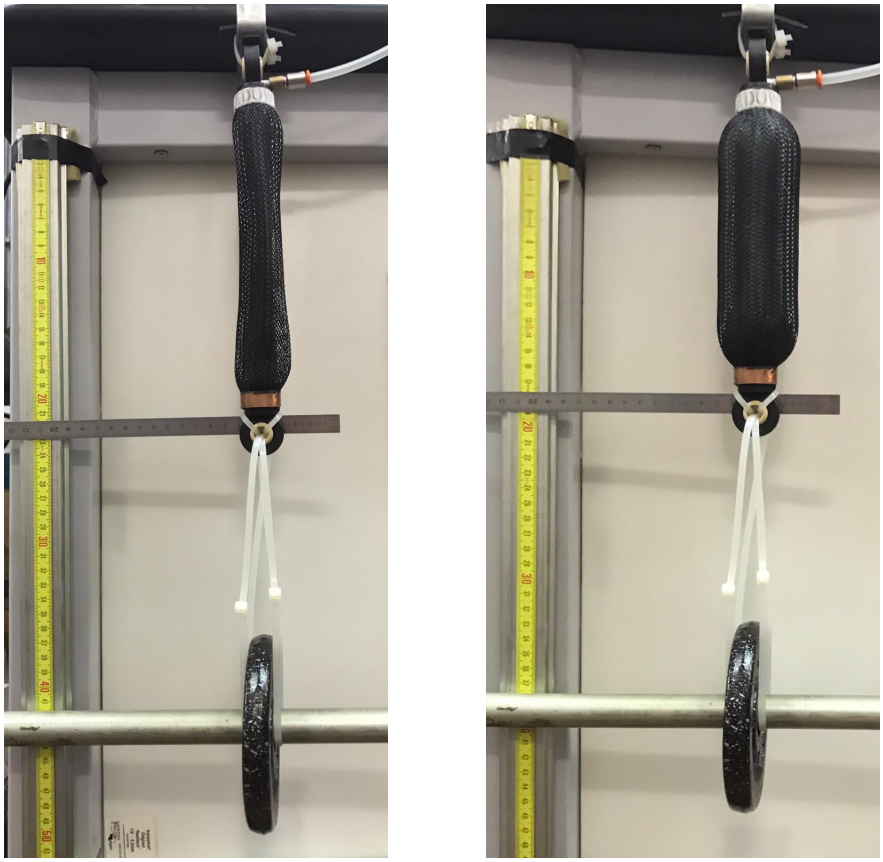

FIGURE 6.29: Test bench - Shadow Robot pneumatic muscle

FIGURE 6.30: Compressed air supply unit

FIGURE 6.31: Pressure gauge

6.4.1 SET 1: Constant load experiments

The first data set was obtained keeping the connection between the muscle and the compressed air generator active. The pneumatic diagram of the test bench is shown in figure 6.32. For each load, the pressure has been increased by 0.5 bar starting from a minimum of 0 bar, up to a maximum of 3 bar. The lengths taken by the muscle for each work pressure and load were read through the measurement scale. The data are shown in table 6.10 and figure 6.33.

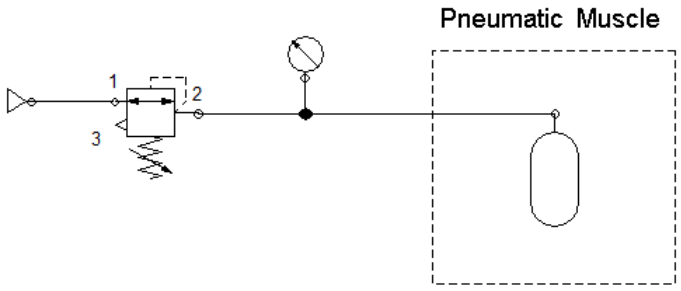

FIGURE 6.32: SET 1: Pneumatic diagram

TABLE 6.10: SET 1: Muscle lengths for different pressures and loads [cm]

Pressure	1.3 [kg]	2.4 [kg]	3.5 [kg]	4.5 [kg]	5.5 [kg]
0 bar	22.9	24.6	28.8	24.9	25
0.5 bar	20.3	20.35	20.5	21.2	21.25
1 bar	18.9	18.95	18.98	19.2	19.4
1.5 bar	18.1	18.3	18.4	18.6	18.7
2 bar	17.9	18	18.05	18.2	18.3
2.5 bar	17.8	17.84	17.89	17.9	18.05
3 bar	17.6	17.7	17.75	17.8	17.85

From the graphs of Figure 6.33, the lengths assumed by the muscle in the different configurations are compared with respect to their initial length assumed for p = 0 bar for each load applied to the end. From the data collected it can be seen how the increase in pressure decreases the allowable contraction of the muscle subjected at the same load, for which it is more efficient.

By imposing the active length of the muscle equal to the maximum length reached under maximum load conditions (table 6.10), the lengths reached by the muscle for the different conditions are compared, the results are visible in figure 6.34.

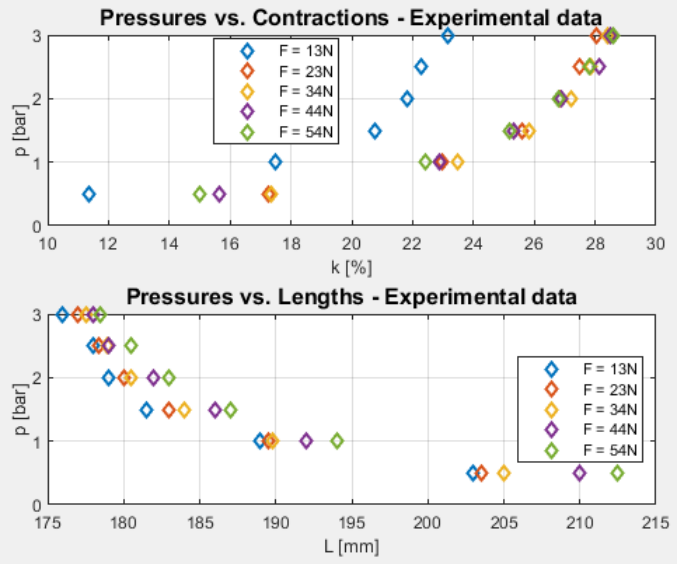

FIGURE 6.33: SET 1 data analysis

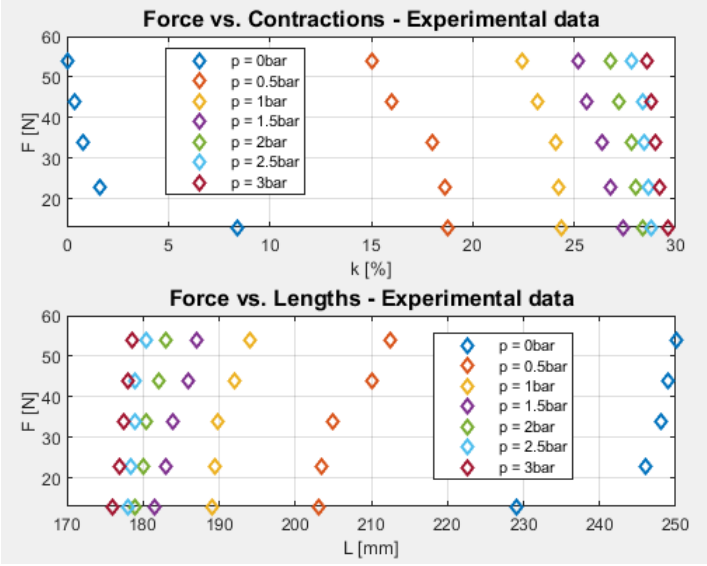

FIGURE 6.34: SET 1 - data analysis (active length 250 mm)

6.4.2 SET 2: Constant air mass experiments

The second set of data was taken by serializing a directional regulating valve, used as a non-return valve, between the muscle and the air generator; after data acquisition, the regulating valve was opened thus emptying the muscle. In addition, a pressure gauge was added between the regulating valve and the muscle to check the actual working pressure. Once the working pressure has been chosen, the non-return valve allows the filling of the muscle; when the muscle is completely full, the generator is switched off, the non-return valve does not allow the passage of compressed air from the muscle to the outlet, thus leaving it under pressure. The pneumatic diagram of the test bench relative to the measurements SET 2 is shown in figure 6.35. For each pressure, the muscle load was increased. The lengths taken by the muscle for each work pressure and load were read through the measurement scale. The data are shown in table 6.11.

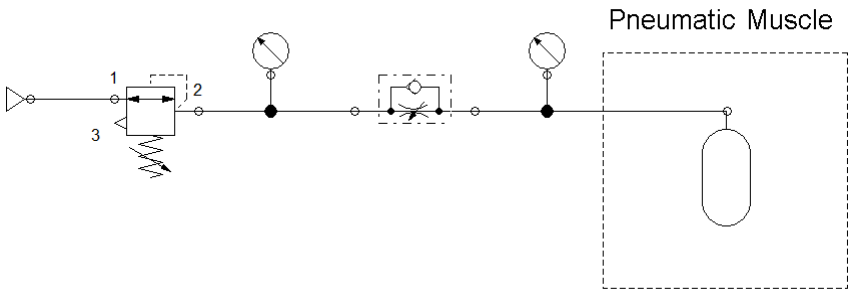

FIGURE 6.35: SET 2: Pneumatic diagram

TABLE 6.11: SET 2: Muscle lengths for different pressures and loads [cm]

Pressure	0 [kg]	1.3 [kg]	2.4 [kg]	3.5 [kg]	4.5 [kg]	5.5 [kg]
0 bar	N/A	22.9	24.6	28.8	24.9	25
0.5 bar	19	19.6	20	20.3	20.6	20.9
1 bar	18.3	18.6	18.9	19.2	19.4	19.6
1.5 bar	18	18.1	18.3	18.5	18.7	18.9
2 bar	17.7	17.9	17.95	18.1	18.2	18.3
2.5 bar	17.6	17.65	17.75	17.85	17.95	18
3 bar	17.3	17.4	17.5	17.6	17.7	17.75

Through the pressure gauge upstream of the muscle, the actual working pressure was obtained. With reference to the data reported in table 6.12, it is made clear that as the load and pressure increase, the muscle tends to increase its losses, as expected. The initial and final pressure shown in the table refer to the unloaded muscle (0 kg) at the beginning and at the end of the test.

TABLE 6.12: SET 2: Real working pressures of muscle for each loads [bar]

I. Pressure	1.3 [kg]	2.4 [kg]	3.5 [kg]	4.5 [kg]	5.5 [kg]	F. pressure
0.5	0.5	0.5	0.5	0.5	0.5	0.4
1	0.95	0.9	0.9	0.85	0.85	0.8
1.5	1.4	1.35	1.3	1.25	1.2	1.2
2	1.95	1.95	1.85	1.8	1.75	1.7
2.5	2.45	2.4	2.3	2.25	2.25	2.2
3	2.95	2.9	2.85	2.8	2.75	2.7

From the graphs of Figure 6.36, the lengths assumed by the muscle in the different configurations are compared with respect to their initial length assumed for p = 0 bar for each load applied to the end.

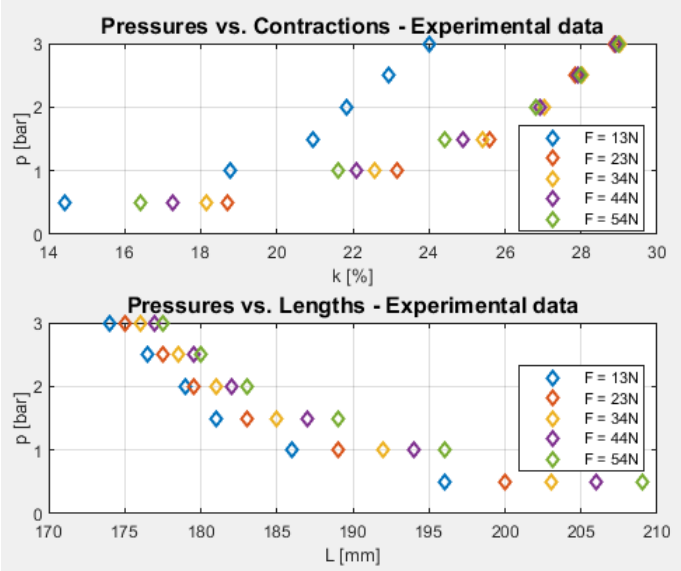

FIGURE 6.36: SET 2 data analysis

By imposing the active length of the muscle equal to the maximum length reached under maximum load conditions (table 6.11), the lengths reached by the muscle for the different conditions are compared, the results are visible in figure 6.37.

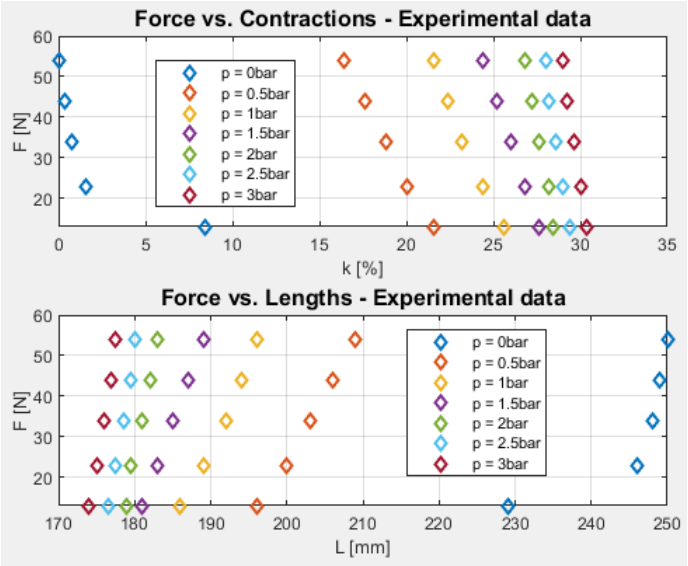

FIGURE 6.37: SET 2 - data analysis (active length 250 mm)

With the aim of highlighting the differences between the two data sets, the characteristic curves for pressures 1, 2 and 3 bar were compared (Figure 6.38).

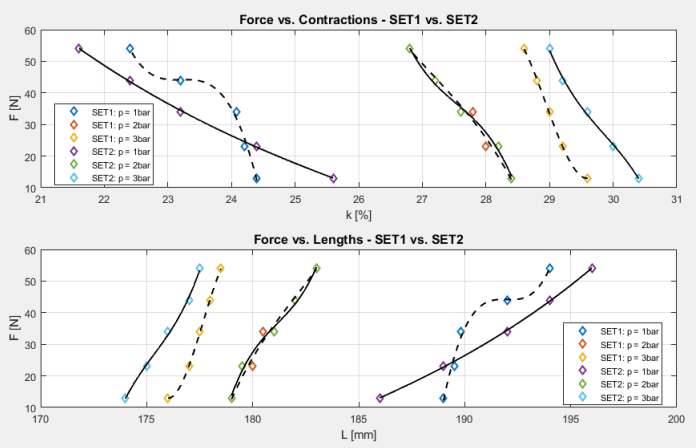

FIGURE 6.38: Comparison between SET 1 and SET 2

Result that the SET2 trends is near to the catalogue characteristic, while the SET1 it stands out more than the trend shown in the catalogue. The curves are non-linear with decreasing trend.

Chapter 7

Conclusions

The improvement of the ergonomic conditions of the operators in the industry is today an important topic in the first place to prevent injuries, but also to facilitate the work of the operator and to improve the efficiency of the production cell.

Currently there are few passive exoskeletons able to fully solve the problem presented, especially for the movement in the entire range of mobility of the arm allowing the correct and free extension of human segments. In particular, we have seen how 5 degrees of freedom are sufficient to describe the movements of the shoulder and the humerus. The first model developed, which is a more rigid system mechanically given the constructive complexity, is currently able to reproduce 4 degrees of freedom of the shoulder allowing for an adjustment of the same and a correction of the position and orientation of the end effector normally following the movement of the operator.

The use of spatial cams, in the case of a cylindrical type, allows a torque recovery that varies from 60% to 98% in an effective working range that varies between 20° and 120°. For the first 20° of the working space, however, movement is still permitted with a resistant torque of less than 3 Nm, which is also variable in the mobility range (up to 20°). The choice of the geometry of the cam and therefore of the law of motion appears to be an important parameter of the system, and for this reason a law of motion with increasing pressure angle has been studied and chosen. The studied system needs lubrication, studied through a pre-sizing of the pins that allow the coupling between motive and transferor in the cam. Given the low speed of the mechanism, it would be sufficient to use a grease.

The static analysis of the system shows that the dimensions and materials chosen for this model with the loads in conditions of maximum stress would generate deformations of the order of a millimeter, considered acceptable for the precision required in this paper.

The pnematic muscles are elastic actuators perfected with respect to their narrow deformation field. The models studied, return a static characteristic of the reliable muscle with respect to the experimental values. The exoskeleton developed with these particular actuators leaves the operator totally free, thus offering a lighter passive exoskeleton that does not generate limitations on human degrees of freedom. However the restricted deformation of the pneumatic muscles allows, with the currently populated system, a mobility field limited to about 40°. The first model has envisaged the search for a geometry that allows to balance the torque due to gravity, however the resulting geometries are not

useful for our purposes, requiring a strictly increasing reason and generating a geometry with a short and steep rise, this does not allow the correct coupling of the wire with the surface of the gemetry in the different points of tangency. For this reason another model has been studied, focused on the search for a single point of support of the wire (through the use of a pulley), the different positions assumed by the arm, with respect to the fixed pulley in the structure, generate the same ray effect. strictly increasing relative to the model with supporting geometry, thus implementing the value of the pair that tried to follow the trend of the Gaussian selected for our study (90° - 125°). The results show a recovery of torque ranging from 90% to about 50% of the value of the initial pair. In particular, the efficiency reduction of more than 65 percent is generated beyond 120°, the solution is useful for our purposes. The system obtained is interesting for its lightness and simplicity, less mechanically rigid than the first model proposed with spatial cams, but with enormous limitations in the range of mobility.

The developed test bench allows to verify the static characteristic of the muscle in the two configurations of constant pressure and constant air mass. The loads used in the test bench are relatively low compared to the loads that the muscle can bear and this explains the restricted deformation of the muscle which is limited to a few millimeters, compared to a maximum allowed deformation of about 4.5 cm as evidenced by the Shadow Robot catalogue. The second configuration of the bench tries to allow to highlight the losses of the muscle when disconnected from the supply unit, and maintained at constant pressure and mass. The losses obtained are mainly attributable to a non-perfect isolation of the mechanical muscle connections, which allow their connection or isolation with the external environment.

One of the biggest limitations of passive exoskeletons that use elastic elements as actuators, is the generation of resistant pairs in the condition of maximum deformation of such elements as shown in the cam device. To solve this problem it is necessary to increase the degree of complexity of the model, a last articulated mechanism has been proposed that can overcome this limitation. The exploitation of the dead points of articulated mechanisms placed in series with each other has been found to be an excellent proposal for lowering the resistant pairs generated in conditions of maximum deformation of the actuators. However, the aforementioned mechanism has exclusively studied the kinematic and dynamic model, defining the main design parameters, but its study has remained primitive and is therefore given in the appendix as a proposal for future research.

This project has opened several topics that can be explored in future work:

- Deepening of the studied models through an adequate experimental activity
- Validation and verification of tests bench and models prototipe
- Metabolic consumption analysis with passive exoskeleton worn by different individuals during mains ones movements

- Report the effects on the subjective comfort of different individuals by the presence and absence of passive compensation joints
- In case of pneumatic actuators a test bench with the maximum permessive load is required in order to evaluate the muscle effective active length
- To investigate the origin of muscle losses in the case of interest (constant air mass) and check the working condition of constant air muscle mass
- In the case of spatial cam mechanism an optimization of the device is required in order to reduce the overall weight of the exoskeleton, the cylindrical cam is the heaviest component, given the coupling of force a cup cam can be inserted
- Deepen the complexity of the model, with the development of a working prototype over the entire range of motion. The articulated mechanism can be a starting point for this purpose

Bibliography

[1] DIN EN 1005-4:2009-01. *Safety of machinery - Human physical performance - Part 4: Evaluation of working postures and movements in relation to machinery.*

[2] ISO 11228-3. *Ergonomics - Manual handling - Part3: Handling of low loads at high frequency.*

[3] S.D. Bagg and W.J. Forrest. "A Biomechanical Analysis of Scapula Rotation during Arm Abduction in the Scapula Plane". In: *Am J Phys Med Rehabil* 67 (1988).

[4] A. Schiele M. D. Bartolomei and F. v. d. Helm. "Towards Intuitive Control of Space Robots: A Ground Development Facility with Exoskeleton". In: *IEEE/RSJ International Conference on Intelligent Robots and Systems (IROS)* (2006), pp. 1396–1401.

[5] CH-P. Chou and B. Hannaford. "Measurement and modeling of McKibben pneumatic artificial muscles". In: *Transaction on Robotics and Automation* 12 (1996), pp. 90–102.

[6] E. Culham and M. Peat. "Functional Anatomy the Shoulder Complex". In: *Journal of Orthopaedic and Sports Physical Therapy* 18.1 (1993).

[7] F. Daerden. "Conception and realization of pleated pneumatic artificial muscles and their use as compliant actuation elements". In: *Vrije Universiteit Brussel* (1999), p. 176.

[8] J. H. van Woensel W. van der Helm F. C. De Groot. "Effect of different arm loads on the position of the scapula in abduction postures". In: *Clinical Biomechanics* 14.5 (1999).

[9] Moeslund T.B. Madsen C.B. Granum E. "Granum E. Modelling the 3D pose of a human arm and the shoulder complex utilizing only two parameters". In: *Computer-Aided Engineering* 12.2 (), p. 1.

[10] Zajac FE. "Muscle and tendon: properties, models, scaling, and application to biomechanics and motor control". In: *Crit. Rev. Biomed. Eng.* 17 (1989), pp. 359–411.

[11] S.G. Doody L. Freedman and C.J. Waterland. "Shoulder Movements during abduction in the Scapular Plane". In: *Arch Phys Med Rehabil* 51 (1970).

[12] Yang L. W.J.A. Grooten and M. Forsman. "An iPhone application for upper arm posture and movement measurements". In: *Appl Ergon.* 65 (2017), pp. 492–500.

[13] Susan Hal. *Basic biomechanics*. 6th edition.

[14] Schiele A Frans C.T. van der Helm. "Kinematic Design to Improve Ergonomics in Human Machine Interaction". In: *IEEE Transaction on Neural Systems and Rehabilitation Engineering* 14.4 (2006), pp. 456–469.

[15] Joseph M. Hidler and Anji E. Wall. "Alterations in Muscle Activation Patterns during robotic-assisted walking". In: *Clinical Biomechanics* 20 (2005), pp. 184–193.

[16] Mária Tóthová Ján Piteľ Alexander Hošovský and József Sárosi. "Numerical Approximation of Static Characteristics of McKibben Pneumatic Artificial Muscle". In: *International journal of mathematics and computers in simulation* 9 (2015).

[17] ISO. *ISO 11226. Ergonomics - Evaluation of static working postures.*

[18] G. Colombo M. Joerg and V. Dietz. "Driven gait orthosis to do locomotor training of paraplegic patients". In: *International Conference of the 22nd Annual EMBS* (2000), pp. 23–28.

[19] Nathan D. Neckel N. Blonien D. Nichols and J. M. Hidler. "Abnormal joint torque patterns exhibited by chronik stroke subjects while walking with a prescribed physiological gait pattern". In: *Journal of NeuroEngineering and Rehabilitation* 20 (2008), 5:19.

[20] J. Miţáková J. Piteľ and M. Tóthová. "Pneumatic artificial muscle as actuator in mechatronic system". In: *Applied Mechanics and Materials* 460 (2014), pp. 81–90.

[21] T. Nef R. Riener and G. Colombo. "Robot-aided neurorehabilitation of the upper extremities". In: *Medical and Biolocial Engineering and Computing* 43 (2005), pp. 2–10.

[22] A. Frisoli F. Rocchi S. Marcheschi A. Dettori F. Salsedo and M. Bergamasco. "A New Force-Feedback Arm Exoskeleton for Haptic Interaction in Virtual Environments". In: *Eurohaptics Conference and Symposium on Haptic Interfaces for Virtual Environment and Teleoperator Systems* (2005), pp. 195–201.

[23] A. Schiele. "Ergonomics of Exoskeletons: Objective Performance Metrics". In: *The 2009 IEEE/RSJ International Conference on Intelligent Robots and Systems* (2009).

[24] A. Schiele and F. v. d. Helm. "Kinematic Design to Improve Ergonomics in Human Machine Interaction". In: *IEEE Transactions on Neural Systems and Rehabilitation Engineering* 14(4) (2006).

[25] J. Sárosi. "New approximation algorithm for the force of fluidic muscles". In: *Proceeding 7th International Symposium on Applied Computational Intelligence and Informatics* 460 (2012), pp. 229–233.

[26] M.M. Stani and C.M. Goehler. "Reproducing human arm motion using a kinematically coupled humanoid shoulder–elbow complex". In: *Applied Bionics and Biomechanics* 5.4 (2008), pp. 175–185.

[27] Robert Riener Tobias Nef. "International Shoulder Actuation Mechanisms for Arm Rehabilitation". In: *Conference on Biomedical Robotics and Biomechatronics* ().

[28] R. Alami A. Albu-Schaeffer A. Bicchi R. Bischoff R. Chatila A. D. Luca A. D. Santis G. Giralt J. Guiochet G. Hirzinger F. Ingrand V. Lippiello R. Mattone D. Powell S. Sen B. Siciliano G. Tonietti and L. Villani. "Safe and Dependable Physical Human-Robot Interaction in Anthropic Domains: State of the Art and Challengess". In: *IEEE International Conference on Intelligent Robots and Systems Beijing* (2006).

[29] Armstrong T.J. A. Burdorf A. Descatha A. F. M. Graf S. Horie W.S. Marras J.R. Potvin D. Rempel G. Spatari E.P. Takala J. Verbeek and F.S. Violante. "Scientific basis of ISO standards on biomechanical risk factors". In: *Scand J Work Environ Health* 44.3 (2018), pp. 232–329.

[30] Zatsiorsky VM. "Kinematics of Human Motion". In: *Champaign, IL: Human Kinetics* (1997).

[31] M. Wehner B. Quinlivan P. M Aubin E. Martinez-Villalpando M. Bauman L. Stirling K. Holt R. Wood. "Design and Evaluation of a Lightweight Soft Exosuit for Gait Assistance". In: *IEEE International Conference on Robotics and Automation* (2012).

[32] Cheng JC Leung SS Chiu BS Tse PW Lee CW Chan AK Xia G Leung AK Xu YY. "Can we predict body height from segmental bone length measurements? A study of 3,647 children". In: *J Pediatr Orthop* 18.3 (1998), pp. 387–93.

[33] Adam Zoss and H. Kazerooni. "Design of an electrically actuated lower extremity exoskeleton". In: *Advanced Robotics* 20:9 (2006), pp. 967–988.

Appendix A

Denavit-Hartenberg Convention (D-H)

The Denavit-Hartenberg Convention (D-H), introduced by Jacques Denavit and Richard S. Hartenberg, is used in robotic applications to select the reference systems of kinematic chains. It allows to represent a geometric transformation in the three-dimensional Euclidean space with the minimum number of parameters, that is four. In this convention every homogeneous transformation is represented by the product of four basic transformations. Starting from the basic link, the links are numbered sequentially from 0 to n and the joints from 1 to n. It is assumed that the joint is at the proximal end of the link i (connects the i link to the i-1 link). Except for the base (i = 0) and the final link (i = n) the frame of the coordinates i (O_i-x_i y_i z_i) is connected to the link i according to the following rules:

- The z axis is aligned with the axis of the joint i, with a positive direction consistent with the degree of freedom of the joint
- Oi origin is at the intersection of the z_i axis with the normal common to the axes z_i and z_{i+1}
- The x_i axis is along the normal common between the axes z_i and z_{i+1} with direction from the articulation i to the junction i+1
- When the axes z_i and z_{i+1} are parallel, the normal common between them is not uniquely defined and the xi axis can be chosen anywhere perpendicular to the two axes of the joint
- When the axes z_i and z_{i+1} intersect, the origin O_i is at the intersection point and the x_i axis is perpendicular to the plane established by the axes z_i and z_{i+1} with arbitrary direction
- The y_i axis is defined so as to complete a right-handed frame

The reference frame 0 is fixed to the base in any convenient position as long as the z_0 axis is aligned with the first axis of the joint (z_1 axis) and, for convenience, the x_0 axis is parallel to x_1 when the degree of freedom of the first joint is zero. The reference frame n is connected to the terminal connection n in any convenient position as long as the z_n axis is aligned with the axis of the

joint n or, for convenience, the x_n axis is parallel to x_{n-1} when the degree of freedom of the joint end n is null.

The Denavit and Hartenberg's parameters are defined as follow:

α_{i-1} twist angle between axes z_{i-1} and z_i. It is the angle required to rotate the axis z_{i-1} into alignment with the axis z_i in the right-hand sense about axis x_{i-1}

a_{i-1} offset distance between axes z_{i-1} and z_i measured along axis x_{i-1}

d_i translational distance between axes x_{i-1} and x_i. It is the distance to translate the axis x_{i-1} into incidence with the axis x_i along the positive direction of axis z_i

θ_i joint angle between the axes x_{i-1} and x_i. It is the angle required to rotate the axis x_{i-1} into alignment with the axis x_i in the right-hand sense about axis z_i

For a revolute joint i, α_{i-1}, a_{i-1}, and d_i are constant link parameters and θ_i is a joint variable to measure the relative location of link i with respect to link i-1. For a prismatic joint i, a_{i-1}, d_i, and θ_i are constant link parameters and d_i is a joint variable to measure the relative location of link i with respect to link i-1.

Appendix B

Articulated mechanism sistem modeling

The previously proposed system, however, does not allow to cancel or limit the torque generated by the actuator in the resting phase of the arm, furthermore due to the poor contraction of the fluidic music with respect to its active length it is possible to limit the compensation action only to a determined very narrow angular opening, reaching a maximum angular lift of the arm of only 120° out of 180 ° . To try to resolve the limits described, a second mechanism is proposed with the following constraints:

1. Increase the angular lift of the shoulder (θ angle) from 0° to 180°, in particular the Abduction/adduction of the shoulder is controlled by the same joint through horizontal flexion/extension from outside to forward (and forward to outside) of the shoulder;

2. Limit the compensated gravity torque from 0° to 90°, covering the residual angle more from 90° to 180° more heavy for the operator;

3. Generate from small displacements (muscle contraction) wide angular displacements with sufficient radii to generate the required torque;

4. Reduce to a minimum the torque generated by the muscle due to zero arm flexion to avoid disturbances during use.

To achieve the aforementioned objectives, the following geometric model in order to define its kinematics has been proposed (figure B.1):
The input data for the model are reported in table B.1.

Table B.1: main model INPUT data

Data	Value
r [m]	0.06
l_{11} [m]	0.08
l_{13} [m]	0.07
l_{23} [m]	0.07
γ_{max} [°]	48

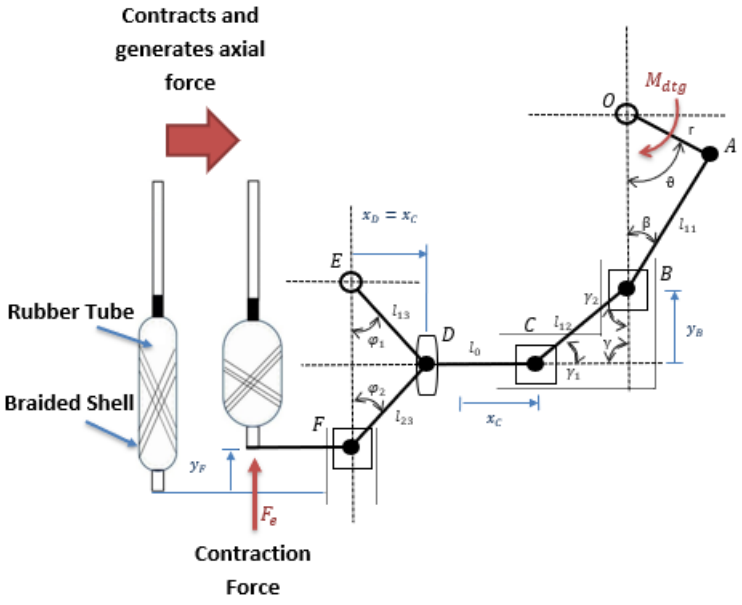

FIGURE B.1: Articulated mechanism model for gravity compensation for flexion/extension angle θ variation

The first system analyzed is a classic thrust rod-crank mechanism capable of transforming a translational motion into a rotary one. The system kinematics is shown in the figure B.2.

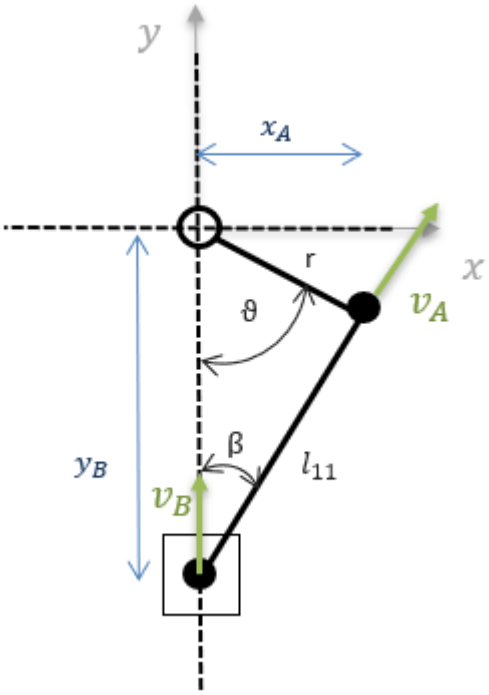

FIGURE B.2: kinematic thrust mechanism 1

In reference to the figure B.2 β is a function of θ given the present kinematic constraints, on the basis of which it is possible to write:

$$\beta = asin(\frac{r}{l_{11}} sin(\theta)) \tag{B.1}$$

The following expression allows instead to calculate the position of the point B along the cordinate y

$$y_B = (r + l_{11}) - (rcos(\theta) + l_{11}cos(\theta)) \tag{B.2}$$

Deriving the equation eqn:beta and eqn:yb:

$$\dot{\beta} = \dot{\theta} \frac{rcos(\theta)}{l_{11}cos(\beta)} \tag{B.3}$$

$$v_B = r\dot{\theta}sin(\theta) + l_{11}\dot{\beta}cos(\beta) \tag{B.4}$$

From which, deriving further the equations B.3 and B.4 , it is obtained

$$\ddot{\beta} = \frac{\ddot{\theta}rcos(\theta) + \dot{\beta}^2 l_{11}sin(\beta) - \dot{\theta}^2 rsin(\theta)}{l_{11}cos(\beta)} \tag{B.5}$$

$$a_B = r\ddot{\theta}sin(\theta) + r\dot{\theta}^2 cos(\theta) + l_{11}\ddot{\beta}sin(\beta) + l_{11}\dot{\beta}^2 cos(\beta) \tag{B.6}$$

The figure B.3 shows the kinematics of the system.

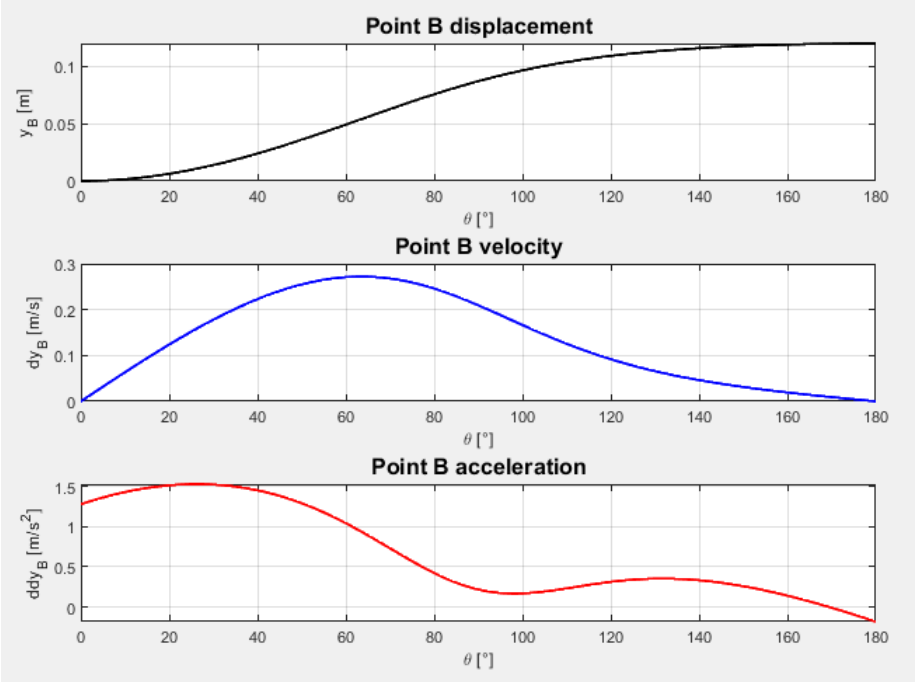

FIGURE B.3: kinematics of point B - mechanism 1

Assuming the hourly moments as positive, respect the figure B.4

$$\delta L_1 = M_{dtg}\delta\theta + V_B\delta y \tag{B.7}$$

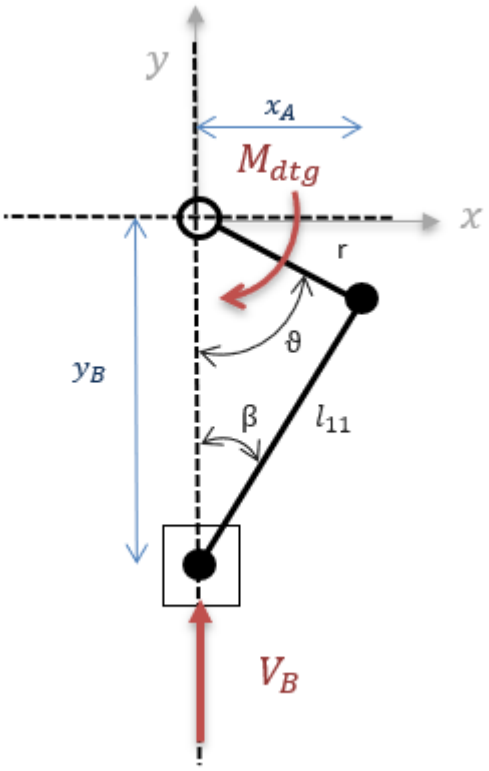

FIGURE B.4: kinematic thrust mechanism 1

$$y_B = -(rcos(\theta) + l_{11}cos(\theta)) \tag{B.8}$$

$$x_A = rsin(\theta) = l_{11}sin(\theta)) \tag{B.9}$$

$$cos(\beta) = \sqrt{1 - sin^2(\beta)} = \sqrt{1 - \frac{r}{l_{11}^2}^2 sin^2(\theta)} \tag{B.10}$$

performing the differentiation operation, remembering that δy_B it is not an exact differential

$$\delta y_B = rsin(\theta)\delta\theta + \frac{r^2}{l_{11}} \frac{sin(\theta)cos(\theta)}{\sqrt{1 - \frac{r}{l_{11}^2} sin^2(\theta)}} \delta\theta \tag{B.11}$$

the virtual work done by the system can be written as

$$\delta L_1 = M_{dtg} + V_B(rsin(\theta) + \frac{r^2}{l_{11}} \frac{sin(\theta)cos(\theta)}{\sqrt{1 - \frac{r}{l_{11}^2} sin^2(\theta)}}) \tag{B.12}$$

and therefore the compensation torque is given by

$$M_{dtg} = V_B r sin(\theta)(1 + \frac{rcos(\theta)}{l_{11}\sqrt{1 - \frac{r^2}{l_{11}^2}sin^2(\theta)}}) \tag{B.13}$$

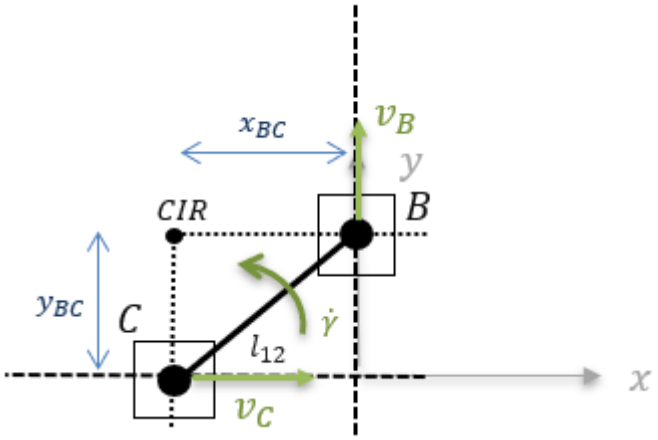

FIGURE B.5: translation mechanism kinematic

From simple geometric considerations it is obtained (figure B.5):

$$y_{BC} = l_{12} sin(\gamma_1) \tag{B.14}$$

$$x_{BC} = l_{12} cos(\gamma_1) \tag{B.15}$$

and for the geometry of the system the linear speeds result

$$v_B = \dot{\gamma} x_{BC} \tag{B.16}$$

from B.20 it is possible to obtain the rotation speed of the rod l_{12}

$$\dot{\gamma} = \frac{v_B}{x_{BC}} \tag{B.17}$$

and v_C results

$$v_C = \dot{\gamma} y_{BC} \tag{B.18}$$

where the linear speeds are related as

$$\frac{v_B}{x_{BC}} = \frac{v_C}{y_{BC}} \tag{B.19}$$

While accelerations can be written as

$$a_B = \ddot{\gamma} x_{BC} \tag{B.20}$$

The angular acceleration of the link results

$$\ddot{\gamma} = \frac{a_B}{x_{BC}} \tag{B.21}$$

and a_C results

$$a_C = \ddot{\gamma} y_{BC} \tag{B.22}$$

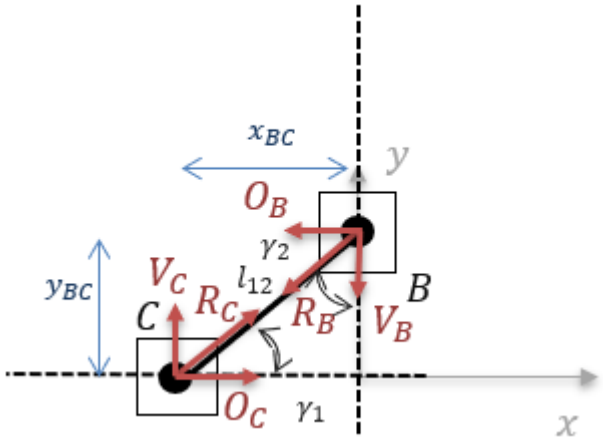

FIGURE B.6: forces exchanged in the system 2

by decomposing the resultant in the hinge C we obtain the force in the horizontal direction coming from the third system

$$\begin{cases} V_C = R_C sin(\gamma_1) \\ O_C = R_C cos(\gamma_1) \end{cases} \tag{B.23}$$

and a_C results

$$V_C = O_C tg\gamma_1 \tag{B.24}$$

for the vertical equilibrium of the forces the vertical component in B results

$$V_B = V_C \tag{B.25}$$

From simple geometric considerations (figure B.7) it is possible to write

$$x_D = l_{13} sin(\phi_1) = l_{23} sin(\phi_2) \tag{B.26}$$

$$y_D = -l_{13} cos(\phi_1) \tag{B.27}$$

$$y_F = -l_{13} cos(\phi_1) - l_{23} cos(\phi_2) \tag{B.28}$$

deriving the equations B.26, B.27 and B.28

$$v_{D,O} = l_{13} \dot{\phi_1} cos(\phi_1) \tag{B.29}$$

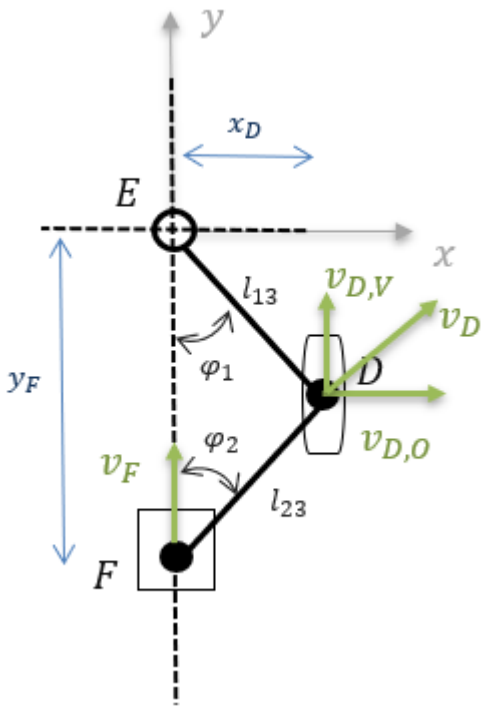

FIGURE B.7: cinematic toggle mechanism 3

$$\dot{\phi_1} = \frac{v_{D,O}}{l_{13}cos(\phi_1)} \tag{B.30}$$

$$\dot{\phi_2} = \frac{v_{D,O}}{l_{23}cos(\phi_2)} \tag{B.31}$$

$$v_{D,V} = l_{13}\dot{\phi_1}sin(\phi_1) \tag{B.32}$$

$$v_F = l_{13}\dot{\phi_1}sin(\phi_1) + l_{23}\dot{\phi_2}^2 sin(\phi_2) \tag{B.33}$$

deriving the equations B.32 and B.33

$$\ddot{\phi_1} = \frac{a_D + l_{13}dot\phi_1{}^2 sin(\phi_1)}{l_{13}cos(\phi_1)} \tag{B.34}$$

$$\ddot{\phi_2} = \frac{a_D + l_{23}dot\phi_2{}^2 sin(\phi_2)}{l_{13}cos(\phi_2)} \tag{B.35}$$

$$a_{D,V} = l_{13}\ddot{\phi_1}sin(\phi_1) + l_{13}\dot{\phi_1}^2 cos(\phi_1) \tag{B.36}$$

$$a_F = l_{13}\ddot{\phi_1}sin(\phi_1) + l_{13}\dot{\phi_1}^2 cos(\phi_1) + l_{23}\ddot{\phi_2}sin(\phi_2) + l_{23}\dot{\phi_2}^2 cos(\phi_2) \tag{B.37}$$

The figure B.8 shows the kinematics of the system.

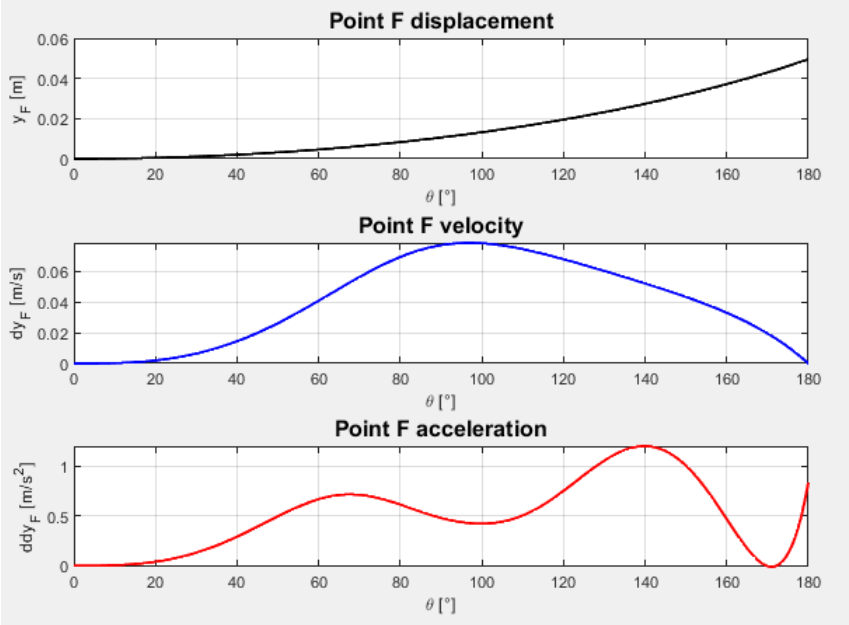

FIGURE B.8: kinematics of point F - mechanism 3

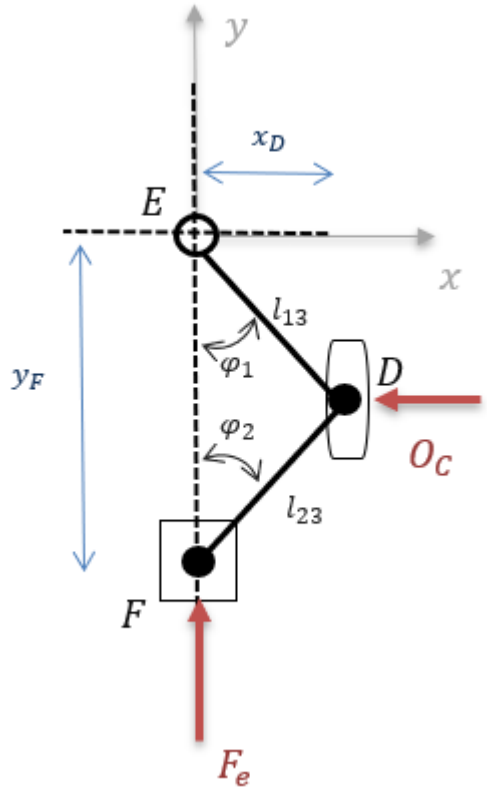

FIGURE B.9: forces exchanged in toggle mechanism 3

With reference to the figure B.9, imposing ϕ_1=ϕ_2 and l_{13}=l_{23}

$$y_F = -2l_{13}cos(\phi_1) \tag{B.38}$$

the virtual work of forces results

$$\delta L_3 = F_e \delta y - O_C \delta x = 0 \tag{B.39}$$

performing the differentiation operation, remembering that δy_F and δx_C are not exact differential

$$\delta x_C = l_{31} cos(\phi_1) \delta \phi_1 \tag{B.40}$$

$$\delta y_F = 2 l_{31} sin(\phi_1) \delta \phi_1 \tag{B.41}$$

the virtual work done by the system can be written as

$$\delta L_3 = F_e (2 l_{31} sin(\phi_1) \delta \phi_1) - O_C (l_{31} cos(\phi_1) \delta \phi_1) = 0 \tag{B.42}$$

the relationship between horizontal and vertical force is

$$O_C = 2 F_e tan(\phi_1) \tag{B.43}$$

Following the same procedure carried out in the simple pulley-cable mechanism obtained the variation of the length of the point F, defining the correction coefficient c_k (equations 6.21 and 6.21) the contractions and variations in useful length are defined where dL is the displacement of point F. In terms of length variations for a pneumatic muscle of length 400mm the results are visible in the figure B.11 and B.10.

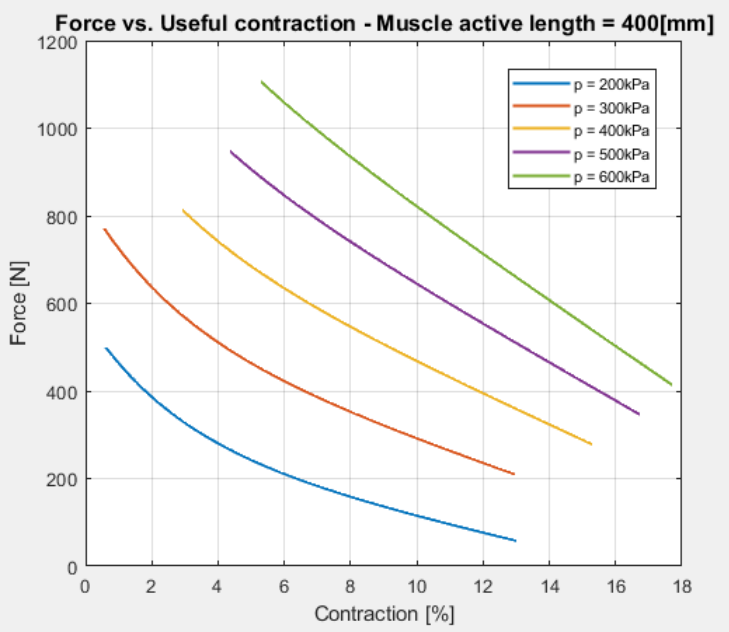

FIGURE B.10: Useful contraction vs. Force for fluidic muscle FESTO MAS-200N

By implementing the models developed on Matlab, the moment of compensation with respect to that generated by gravity with a working pressure of 3 bar and a contraction of the muscle of 5 cm results (figure B.12) Following the compensation of gravity, the resulting net moment is shown in figure B.13.

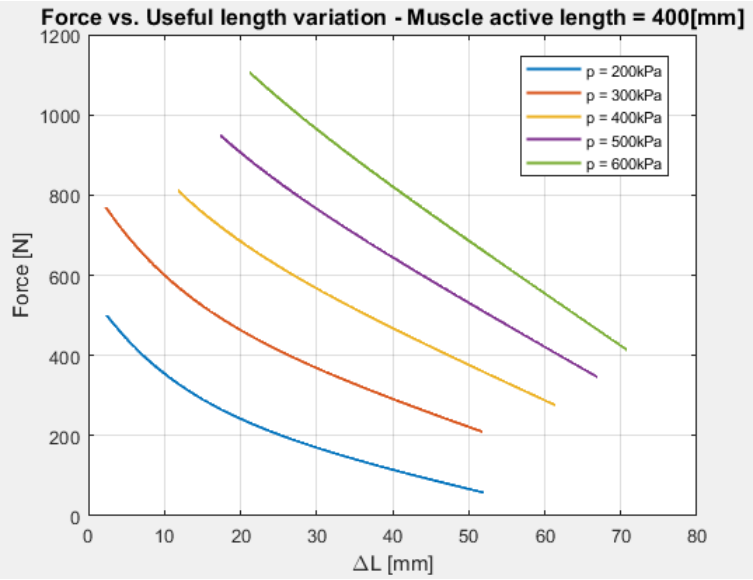

FIGURE B.11: Change in length from contractions k for fluidic muscle FESTO MAS-200N

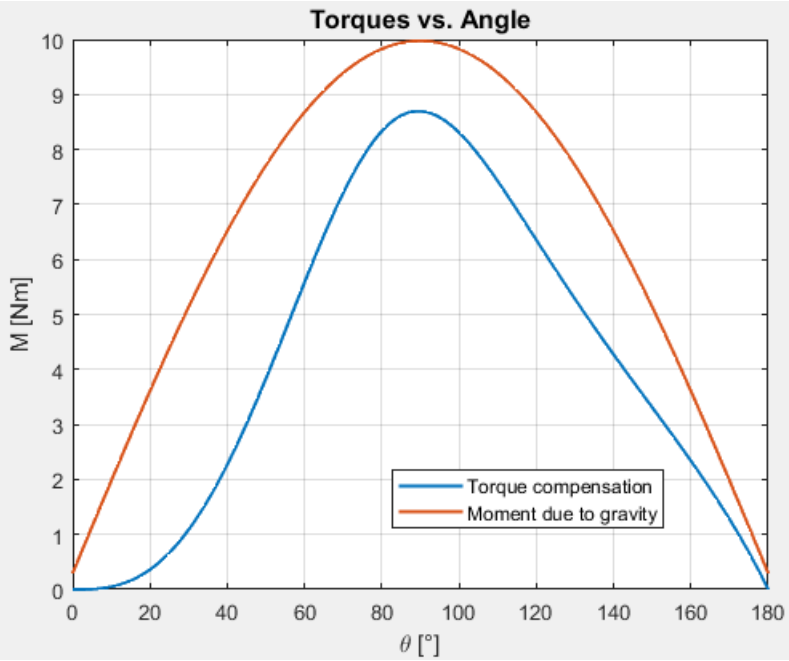

FIGURE B.12: Moment due to gravity and Moment gravity compensation with articulated mechanism

Which softens the remaining moment by dividing it into two curves of different amplitude with minimum point at an angle of 90°. It can be seen how the remaining moment in the most burdensome phase from 90° to 180° was therefore minimized.

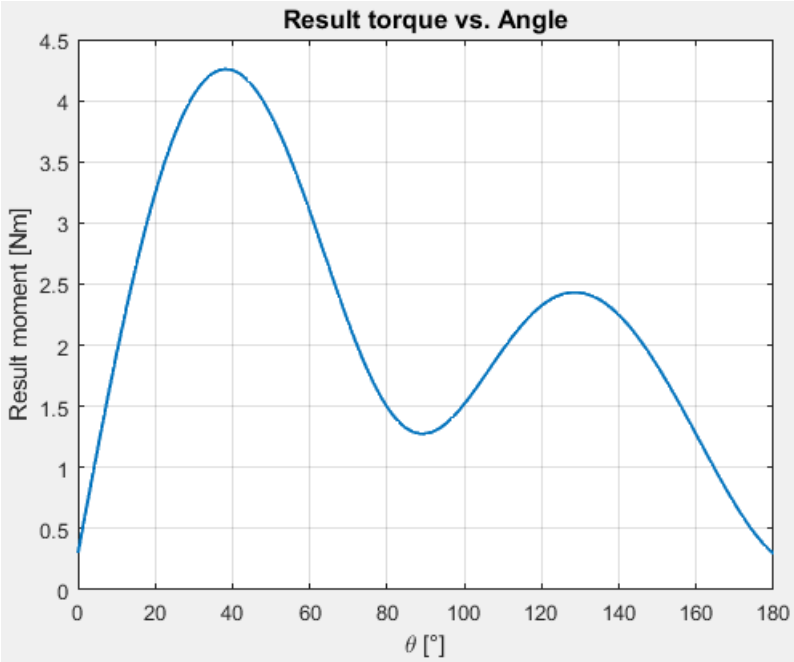

FIGURE B.13: Torque after gravity compensation with articulated mechanism

Appendix C

Materials

The choice of the constituted material of the exoskeleton takes place according to the characteristics that it is desired to confer to it. In particular, an exoskeleton for industrial use must be characterized by:

1. Light. Its weight is discharged directly into the body of the wearer
2. Biocompatible with human beings. Even if its use is external it must not cause any form of reaction in contact with the individual
3. Tenacious, to withstand impacts;
4. Cheap, the product must be easily marketable.

The interface with the user, therefore the part directly in contact with the operator must have different characteristics, such as

1. Soft and comfortable, so that it mates with the user and adapts to the shape of his body without causing injury
2. Breathable to allow cellular breathing of the skin
3. Light
4. Easy disassembly and cleaning

C.1 Materials used in the production of exoskeletons

The materials generally used range from metals, plastics to composite materials. There are many on the market and they can be classified according to their hardness and stiffness:

- The rigid materials are metals, in particular steel, aluminum and titanium, composite materials such as resins, carbon fiber or glass fiber and finally thermoplastics such as polyethylene and polypropylene.
- The semi-rigid materials are low-density polyethylene and rubbers
- The soft materials are sponges, silicones, gels and rubbers

In the following chapter we aim to bring back the metallic, non-metallic and composite materials used in the manufacture of exoskeletons, reporting their fundamental properties.

C.1.1 Metallic materials

Metallic materials, in general, are hard, heavy, malleable, ductile and tanaci; they are good conductors of electricity and heat but vulnerable to wear and external agents causing corrosion with exception of aluminum and obviously stainless steel. In the production of exoskeletons mainly 3 metallic materials are used, such as:

- Steel: low cost, easy to mold, resistant to fatigue but very heavy. is widely used in the construction of joints, shock absorbers and actuators, but we try to use it as little as possible due to its weight;
- Aluminum: much lighter than steel, less resistant than fatigue so it is little used in the joints. Aggregating it with copper, sicilio and magnesium, it forms duralumin which has better performance;
- Titanium: the mechanical characteristics are similar to steel but the weight is considerably lower; it also has good corrosion resistance. However it is difficult to model and its cost is considerably higher than steel.

Table C.1: Main properties of seel

Materials	Steel
Density [kg / m^3]	7500-8000
Tensile strength [MPa]	480-1100
Yield strength [MPa]	205-820
Tensile modulus of elasticity (Young) [GPa]	200-230

C.1.2 Non-metallic materials

Plastic and polymeric materials have adequate characteristics for the production of exoskeletons, in particular they are stable with respect to corrosion and aging, they are light, malleable and therefore easy to model, which allows a considerable reduction in the manufacturing cost and to obtain more complex geometries.

Polymers are distinguishable in three categories:

- Thermoplastic;
- Thermostable;
- Elastomers.

Thermoplastic polymers are composed of very heavy and hard molecules. They are formed by linear or little ramified chains, or non-crosslinked (they

are not linked to each other), it is therefore sufficient to increase the temperature slightly to bring them to a viscous state and then be able to shape and form them. Thermally they can be divided into two categories, low temperature thermoplastics (it is sufficient to increase the temperature below 80 °C) and high temperature thermoplastics (it is necessary to exceed 80 °C to shape them). The former are used little given the low fatigue strength and the applicable force constraints, high temperature thermoplastics are generally used for exoskeletons. they are very resistant to corrosion but have much lower mechanical strength and stiffness than metals. Another drawback is the modification of the properties with the passage of time, in particular the resistant load and the deformation decreasing its stiffness.

Some thermoplastic polymers are reported below:

- ABS Acrylonitrile butadiene styrene
- PLA polylactic acid
- PVC polyvinyl chloride or polyvinyl chloride
- Polyethylene PE
- Polypropylene PP

ABS is a common thermoplastic polymer used to create light and rigid objects. The most important properties are hardness and impact resistance, excellent dimensional stability under low loads. ABS is a copolymer derived from polymerized styrene together with acrylonitrile in the presence of polybutadiene, and therefore can be defined as a terpolymer. The ABS finds great application in the realization of products through the use of rapid prototyping machines that use production techniques such as the FDM (Fused Deposition Modeling). it is widely used in the industrial field as in domestic use. it is a recyclable material, inflammable at high temperatures.

Polylactic acid, or more correctly poly (lactic acid) or polylactate, is a thermoplastic polymer derived from lactic acid. Commonly used through 3D printing (additive manufacturing). it is obtained through the synthesis by fermentation and isolation of L-lactic acid with subsequent polymerization of the acid obtained. The main properties are rheological, ie the melt's elasticity is lower than that of the olefins, which vary from those of an amorphous polymer to those of a semi-crystalline polymer to be more rigid or flexible, hard or soft with different resistances, and biodegradable following hydrolysis at a temperature greater than 60 °C and humidity greater than 20%. The PLA has a much shorter biodegradation time than the classic plastic.

Polyethylene (also known as polythene) is the simplest of synthetic polymers and is the most common of plastics. It stands out in high temperature and low temperature polyethylene. High temperature polyethylene is generally used for splints, busts, masks and accessories for temporary prostheses. it is light and low cost. May cause allergy and reactions in contact with the skin with increased sweating. It has a low fatigue strength, so it is not a good material for prolonged use. Low temperature polyethylene is a semi-rigid plastic, modeled

at temperatures below 80 °C, which allows it to be modeled directly above the individual. The cost is much higher than that at high temperature.

Polypropylene is a high temperature thermoplastic, it is considered to be the lightest plastic with excellent mechanical characteristics. is a semi-crystalline polymer characterized by a high tensile strength, low density, good thermal resistance and abrasion resistance. The cost is relatively low, but can cause allergies and sweating if in contact with the individual. It can show different tacticity, isotactic, atactic and syndiotactic. the most interesting product from the commercial point of view is the isotactic one, as it is more crystalline, with consequent greater mechanical strength and toughness.

Table C.2: Main properties of thermoplastic materials

Materials	ABS	PVC	PP	PE
Density [kg / m^3]	1040-1180	1400	920-940	926-960
Friction coefficient	0.5	0.4	0.1-0.3	0.29
Tensile strength [MPa]	32-45	40-55	25-40	15-40
Tensile modulus of elasticity (Young) [GPa]	1.7-2.6	1.8-2.6	0.7-1.5	0.5-1.2
stretching to break [%]‘	20-100	40-100	150-300	600-800

The thermostable materials are classified as rigid (short chains with many connections) and flexible (long chains with many connections). The strong molecules are permanently connected after irreversible molding through heating. They withstand high temperatures and have good dimensional stability. They are not very resistant to impact, but very complex and different geometries can be generated.

Elastomers have a high elongation power and a high coefficient of friction, and are used as fillers or sealants. Among the most important we remember:

- Rubber
- Silicones
- Neopreno

Silicones (or polysiloxanes) are inorganic polymers based on a silicon-oxygen chain and organic functional groups (R) bound to silicon atoms. they are excellent when used as impact crackers, they have good adherence to the balls and are easily washable. High costs, cause sweating and allergies.

Neoprene refers to a family of synthetic rubbers based on polychloroprene (polymeric form of chloroprene). The main characteristics are elasticity, resistance to shearing and crushing, resistance to atmospheric aging and heat, and it also appears to be inert towards many chemical agents, oils and solvents, is produced in various thicknesses and is easily washable. Widely used for protective coatings and garments for its good transpiration thus avoiding the problem of sweating.

C.1.3 Composite materials

Composite material is a heterogeneous material, ie it is a material consisting of two or more phases with different physical properties, whose properties are better than those of the phases that constitute it. The different phases in the composite consist of different materials, as in the case of carbon fiber and epoxy resin composites.

Carbon fiber is a material having a very thin thread-like structure, made of carbon, generally used in the production of a great variety of composite materials, which are so called because they are made up of two or more materials. In particular, the carbon fiber consists of carbon fiber and a so-called matrix, generally of resin, plastic or a metal whose function is to keep the resistant fibers in "laying", so that they maintain the correct orientation in absorbing the efforts to protect the fibers and also to maintain the shape of the composite product. Carbon fibers have a high chemical inertness compared to many aqueous solutions, they undergo deterioration if they come into contact with metals and metal oxides at temperatures higher than 1000 K. The mechanical properties are excellent, very similar to steel, but with a lower density, about 1750 kg / m^3 which allows lighter objects to be obtained. The mechanical strength of the different types of yarn varies between 2-7 GPa. The production cost is higher than steel.

Fiberglass reinforced plastic is a very strong and light material, with dimyl properties to carbon fiber, although not so exceptional. However the production cost is considerably reduced. Glass fibers are widely used in the production of structural composites in the aerospace, nautical and automotive fields, associated with different matrices, for example polyamide or epoxy, but still synthetic resins. They are not generally used in the production of composites with metallic or ceramic matrices.

Table C.3: Main properties of composite materials

Materials	Carbon fiber	Fiberglass
Density [kg / m^3]	1700-2100	2500-2800
Tensile strength [MPa]	3100-4500	2000-5000
Tensile modulus of elasticity (Young) [GPa]	220-800	70-80

Appendix D

Programming Codes

D.1 Function: Arm center of gravity calculation and pair due to gravity

```
%Arm center of gravity calculation and pair due to gravity
function [Mdtg, theta, Ixx, Iyy, Izz]= muscleFM_v2(body_mass, body_size,
        g, N, theta_min, theta_max, dtheta, ddtheta)
%% definizione grandezze
    m_up = 0.028*body_mass; %kg
    m_fa = 0.016*body_mass; %kg
    m_ha = 0.006*body_mass+0.5; %kg
    m = m_up + m_fa + m_ha; %kg

    l_up = 0.186*body_size; %m
    l_fa = 0.146*body_size; %m
    l_ha = 0.108*body_size; %m

    %calcolo centri di massa rispetto giunto spalla
    cm_up = l_up*47.16/100; %m
    cm_fa = l_fa*40.98/100 + l_up; %m
    cm_ha = l_ha*32.60/100 + l_up + l_fa; %m

    %centro massa globale (braccio esteso)
    b = (m_up*l_up + m_fa*l_fa + m_ha*l_ha)/(m_up + m_fa + m_ha); %m

    %momenti di inerzia
    Ixx_ua=(-250.7+1.56*body_mass+1.512*body_size*100)/10000; %kg*m^2
    Iyy_ua=(-232+1.525*body_mass+1.343*body_size*100)/10000; %kg*m^2
    Izz_ua=(-16.9+0.662*body_mass+0.0435*body_size*100)/10000; %kg*m^2

    Ixx_fa=(-64+0.95*body_mass+0.34*body_size*100)/10000; %kg*m^2
    Iyy_fa=(-67.9+0.855*body_mass+0.376*body_size*100)/10000; %kg*m^2
    Izz_fa=(5.66+0.306*body_mass-0.088*body_size*100)/10000; %kg*m^2

    Ixx_ha=(-19.5+0.17*body_mass+0.116*body_size*100)/10000; %kg*m^2
    Iyy_ha=(-13.68+0.088*body_mass+0.092*body_size*100)/10000; %kg*m^2
    Izz_ha=(-6.26+0.0762*body_mass+0.0347*body_size*100)/10000; %kg*m^2

    %respect frontal plane
```

```
    Ixx=Ixx_ua+Ixx_fa+Ixx_ha;
37  %respect saggital plane
    Iyy=Iyy_ua+Iyy_fa+Iyy_ha;
39  %respect horizontal plane
    Izz=Izz_ua+Izz_fa+Izz_ha;
41
    theta=linspace(theta_min, theta_max, N);
43  Mdtg = b*m*g*sin(theta*pi/180)+Iyy*ddtheta;
end
```

D.2 Function: Moment arm calculation

```
%Funzione per il calcolo del braccio
2 function [r, b]= d_arm_v5(a, c_I, rsp, alpha, beta, gamma, theta)
    for i=1:length(theta)
4       for j=1:length(c_I)
        a_I(j,i) = sqrt(a.^2+rsp.^2-2.*a*rsp.*cos((90+gamma(i)).*pi/180));
6       beta_I(j,i)= asin(rsp./a_I(j,i).*sin((90+gamma(i)).*pi/180)).*180./pi;
        b(j,i) = sqrt(a_I(j,i).^2+c_I(j).^2
8       +2.*a_I(j,i).*c_I(j).*cos((theta(i)+beta(j)+beta_I(j,i)-alpha).*pi./180));
        %Semi-perimeters
10      S(j,i) = (a_I(j,i) + c_I(j) + b(j,i))./2;
        A(j,i)=sqrt(S(j,i).*((S(j,i)-a_I(j,i)).*(S(j,i)-c_I(j)).*(S(j,i)-b(j,i))));
12      %Moment Arm calculation
        r(j,i)=(2./b(j,i)).*A(j,i);
14      end
    end
16 end
```

D.3 Shoulder Rythm and MdtG peak values

```
clear all
close all
clc

g = 9.81; %m/s^2
N=200;

body_mass=80; %Kg
body_size=1.8; %m

m_up = 0.028*body_mass; %kg
m_fa = 0.016*body_mass; %kg
m_ha = 0.006*body_mass; %kg
m = m_up + m_fa + m_ha; %kg

l_up = 0.186*body_size; %m
l_fa = 0.146*body_size; %m
l_ha = 0.108*body_size; %m

%calcolo centri di massa rispetto giunto spalla
cm_up = l_up*47.16/100; %m
cm_fa = l_fa*40.98/100 + l_up; %m
cm_ha = l_ha*32.60/100 + l_up + l_fa; %m

%centro massa globale (braccio esteso)
b = (m_up*l_up + m_fa*l_fa + m_ha*l_ha)/(m_up + m_fa + m_ha); %m

theta1 = 0:1:130;
M1 = b*m*g*sin(theta1*pi/180);

theta2 = 0:1:130;
for i=1:length(theta2)
    x2_cm(i)=l_fa*cos(theta2(i)*pi/180);
    y2_cm(i)=l_fa*sin(theta2(i)*pi/180);
    x3_cm(i)=(l_fa+l_ha)*cos(theta2(i)*pi/180);
    y3_cm(i)=(l_fa+l_ha)*sin(theta2(i)*pi/180);

    x_cm(i)= (m_up*l_up + m_fa*x2_cm(i) + m_ha*x3_cm(i))
/(m_up + m_fa + m_ha);
    y_cm(i)= (0 + m_fa*y2_cm(i) + m_ha*y3_cm(i))
/(m_up + m_fa + m_ha);
    CM(i)=(x_cm(i)^2+y_cm(i)^2)^(1/2);
end

for i=1:length(CM)
    M2(i)= CM(i)*m*g*sin(pi/2);
end

```

```
figure('name','Arm Torque characteristics','IntegerHandle','off')
subplot(3,1,1)
title('\fontsize{16}Max Moment due to gravity[Nm]')
plot(theta1,M1,'-','linewidth',2),grid on, hold on
xlabel('\fontsize{14} \theta_1[degree]')
ylabel('\fontsize{14}MdtG_M_a_x[Nm]')

subplot(3,1,2)
title('\fontsize{16}Center of Mass (\theta_2 variable)')
plot(theta2,CM,'-','linewidth',2),grid on, hold on
xlabel('\fontsize{14} \theta_2[degree]')
ylabel('\fontsize{14}CoM[m]')

subplot(3,1,3)
title('\fontsize{16}Center of Mass (\theta_2 variable)')
plot(CM,M2,'-','linewidth',2),grid on, hold on
xlabel('\fontsize{14}CoM[m]')
ylabel('\fontsize{14}MdtG_p_e_a_k_ _v_a_l_u_e_s[Nm]')

%% Shoulder Rythm
% clear all
%Definizione dati Scapulahumeral rhythm
lc = 0.14999; %m
ls = 0.0668; %m
lb = 0.792; %m
h = 1.73; %m
href = 1.800; %m

%Variazioni theta
theta_1 = 0;
theta_2 = 30;
theta_3 = 80;
theta_4 = 140;
theta_5 = 180;

%Variazioni ni
d_ni_1 = 0;
d_ni_2 = 26;
d_ni_3 = 65;
d_ni_4 = 90;
d_ni_5 = 121;

%Variazioni beta
d_beta_1 = 0;
d_beta_2 = 0;
d_beta_3 = 0;
d_beta_4 = 35;
d_beta_5 = 35;

%Variazioni alpha
```

```
d_alpha_1 = 0;
d_alpha_2 = 4;
d_alpha_3 = 15;
d_alpha_4 = 15;
d_alpha_5 = 24;

%Angoli iniziali
alpha_0 = 99;
beta_0 = 143;
ni_0 = 118;

%Vettori angoli
theta1 = linspace(theta_1, theta_2, N/4);
theta2 = linspace(theta_2, theta_3, N/4);
theta3 = linspace(theta_3, theta_4, N/4);
theta4 = linspace(theta_4, theta_5, N/4);

ni1 = linspace(d_ni_1, d_ni_2, N/4) + ni_0;
ni2 = linspace(d_ni_2, d_ni_3, N/4) + ni_0;
ni3 = linspace(d_ni_3, d_ni_4, N/4) + ni_0;
ni4 = linspace(d_ni_4, d_ni_5, N/4) + ni_0;

beta1 = linspace(d_beta_1, d_beta_2, N/4) + beta_0;
beta2 = linspace(d_beta_2, d_beta_3, N/4) + beta_0;
beta3 = linspace(d_beta_3, d_beta_4, N/4) + beta_0;
beta4 = linspace(d_beta_4, d_beta_5, N/4) + beta_0;

alpha1 = linspace(d_alpha_1, d_alpha_2, N/4) + alpha_0;
alpha2 = linspace(d_alpha_2, d_alpha_3, N/4) + alpha_0;
alpha3 = linspace(d_alpha_3, d_alpha_4, N/4) + alpha_0;
alpha4 = linspace(d_alpha_4, d_alpha_5, N/4) + alpha_0;

theta1 = [theta1 theta2 theta3 theta4]*pi/180;
ni = [ni1 ni2 ni3 ni4]*pi/180;
beta = [beta1 beta2 beta3 beta4]*pi/180;
alpha = [alpha1 alpha2 alpha3 alpha4]*pi/180;

lgs = sqrt(ls^2+lc^2-2*ls*lc*cos(beta));

[Mlgs,Plgs]=max(lgs);

theta_1=(theta1-90).*pi./180;

for i_cgh=1:length(theta1)
    x_CGH(i_cgh) = ((+lc*cos(alpha(i_cgh)-90*pi/180)+ls*sin(beta(i_cgh)
+ alpha(i_cgh)-180*pi/180))*h/href);
    y_CGH(i_cgh) = ((+lc*sin(alpha(i_cgh)-90*pi/180)-ls*cos(beta(i_cgh)
+ alpha(i_cgh)-180*pi/180))*h/href);
end

```

```
for i_cgh=1:length(theta1)
    x_ARM(i_cgh) = ((+lc*cos(alpha(i_cgh)-90*pi/180)+ls*sin(beta(i_cgh)
        + alpha(i_cgh)-180*pi/180)+lb*sin(beta(i_cgh)
        + alpha(i_cgh) + ni(i_cgh-360*pi/180))*h/href);
    y_ARM(i_cgh) = ((+lc*sin(alpha(i_cgh)-90*pi/180)-ls*cos(beta(i_cgh)
        + alpha(i_cgh)-180*pi/180)-lb*cos(beta(i_cgh)
        + alpha(i_cgh) + ni(i_cgh)-360*pi/180))*h/href);
    r_ARM(i_cgh) = sqrt(x_ARM(i_cgh)^2+y_ARM(i_cgh)^2);
end

figure('name','Arm Cartesian Space','IntegerHandle','off');
subplot(1,2,1)
plot(x_CGH,y_CGH,'-','linewidth',1.5);
grid on;
axis equal;
xlabel('x_C_G_H [m]');
ylabel('y_C_G_H [m]');
title('Shoulder Rythm');

subplot(1,2,2)
plot(x_ARM,y_ARM,'-','linewidth',1.5);
grid on;
axis equal;
xlabel('x_A_R_M [m]');
ylabel('y_A_R_M [m]');
title('Flexion/Extension trajectory');

figure(2)
plot(theta1.*180./pi,r_ARM,'-','linewidth',1.5);
grid on;
axis equal;
xlabel('\theta [degree]');
ylabel('Arm [m]');
title('Distance from CGH center');
```

D.4 Denavit-Hartenberg Convention

```
close all
clear all
clc

%Denavit−Hartenberg parameters link 1
alpha1 = pi/2; %rad
a1 = 12; %cm
d1 = 0; %cm
theta1 = 0 + pi/2;%rad
sigma1 = 0;
qlim1= [0 130]∗pi/180; %range q1

%Denavit−Hartenberg parameters link 2
alpha2 = −pi/2; %rad
a2 = 0; %cm
d2 = 0; %cm
theta2 = 0 + pi/2; %rad
sigma2 = 0;
qlim2= [−155 −60]∗pi/180; %range q2

%Denavit−Hartenberg parameters link 3
alpha3 = 0; %rad
a3 = 0; %cm
d3 = 15; %cm
theta3 = 0; %rad
sigma3 = 0;
qlim3= [0 180]∗pi/180; %range q3

%Denavit−Hartenberg parameters link 5
alpha4 = 0; %rad
a4 = 0; %cm
d4 = 0; %cm
theta4 = 0; %rad
sigma4 = 1;
qlim4= [0 15]; %range q5

% th d a alpha
L(1) = Link([theta1 d1 a1 alpha1 sigma1]);
L(2) = Link([theta2 d2 a2 alpha2 sigma2]);
L(3) = Link([theta3 d3 a3 alpha3 sigma3]);
L(4) = Link([theta4 d4 a4 alpha4 sigma4]);

L(1).qlim = qlim1;
L(2).qlim = qlim2;
L(3).qlim = qlim3;
L(4).qlim = qlim4;

PassiveExo = SerialLink(L);
```

```
PassiveExo.name = 'Passive Exoskeleton';

figure(1)
PassiveExo.teach([0 qlim2(2) 0 0]) %teach
PassiveExo.fkine([0 qlim2(2) 0 0]); %forward kinematics
PassiveExo.plot([0 qlim2(2) 0 0]); %initial plot
xlabel('X [cm]');
ylabel('Y [cm]');
zlabel('Z [cm]');
title('Workspace of Passive Exo');
hold on;
N=50;
for i= 1:N+1
    for j= 1:N+1
    TR = PassiveExo.fkine
        ([qlim1(2)*(i-1)/N pi*(95/180)*(j-1)/N+qlim2(1) 0 qlim4(1)]);
    SURF(i,j,:) = TR.t;
    end
end

CO(:,:,1) = zeros(N+1); % red
CO(:,:,2) = ones(N+1).*linspace(0.5,0.6,N+1); % green
CO(:,:,3) = ones(N+1).*linspace(0,1,N+1); % blue
surf(SURF(:,:,1),SURF(:,:,2),SURF(:,:,3),CO);

for i= 1:N+1
    for j= 1:N+1
    TR = PassiveExo.fkine
        ([qlim1(2)*(i-1)/N pi*(95/180)*(j-1)/N+qlim2(1) 0 qlim4(2)]);
    SURF(i,j,:) = TR.t;
    end
end

CO(:,:,1) = zeros(N+1); % red
CO(:,:,2) = ones(N+1).*linspace(0.5,0.6,N+1); % green
CO(:,:,3) = ones(N+1).*linspace(0,1,N+1); % blue
surf(SURF(:,:,1),SURF(:,:,2),SURF(:,:,3),CO);
```

D.5 Spatial CAM Modeling

```
clear all
close all
clc

%Body Data Age 30
g = 9.81; %m/s^2
body_mass=70; %Kg
body_size=1.72; %m
dtheta=200*pi/180; %rad/s
ddtheta=dtheta/0.2; %rad/s^2

N=120; %punti approx
theta_max=120; %angolo flessione
alpha_max=35; %angolo curvatura camma

ta=(theta_max*pi/180)/dtheta; %tempo avanzamento s

%Calcutation of Arm Moment
[Mdtg, theta, Ixx, Iyy, Izz]= muscleFM(body_mass, body_size,
        g, N, theta_max, dtheta, ddtheta); %[Nm]
Mdtg=Mdtg+3;

phi=atan(0.05)*180/pi; %coeff attrito dinamico acciai lubrificati
alpha=linspace(phi, alpha_max, N);
ns=1; %numero molle serie
np=4; %numero molle in parallelo
ks=18.01/ns; %rigidezza molle serie
kp=np*ks; %rigidezza molla N/mm
d_medio=0.10; %m

%geometria camma
[Ma,Pa]=max(alpha);
[ma,pa]=min(alpha);
dtheta_i=theta_max/N.*ones(1,N);
alpha_i=linspace(ma,Ma,N);
l_alzate=(d_medio.*(dtheta_i.*pi./180)./2)./(cos(alpha_i.*pi./180)).*1000.*32;
%legge delle alzate approx mm
[M_alzate,P_alzate]=max(l_alzate);
[m_alzate,p_alzate]=min(l_alzate);
l_alzate=l_alzate-m_alzate;

%Sagoma equivalente
x_se=theta.*pi./180.*(d_medio/2).*1000; %mm
y_se=l_alzate;
c_pol=polyfit(x_se,y_se,4);
[minx_se,mpx_se]=min(x_se);
[Maxx_se,Mx_se]=max(x_se);
x_sevett=linspace(minx_se,Maxx_se,100);
```

```
ev_pol=polyval(c_pol,x_sevett);

%legge alzate
x_la=theta.*pi./180; %radianti
y_la=l_alzate; %mm
c_la=polyfit(x_la,y_la,7); %coeff polinomio 7 grad
[h, P_h]=max(y_la);

%Alzata adimensionale
Y=y_la./h;
tau=alpha/Ma;

theta=theta.*pi./180; %rad
%vel. geometrica
for i=1:length(theta)
dy_g(i)=c_la(1).*7.*theta(i).^6-c_la(2).*6.*theta(i).^5
        +c_la(3).*5.*theta(i).^4+c_la(4).*4.*theta(i).^3
        +c_la(5).*theta(i).^2+c_la(6).*theta(i)+c_la(7);
end

%vel.
dy=dy_g.*dtheta;
%vel. adimensionale
YI=dy./(h/ta);

%accellerazione geometrica
for i=1:length(theta)
ddy_g(i)=c_la(1).*7.*6.*theta(i).^5-c_la(2).*6.*5.*theta(i).^4
        +c_la(3).*5.*4.*theta(i).^3+c_la(4).*4.*3.*theta(i).^2
        +c_la(5).*2.*theta(i)+c_la(6);
end

%accellerazione
ddy=ddy_g.*(dtheta^2);
%accellerazione adimensionale
YII=ddy./(h/(ta^2));

%Jerk adimensionale def. YIII=dYII/Dtau=dddy_g/dtheta*theta_MAX*ta^2/h
for i=1:length(theta)
YIII(i)=(c_la(1).*7.*6.*5.*theta(i).^4-c_la(2).*6.*5.*4.*theta(i).^3
        +c_la(3).*5.*4.*3.*theta(i).^2+c_la(4).*4.*3.*2.*theta(i)
        +c_la(5).*2).*(theta(end)*ta^2/h);
end

theta=theta.*180./pi; %grad

%dati molla LC 059F 03 (Catalogo lee)
Li=19.05; %lunghezza iniziale molla mm
Lf=10.01; %lunghezza finale molla mm
delta_Li=Li-Lf; %delta molla mm
```

```
delta_Lf=3.2; %delta finale richiesto mm
dL=linspace(delta_Li, delta_Lf, N); %dL molla mm
Fm=dL.*kp; %forza molla

frc=0.005; %coefficients of friction for lubricated linear ball bearings
%(between 0,0015 (heavy loads) and 0,005 (light loads))
F_friction_f=dL.*kp.*tan((alpha-phi)*pi/180)*frc;
F_friction_e=dL.*kp.*tan((alpha+phi)*pi/180)*frc;

f_camma_f=tan((alpha-phi)*pi/180); %curvatura camma flessione
Fu_f=dL.*kp.*f_camma_f-F_friction_f; %forza utile flessione N
M_f=Fu_f.*d_medio/2; %momento in flessione Nm

f_camma_e=tan((alpha+phi)*pi/180); %curvatura camma estensione
Fu_e=dL.*kp.*f_camma_e-F_friction_e; %forza utile estensione N
M_e=Fu_e.*d_medio/2; %momento in estensione Nm

S=dL.*kp.*cos((alpha+phi)*pi/180); %spinta massima in estensione N

%Pressioni herziane
b=11; %mm
Rr=16; %mm
E=220000; %N/mm
ro=((d_medio/2*1000).^2)./(cos((alpha+phi)*pi/180).^3.*ddy_g(end)); %mm
ph=sqrt(0.175.*((S.*E)./(b*Rr)).*(1+Rr./ro)); %MPa
r_min=((dy_g(end))/tan(alpha_max*pi/180)); %Rb camma minimo mm

M_ris=Mdtg-M_e; %momento risultante in estensione Nm

%% Plot
figure(1)
plot(theta,Mdtg, 'linewidth',1.5);
hold on;
grid on;
plot(theta,M_f, 'linewidth',1.5);
plot(theta,M_e, 'linewidth',1.5);
xlabel('\theta_1 degree');
ylabel('Torques [Nm]');
title('Troques vs. \theta_1','fontsize',12,'fontweight','bold');
legend('mdtg','elastic released torque', 'static torque compensation');
legend('Location','best');


figure(2)
subplot(4,1,1)
plot(tau,Y, 'k', 'linewidth',1);
xlim([tau(1) tau(end)]);
hold on;
grid on;
xlabel('\tau [-]');
```

```
ylabel('Y [-]');
title('Displacement diagram','fontsize',12,'fontweight','bold');
subplot(4,1,2)
plot(tau,YI, 'b', 'linewidth',1);
xlim([tau(1) tau(end)]);
hold on;
grid on;
xlabel('\tau [-]');
ylabel('YI [-]');
title('Dimensionless velocity','fontsize',12,'fontweight','bold');
subplot(4,1,3)
plot(tau,YII, 'r', 'linewidth',1);
xlim([tau(1) tau(end)]);
hold on;
grid on;
xlabel('\tau [-]');
ylabel('YII [-]');
title('Dimensionless acceleration','fontsize',12,'fontweight','bold');
subplot(4,1,4)
plot(tau,YIII, 'r', 'linewidth',1);
xlim([tau(1) tau(end)]);
hold on;
grid on;
xlabel('\tau [-]');
ylabel('YIII [-]');
title('Dimensionless Jerk','fontsize',12,'fontweight','bold');

figure(3)
plot(dL, Fm, 'linewidth',1.5);
hold on;
grid on;
xlabel('dL [mm]');
ylabel('Spring force [N]');
title('Spring force vs. deformation','fontsize',12,'fontweight','bold');

figure(4)
plot(theta, alpha, 'linewidth',1.5);
hold on;
grid on;
xlabel('\theta_1 degree');
ylabel('\theta degree');
title('Transmission angle \theta vs. advance angle \theta_1'
        ,'fontsize',12,'fontweight','bold');

figure(5)
plot(theta,M_ris,'linewidth',1.5);
hold on
grid on
xlabel('\theta_1 degree');
ylabel('M [Nm]');
```

```
199 title('Result moment vs. Angle');

201 %plot sagoma equivalente
    figure(6)
203 plot(x_se,l_alzate,'linewidth',1.5);
    hold on
205 grid on
    plot(x_sevett,ev_pol,'linewidth',1.5);
207 xlabel('Circumference of cam [mm]');
    ylabel('Follower displacement [mm]');
209 title('Development of cylindrer');
    legend('law of motion', 'approximation');
211 legend('Location','best');

213 figure(7)
    plot(theta,ro,'linewidth',1.5);
215 hold on
    grid on
217 xlabel('\theta_1 degree');
    ylabel('\rho [mm]');
219 title('Radius of curvature');

221 figure(8)
    plot(theta,ph,'linewidth',1.5);
223 hold on
    grid on
225 xlabel('\theta_1 degree');
    ylabel('Ph [MPa]');
227 title('Hertzian contact stress');

229 %% Wheel friction moment
    dmw=(D+d)/2000; %wheel average diameter m
231 fwf=0.0035; %friction coefficient
    Mwf=fwf.*Fm*dmw/2;
```

D.6 Supporting Geometry Modeling

```
clear all
close all
clc

%Dati INPUT
L_muscle=400; %mm
p=[100, 200, 300, 400, 500, 600]; %kPa
ck=[0 0 2 2.5 1 1]; %coeff. contrazione
%definisce forza massima e minima ottenuta dalla contrazione utile
N=500; %punti approx
np=3; %pressione di lavoro bar (scegliere 1-6 bar)
nk=3; %contrazione massima ammessa in funzione di l
%(scegliere 1, 2, 3)

%Body Data Age 30
g = 9.81; %m/s^2
body_mass=70; %Kg
body_size=1.72; %m
dtheta=200*pi/180; %rad/s
ddtheta=dtheta/0.2; %rad/s^2
theta_max=120; %angolo flessione

%Calcutation of Arm Moment
[Mdtg, theta, Ixx, Iyy, Izz]=muscleFM(body_mass, body_size,
        g, N, theta_max, dtheta, ddtheta); %[Nm]
Mdtg=Mdtg;

%Torque's Arm calculation - with d Variation
%Geometric Data
rsp=0.007; %support joint m
rsj=0.01; %shoulder joint r m
l0=0.10; %m
l=[0.25, 0.30, 0.35]; %m
alpha=50; %grad
l0_I=sqrt(rsp^2+l0^2); %m
beta_0=asin(rsp/l0_I)*180/pi; %grad


%calcolo beta in funzione di l e rsp
for i=1:length(l)
    beta(i)=(acos(l(i)/(sqrt(l(i)^2+rsp^2))))*180/pi; %grad
end

%Calcolo d e L
[d, dp, L]= d_arm_v2(l0, l, rsj, alpha, beta, theta); %[m]
ang_avv=linspace(alpha,0, dp);
L_r=ang_avv.*rsj.*pi./180;

```

```
%polinomio d
d_prova=(d(1,dp:end)-0.002).*1000;
theta_prova=linspace(80,120,length(d_prova));
c_pol=polyfit(theta_prova,d_prova,2);
ev_pol=polyval(c_pol,theta_prova);

%Correzione vettore L per angolo avvolgimento (shoulder joint)
for i=1:length(l)
    c_vett=zeros(1,(length(L(i,:))-length(L_r)));
    [max_L(i), p_L(i)]=max(L(i,:));
    L_ri(i,:)=L_r+max_L(i);
    L_rm(i,:)=[L_ri(i,:) c_vett];
end

for i=1:length(l)
    for j=1:dp
    L(i,j)=L_rm(i,j);
    end
end

L=L*1000; %mm

pm=ones(length(p),N);
%Matrice Pressioni
pm(1,:)=p(1)*pm(1,:);
pm(2,:)=p(2)*pm(2,:);
pm(3,:)=p(3)*pm(3,:);
pm(4,:)=p(4)*pm(4,:);
pm(5,:)=p(5)*pm(5,:);
pm(6,:)=p(6)*pm(6,:);

%coeff. caratteristica muscolo
a1=0.11210;
a2=263.700;
a3=-0.35150;
a4=-0.08619;
a5=2.62400;
a6=-245.60;

% Contrazioni Originali
ko(1,:)=linspace(0, 5.96, N);
ko(2,:)=linspace(0, 16, N);
ko(3,:)=linspace(0, 20.96, N);
ko(4,:)=linspace(0, 23.33, N);
ko(5,:)=linspace(0, 24.75, N);
ko(6,:)=linspace(0, 25.70, N);

km=zeros(length(p),N);
% Contrazioni plot surf
km(1,:)=linspace(0, 27, N);
```

```
km(2,:)=linspace(0, 27, N);
km(3,:)=linspace(0, 27, N);
km(4,:)=linspace(0, 27, N);
km(5,:)=linspace(0, 27, N);
km(6,:)=linspace(0, 27, N);

%calcolo variazione lunghezza cavo per contrazione massima utile del muscolo
for i=1:length(l)
    [L_max(i),pl_max(i)]=max(L(i,:));
    [L_min(i),pl_min(i)]=min(L(i,:));
    dL_max(i)=L_max(i)-L_min(i);
    k_max(i)=dL_max(i)*100/L_muscle;
end
k=zeros(length(p),N);
%Contrazioni utili (range utile di lavoro del muscolo)
k(1,:)=linspace(ko(1,end)-k_max(nk)-ck(1), ko(1,end)-ck(1), N);
k(2,:)=linspace(ko(2,end)-k_max(nk)-ck(2), ko(2,end)-ck(2), N);
k(3,:)=linspace(ko(3,end)-k_max(nk)-ck(3), ko(3,end)-ck(3), N);
k(4,:)=linspace(ko(4,end)-k_max(nk)-ck(4), ko(4,end)-ck(4), N);
k(5,:)=linspace(ko(5,end)-k_max(nk)-ck(5), ko(5,end)-ck(5), N);
k(6,:)=linspace(ko(6,end)-k_max(nk)-ck(6), ko(6,end)-ck(6), N);


for i=1:length(p)
    for j=1:N
        Fo(i,j) = (a1*p(i)+a2)*exp(a3*ko(i,j))+(a4*p(i)*ko(i,j))+a5*p(i)+a6;
        Fm(i,j) = (a1*p(i)+a2)*exp(a3*km(i,j))+(a4*p(i)*km(i,j))+a5*p(i)+a6;
        if Fo(i,j)<0
            Fo(i,j)=0;
        end
    end

    figure(1)
    plot(ko(i,:),Fo(i,:),'linewidth',1.5);
    hold on
    grid on
    xlabel('Contraction [%]');
    ylabel('Force [N]');
    t=['Force vs. Catalogue contraction -
        Active length = ',num2str(L_muscle),'[mm]'];
    title(t,'fontsize',12,'fontweight','bold');
    legend_parameters=['\fontsize{8}p = ',num2str(p(i)),'\fontsize{8}kPa'];
    lgnd(i,1:length(legend_parameters))=legend_parameters;
    legend(lgnd);
    legend('Location','best');
end
clear legend_parameters, clear lgnd, clear t;

dL_muscle=L_muscle*ko/100;
for i=1:length(p)
```

```
    Fi(i,:)=fliplr(Fo(i,:));
150 figure(2)
    plot(dL_muscle(i,:),Fo(i,:),'linewidth',1.5);
152 hold on
    grid on
154 xlabel('\DeltaL [mm]');
    ylabel('Force [N]');
156 t=['Force vs. Length variation −
          Active length = ',num2str(L_muscle)' [mm]'];
158 title(t,'fontsize',12,'fontweight','bold');
    legend_parameters=['\fontsize{8}p = ',num2str(p(i))' \fontsize{8}kPa'];
160 lgnd(i,1:length(legend_parameters))=legend_parameters;
    legend(lgnd);
162 legend('Location','best');
    end
164 clear legend_parameters, clear lgnd, clear t;

166 %Surf plot Data
    figure(3)
168 surf(km,pm,Fm);
    grid on;
170 title('3D Plot (Contraction, Pressure, Force)');
    xlabel('Contraction [%]');
172 ylabel('Pressure [kPa]');
    zlabel('Force [N]');
174 colormap('hsv');
    colorbar;
176
    %variazione utile lunghezza muscolo
178 dL_muscle_useful=L_muscle*k/100;
    lg=1; %contatore per leggenda
180 for i=1:length(p)
        if (ko(i,end)−k_max(nk))>0
182     for j=1:N
            F(i,j) = (a1*p(i)+a2)*exp(a3*k(i,j))+(a4*p(i)*k(i,j))+a5*p(i)+a6;
184         if F(i,j)<0
                F(i,j)=0;
186         end
        end
188
        figure(4)
190     plot(k(i,:),F(i,:),'linewidth',1.5);
        hold on
192     grid on
        xlabel('Contraction [%]');
194     ylabel('Force [N]');
        t_uc=['Force vs. Useful contraction −
196           Active length = ',num2str(L_muscle)' [mm]'];
        title(t_uc,'fontsize',12,'fontweight','bold');
198     legend_parameters=['\fontsize{8}p = ',num2str(p(i))' \fontsize{8}kPa'];
```

```
        lgnd(lg,1:length(legend_parameters))=legend_parameters;
200     legend(lgnd);
        legend('Location','best');
202
        [dLm_MAX, dLm_MP]=max(dL_muscle_useful(i,:));
204     [dLm_min, dLm_mp]=min(dL_muscle_useful(i,:));
        dLm=dLm_MAX-dLm_min;
206
        figure(5)
208     plot(dL_muscle_useful(i,:),F(i,:),'linewidth',1.5);
        hold on
210     grid on
        xlabel('\DeltaL [mm]');
212     ylabel('Force [N]');
        t_ul=['Force vs. Useful length variation -
214           Active length = ',num2str(L_muscle) '[mm]'];
        title(t_ul,'fontsize',12,'fontweight','bold');
216     legend(lgnd);
        legend('Location','best');
218     lg=lg+1;
        fprintf('Length variation
220           %g mm for p = %g kPa and l=%g\n',dLm, p(i), l(nk));
    else
222 end
end
224 clear legend_parameters, clear lgnd, clear t;

226 d=d*1000; %mm
for i=1:length(l)
228     figure(6)
    plot(theta,d(i,:),'linewidth',1.5);
230     hold on
    grid on
232     xlabel('\theta degree');
    ylabel('d [mm]');
234     title('d vs. Angle');
    legend_parameters=['\fontsize{8}l = ',num2str(l(i)) '\fontsize{8}m'];
236     lgnd(i,1:length(legend_parameters))=legend_parameters;
    legend(lgnd);
238     legend('Location','best');
end
240 clear legend_parameters, clear lgnd, clear t;

242 for i=1:length(l)
    [dL_MAX, dL_MP]=max(L(i,:));
244     [dL_min, dL_mp]=min(L(i,:));
    dL=dL_MAX-dL_min;
246     figure(7)
    plot(theta,L(i,:),'linewidth',1.5);
248     hold on
```

```
    grid on
    xlabel('\theta degree');
    ylabel('L(\theta,d(\theta)) [mm]');
    title('L vs. Angle');
    legend_parameters=['\fontsize{8}l = ',num2str(l(i)),'\fontsize{8}m'];
    lgnd(i,1:length(legend_parameters))=legend_parameters;
    legend(lgnd);
    legend('Location','best');
    fprintf('Cable length variation %g mm for l = %g mm\n',dL,l(i));
end
clear legend_parameters, clear lgnd, clear t;

d=d/1000; %m
figure(8)
plot(theta,Mdtg,'k--','linewidth',1.5);
hold on
grid on
Mgc=d(nk,:).*F(np,:);
plot(theta,Mgc,'linewidth',1.5);
xlabel('\theta degree');
ylabel('M [Nm]');
t=['Torques vs. Angle (p= ',num2str(p(np)),'[kPa], l= ',num2str(l(nk)),'[m])'];
title(t,'fontsize',12,'fontweight','bold');
legend('\fontsize{8}M. due to Gravity','\fontsize{8}M. gravity compensation');
legend('Location','best');
DM=Mdtg-Mgc;
clear legend_parameters, clear lgnd, clear t;

figure(9)
plot(theta,DM,'linewidth',1.5);
hold on
grid on
xlabel('\theta degree');
ylabel('M [Nm]');
t=['Result torque vs. Angle (p= ',num2str(p(np)),'[kPa], l= ',num2str(l(nk)),'[m])'];
title(t,'fontsize',12,'fontweight','bold');
```

D.7 Pulley-Cable Modeling

```
clear all
close all
clc

%Dati INPUT
N=200; %punti approx
np=1; %pressione di lavoro (scegliere 1−3 (rispettivamente 2,4,6 bar))
nl=1; %contrazione massima ammessa in funzione di l (scegliere 1, 2, 3)

%Body Data Age 30
g = 9.81; %m/s^2
body_mass=70; %Kg
body_size=1.72; %m
dtheta=200*pi/180; %rad/s
ddtheta=dtheta/0.2; %rad/s^2
theta_min=90; %angolo flessione
theta_max=125; %angolo flessione

%Arm Moment Calcutation
[Mdtg, theta, Ixx, Iyy, Izz]=muscleFM_v2(body_mass, body_size,
        g, N, theta_min, theta_max, dtheta, ddtheta); %[Nm]

%Torque's Arm calculation - with d Variation
%Geometric Data
rsp=0.007; %support joint [m]
rsj=0.015; %shoulder joint r [m]
ras=0.05; %arm support radius [m]
a=0.15; %[m]
c=[0.20, 0.25, 0.30]; %[m]
alpha=80; %degree

c_I=sqrt(c.^2+ras^2); %[mm]
beta=asin(ras./c_I).*180/pi; %degree
gamma=linspace(0,90,N); %degree

%Calcolo r e b
[r, b]= d_arm_v5(a, c_I, rsp, alpha, beta, gamma, theta); %[m]

r=r*1000; %mm
for i=1:length(c)
    figure(1)
    plot(theta,r(i,:),'linewidth',1.5);
    hold on
    grid on
    xlabel('\theta_1 degree');
    ylabel('r [mm]');
    title('r vs. Angle');
    legend_parameters=['\fontsize{8}c = ',num2str(c(i)) '\fontsize{8}m'];
```

```
    lgnd(i,1:length(legend_parameters))=legend_parameters;
50  legend(lgnd);
    legend('Location','best');
52  end
    clear legend_parameters, clear lgnd, clear t;
54
    b=b.*1000; %mm
56  for i=1:length(c)
        [b_MAX, b_MP]=max(b(i,:));
58      [b_min, b_mp]=min(b(i,:));
        db=(rsp*1000*gamma(end)*pi/180+b_MAX)-b_min;
60      figure(2)
        plot(theta,b(i,:),'linewidth',1.5);
62      hold on
        grid on
64      xlabel('\theta_1 degree');
        ylabel('b [mm]');
66      title('b vs. Angle');
        legend_parameters=['\fontsize{8}c = ',num2str(c(i)) '\fontsize{8}m'];
68      lgnd(i,1:length(legend_parameters))=legend_parameters;
        legend(lgnd);
70      legend('Location','best');
        fprintf('Cable length variation %g mm for c = %g m\n',db, c(i));
72  end
    clear legend_parameters, clear lgnd, clear t;
74


76  %% Shadow Rob muscle
    %Percentage Contraction of Active Length for 20mm Air Muscle
78  %Pressure 0, 2, 4, 6 bar
    F0 = flip([5 10 15 20 25]).*9.81; %[N]
80  C2 = flip([29 23 17 12 10])./100; %[%]
    C4 = flip([33 29 25 23 22])./100; %[%]
82  C6 = flip([34 31 29 26 24])./100; %[%]

84  %Pressures
    p=[2 4 6].*100; %kPa
86
    %contractions
88  k0_sr=zeros(length(p),length(F0));
    k0_sr(1,:)=C2*100;
90  k0_sr(2,:)=C4*100;
    k0_sr(3,:)=C6*100;
92
    for i=1:length(p)
94      %determinazione polinomio
        c_sr(i,:)=polyfit(k0_sr(i,:),F0,3);
96      k_sr(i,:)=linspace(k0_sr(i,1),k0_sr(i,end),N);
        F_sr(i,:)=polyval(c_sr(i,:),k_sr(i,:));
98  end
```

```
M_gen_sr=F_sr(np,:).*r(nl,:)/1000; %[Nm]

%% Risultanti 2
figure(3)
plot(theta,M_gen_sr,'linewidth',1.5);
hold on
grid on
plot(theta,Mdtg,'k--','linewidth',1.5);
xlabel('\theta_1 degree');
ylabel('M [Nm]');
t=['Torques vs. Angle (useful radius
p= ',num2str(p(np))' [kPa],
c= ',num2str(c(nl))' [m])'];
title(t,'fontsize',12,'fontweight','bold');
legend('Generated torque', 'Moment due to gravity');
legend('Location','best');

%calcolo momento risultante in funzione della pressione e del raggio scelto
M_res_sr=Mdtg-M_gen_sr;
figure(4)
plot(theta,M_res_sr,'linewidth',1.5);
hold on
grid on
xlabel('\theta_1 degree');
ylabel('M [Nm]');
t=['Result Torques vs. Angle
(p= ',num2str(p(np))' [kPa],
useful radius for c= ',num2str(c(nl))' [m])'];
title(t,'fontsize',12,'fontweight','bold');

rate=M_gen_sr./Mdtg.*100;
figure(5)
plot(theta,rate,'linewidth',1.5);
hold on
grid on
xlabel('\theta_1 degree');
ylabel('Rate coefficient [%]');
t=['Rate coefficient
(p= ',num2str(p(np))' [kPa],
useful radius for c= ',num2str(c(nl))' [m])'];
title(t,'fontsize',12,'fontweight','bold');
```

D.8 Shadow Robot Muscle - Static Characteristic

```
%Data Sheet 20mm BPA muscle
clear all
close all
clc

%Dati INPUT
N=200; %punti approx
rp=3; %raggio identificazione geometria (scegliere da 1 a 6);
c=200; %[mm] distanza cavo da giunto spalla
ras=50; %arm support radius [mm]
pr=50; % percentuale recupero coppia [%]

%Body Data Age 30
g = 9.81; %m/s^2
body_mass=70; %Kg
body_size=1.72; %m
dtheta=200*pi/180; %rad/s
ddtheta=dtheta/0.2; %rad/s^2
theta_min=90; %angolo flessione
theta_max=130; %angolo flessione

%Calcutation of Arm Moment
[Mdtg, theta, Ixx, Iyy, Izz]= muscleFM_v2(body_mass, body_size,
        g, N, theta_min, theta_max, dtheta, ddtheta); %[Nm]
M_pr=Mdtg.*pr./100;

%Percentage Contraction of Active Length for 20mm Air Muscle
%Pressure 0, 2, 4, 6 bar

F0 = flip([5 10 15 20 25]).*9.81; %[N]
C2 = flip([29 23 17 12 10])./100; %[%]
C4 = flip([33 29 25 23 22])./100; %[%]
C6 = flip([34 31 29 26 24])./100; %[%]

%Gometric Data
D_muscle = 20; %[mm]
L_muscle = 210; %[m] active length
W = 40; %[g] weight approx.
n=2.5; %number of turns

%Pressures
p=[2 4 6]; %bar

%contractions
k0=zeros(length(p),length(F0));
k0(1,:)=C2*100;
```

```
k0(2,:)=C4*100;
k0(3,:)=C6*100;

%contractions variations
dL=zeros(length(p),N);
dL(1,:)=L_muscle.*linspace(C2(1),C2(end),N);
dL(2,:)=L_muscle.*linspace(C4(1),C4(end),N);
dL(3,:)=L_muscle.*linspace(C6(1),C6(end),N);

%Length variation
L=zeros(length(p),N);
L(1,:)=linspace(L_muscle,L_muscle*C2(1),N);
L(2,:)=linspace(L_muscle,L_muscle*C4(1),N);
L(3,:)=linspace(L_muscle,L_muscle*C6(1),N);

% for i=1:length(p)
% for j=1:length(Fo)
% b_cm(i,j) = sqrt(3*L(i,j)^2-(Fo(i)*4*pi*n^2)/(p(i)/10));
%PRESSURE [/10 MPA]
% end
% end

% for i=1:length(p)
% for j=1:length(Fo)
% F(i,j) = (p(i)/10)*b(i,j)^2/(4*pi*n^2)*(3*L(i,j)/b(i,j)-1);
% kr(i,j)=6*F(i,j)/(3*L(i,j)-b(i,j)^2/L(i,j));
% end
%
% figure(1)
% plot(C2*100,flip(F(i,:)),'linewidth',1.5);
% hold on
% grid on
% xlabel('Contraction [%]');
% ylabel('Force [N]');
% title('Force vs. contraction');
% legend('p_1 = 200kPa','p_2 = 400kPa','p_3 = 600kPa');
% legend('Location','best');
% end

for i=1:length(p)
    %determinazione polinomio
    c_F(i,:)=polyfit(k0(i,:),F0,3);
    k_vett(i,:)=linspace(k0(i,1),k0(i,end),N);
    F(i,:)=polyval(c_F(i,:),k_vett(i,:));

    figure(2)
    subplot(3,1,1)
    plot(k0(i,:),F0, 'd', 'linewidth',1.5);
    hold on
    grid on
```

```
    xlabel('k [%]');
    ylabel('Force [N]');
    t=['Force vs. Catalogue contraction -
␣␣␣␣␣␣␣␣Active length = ',num2str(L_muscle) '[mm]'];
    title(t,'fontsize',12,'fontweight','bold');
    legend_parameters=['\fontsize{8}p = ',num2str(p(i)) '\fontsize{8}bar'];
    lgnd(i,1:length(legend_parameters))=legend_parameters;
    legend(lgnd);
    legend('Location','best');

    subplot(3,1,2)
    plot(L_muscle.*k0(i,:)./100,F0, 'd', 'linewidth',1.5);
    hold on
    grid on
    xlabel('\Delta L [mm]');
    ylabel('Force [N]');
    t=['Force vs. Length variation -
␣␣␣␣␣␣␣␣Active length = ',num2str(L_muscle) '[mm]'];
    title(t,'fontsize',12,'fontweight','bold');
    legend_parameters=['\fontsize{8}p = ',num2str(p(i)) '\fontsize{8}bar'];
    lgnd(i,1:length(legend_parameters))=legend_parameters;
    legend(lgnd);
    legend('Location','best');

    subplot(3,1,3)
    plot(L_muscle.*(1-(k0(i,:)./100)),F0, 'd', 'linewidth',1.5);
    hold on
    grid on
    xlabel('L [mm]');
    ylabel('Force [N]');
    t=['Force vs. Length -
␣␣␣␣␣␣␣␣Active length = ',num2str(L_muscle) '[mm]'];
    title(t,'fontsize',12,'fontweight','bold');
    legend_parameters=['\fontsize{8}p = ',num2str(p(i)) '\fontsize{8}bar'];
    lgnd(i,1:length(legend_parameters))=legend_parameters;
    legend(lgnd);
    legend('Location','best');
end

for i=1:length(p)
    figure(2)
    subplot(3,1,1)
    plot(k_vett(i,:),F(i,:), '--k', 'linewidth',1.5);
    legend_parameters=['\fontsize{8}p = ',num2str(p(i)) '\fontsize{8}bar'];
    lgnd(i,1:length(legend_parameters))=legend_parameters;
    legend(lgnd);
    legend('Location','best');

    subplot(3,1,2)
    plot(L_muscle.*k_vett(i,:)./100,F(i,:), '--k', 'linewidth',1.5);
```

```
    hold on
148 grid on
    xlabel('\Delta L [mm]');
150 ylabel('Force [N]');
    t=['Force vs. Length variation -
152 Active length = ',num2str(L_muscle) '[mm]'];
    title(t,'fontsize',12,'fontweight','bold');
154 legend_parameters=['\fontsize{8}p = ',num2str(p(i)) '\fontsize{8}bar'];
    lgnd(i,1:length(legend_parameters))=legend_parameters;
156 legend(lgnd);
    legend('Location','best');
158
    subplot(3,1,3)
160 plot(L_muscle.*(1-(k_vett(i,:)./100)),F(i,:), '--k', 'linewidth',1.5);
    hold on
162 grid on
    xlabel('L [mm]');
164 ylabel('Force [N]');
    t=['Force vs. Length -
166 Active length = ',num2str(L_muscle) '[mm]'];
    title(t,'fontsize',12,'fontweight','bold');
168 legend_parameters=['\fontsize{8}p = ',num2str(p(i)) '\fontsize{8}bar'];
    lgnd(i,1:length(legend_parameters))=legend_parameters;
170 legend(lgnd);
    legend('Location','best');
172 end
clear legend_parameters, clear lgnd, clear t;
174
b= zeros(length(p),N);
176 gamma=90; %degree
c_I=sqrt(c.^2+ras^2); %[mm]
178 beta_I=asin(ras./c_I).*180/pi; %degree

180 for i=1:length(p)
    %definizione triangolo c1
182     r(i,:)= M_pr./F(i,:).*1000; %[mm]
        b(i,:)=sqrt(c_I.^2-r(i,:).^2); %[mm]
184     beta(i,:)=asin(b(i,:)./c_I).*180./pi; %degree
        alpha(i,:)=180-gamma-beta(i,:); %degree
186
        ang_geom(i,:)=theta+beta(i,:)+beta_I-90;
188
        %Rappresentazione geometria com coordinate polari
190     x_th(i,:)=r(i,:).*cos((ang_geom(i,:)).*pi/180); %[mm]
        y_th(i,:)=r(i,:).*sin((ang_geom(i,:)).*pi/180); %[mm]
192
        %ricavo polinomio caratteristico
194     cpol(i,:)=polyfit(x_th(i,:),y_th(i,:),4);
        epol(i,:)=polyval(cpol(i,:),x_th(i,:));
196
```

```
        %calcolo lunghezza curva
198     xlpol=x_th(i,:);
        lpol(i,:)=integral(@(xlpol)sqrt(1+(4.*cpol(i,1).*(xlpol).^3
200 +3.*cpol(i,2).*(xlpol).^2+cpol(i,3).*(xlpol)+cpol(i,4)).^2),xlpol(1),xlpol(end));
        lpol(i,:)=abs(lpol(i,:));
202
        %calcolo variazione utile per contrazione utile del muscolo
204     dl_geomuse(i,:)=(lpol(i)+b(i,1))-(b(i,end));

206     %plot raggio utile per genrazione momento utile
        figure(5)
208     plot(theta,r(i,:),'linewidth',1.5);
        hold on
210     grid on
        xlabel('\theta degree');
212     ylabel('r [mm]');
        title('Useful radius','fontsize',12,'fontweight','bold');
214     legend_parameters=['\fontsize{8}p = ',num2str(p(i)) '\fontsize{8}bar'];
        lgnd(i,1:length(legend_parameters))=legend_parameters;
216     legend(lgnd);
        legend('Location','best');
218
        figure(6)
220     plot(theta,b(i,:),'linewidth',1.5);
        hold on
222     grid on
        xlabel('\theta degree');
224     ylabel('b [mm]');
        title('b variation','fontsize',12,'fontweight','bold');
226     legend_parameters=['\fontsize{8}p = ',num2str(p(i)) '\fontsize{8}bar'];
        lgnd(i,1:length(legend_parameters))=legend_parameters;
228     legend(lgnd);
        legend('Location','best');
230
        figure(7)
232     plot(theta,beta(i,:),'linewidth',1.5);
        hold on
234     grid on
        xlabel('\theta degree');
236     ylabel('\beta degree');
        title('\beta variation','fontsize',12,'fontweight','bold');
238     legend_parameters=['\fontsize{8}p = ',num2str(p(i)) '\fontsize{8}bar'];
        lgnd(i,1:length(legend_parameters))=legend_parameters;
240     legend(lgnd);
        legend('Location','best');
242
        %plot geometria effettiva
244     figure(8)
        plot(x_th(i,:),y_th(i,:),'linewidth',1.5);
246     grid on
```

```
        hold on
        xlabel('x [mm]');
        ylabel('y [mm]');
        title('Resulting geometry','fontsize',12,'fontweight','bold');
        legend_parameters=['\fontsize{8}p = ',num2str(p(i)) '\fontsize{8}bar'];
        lgnd(i,1:length(legend_parameters))=legend_parameters;
        legend(lgnd);
        legend('Location','best');

        %plot approssimazione polinomiale geometria
        figure(9)
        plot(x_th(i,:),epol(i,:),'linewidth',1.5);
        hold on
        grid on
        xlabel('x [mm]');
        ylabel('y [mm]');
        title('Polynomial approximation','fontsize',12,'fontweight','bold');
        legend_parameters=['\fontsize{8}p = ',num2str(p(i)) '\fontsize{8}bar'];
        lgnd(i,1:length(legend_parameters))=legend_parameters;
        legend(lgnd);
        legend('Location','best');
end
clear legend_parameters, clear lgnd, clear t;
```

D.9 Shadow Robot Muscle - Experimental SET1

```
%Data Sheet 20mm BPA muscle
clear all
close all
clc

%Gometric Data
D_muscle = 20; %[mm]
W = 40; %[g] weight approx.
n=2.5; %number of turns
A=243.8; %[g] rod weight

%Forces
F0 = round([1066+A 1066+1074+A 1066+1074+1101+A
                1066+1074+1101+1017+A
                1066+1074+1101+1017+1044+A].*9.81.*10^-3); %[N]

%Pressures
p=[0 0.5 1.0 1.5 2.0 2.5 3.0]; %bar

%Length variation
L=zeros(length(p),length(F0));
L(1,:) =[22.9 24.6 24.8 24.9 25].*10; %[mm]
L(2,:)=[20.3 20.35 20.5 21 21.25].*10; %[mm]
```

```
L(3,:)=[18.9 18.95 18.98 19.2 19.4].*10; %[mm]
L(4,:)=[18.15 18.3 18.4 18.6 18.7].*10; %[mm]
L(5,:)=[17.9 18 18.05 18.2 18.3].*10; %[mm]
L(6,:)=[17.8 17.84 17.89 17.9 18.05].*10; %[mm]
L(7,:)=[17.6 17.7 17.75 17.8 17.85].*10; %[mm]

%muscle length
L_active=L(1,end); %[mm]

%Contractions
C=zeros(length(p),length(F0));
C(1,:)=(1 - L(1,:)./L_active).*100; %[%]
C(2,:)=(1 - L(2,:)./L_active).*100; %[%]
C(3,:)=(1 - L(3,:)./L_active).*100; %[%]
C(4,:)= (1 - L(4,:)./L_active).*100; %[%]
C(5,:)= (1 - L(5,:)./L_active).*100; %[%]
C(6,:)= (1 - L(6,:)./L_active).*100; %[%]
C(7,:)= (1 - L(7,:)./L_active).*100; %[%]

% %contractions variations
% dL=zeros(length(p),length(F0));
% dL(1,:)=L(1,1).*linspace(C(1,1),C(1,end),N);
% dL(2,:)=L(1,2).*linspace(C(2,1),C(2,end),N);
% dL(3,:)=L(1,3).*linspace(C(3,1),C(3,end),N);
% dL(4,:)=L(1,4).*linspace(C(4,1),C(4,end),N);
% dL(5,:)=L(1,5).*linspace(C(5,1),C(5,end),N);
% dL(6,:)=L(1,6).*linspace(C(6,1),C(6,end),N);
% dL(7,:)=L(1,7).*linspace(C(7,1),C(7,end),N);

for i=1:length(p)
    figure(1)
    subplot(2,1,1)
    plot(C(i,:),F0, 'd', 'linewidth',1.5);
    hold on
    grid on
    xlabel('k [%]');
    ylabel('F [N]');
    t=['Force vs. Contractions - Experimental data'];
    title(t,'fontsize',12,'fontweight','bold');
    legend_parameters=['\fontsize{8}p = ',num2str(p(i)) '\fontsize{8}bar'];
    lgnd(i,1:length(legend_parameters))=legend_parameters;
    legend(lgnd);
    legend('Location','best');

    subplot(2,1,2)
    plot(L(i,:),F0, 'd', 'linewidth',1.5);
    hold on
    grid on
    xlabel('L [mm]');
    ylabel('F [N]');
```

```
    t=['Force␣vs.␣Lengths␣-␣Experimental␣data'];
75  title(t,'fontsize',12,'fontweight','bold');
    legend_parameters=['\fontsize{8}p␣=␣',num2str(p(i)) '\fontsize{8}bar'];
77  lgnd(i,1:length(legend_parameters))=legend_parameters;
    legend(lgnd);
79  legend('Location','best');
end
```

D.10 Shadow Robot Muscle - Experimental SET2

```
%Data Sheet 20mm BPA muscle
clear all
close all
clc

%Dati INPUT

%Gometric Data
D_muscle = 20; %[mm]
W = 40; %[g] weight approx.
n=2.5; %number of turns
A=243.8; %[g] rod weight

%Forces
F0 = round([1066+A 1066+1074+A 1066+1074+1101+A
                    1066+1074+1101+1017+A
                    1066+1074+1101+1017+1044+A].*9.81.*10^-3); %[N]

%Pressures
p=[0 0.5 1 1.5 2 2.5 3]; %bar

%Length variation
L=zeros(length(p),length(F0));
L(1,:) =[22.9 24.6 24.8 24.9 25].*10; %[mm]
L(2,:)=[19.6 20 20.3 20.6 20.9].*10; %[mm]
L(3,:)=[18.6 18.9 19.2 19.4 19.6].*10; %[mm]
L(4,:)=[18.1 18.3 18.5 18.7 18.9].*10; %[mm]
L(5,:)=[17.9 17.95 18.1 18.2 18.3].*10; %[mm]
L(6,:)=[17.65 17.75 17.85 17.95 18].*10; %[mm]
L(7,:)=[17.4 17.5 17.6 17.7 17.75].*10; %[mm]

%muscle length
L_active=L(1,end); %[mm]

%Contractions
C=zeros(length(p),length(F0));
C(1,:)=(1 - L(1,:)./L_active).*100; %[%]
C(2,:)=(1 - L(2,:)./L_active).*100; %[%]
C(3,:)=(1 - L(3,:)./L_active).*100; %[%]
C(4,:)= (1 - L(4,:)./L_active).*100; %[%]
C(5,:)= (1 - L(5,:)./L_active).*100; %[%]
C(6,:)= (1 - L(6,:)./L_active).*100; %[%]
C(7,:)= (1 - L(7,:)./L_active).*100; %[%]

% %contractions variations
% dL=zeros(length(p),length(F0));
% dL(1,:)=L(1,1).*linspace(C(1,1),C(1,end),N);
% dL(2,:)=L(1,2).*linspace(C(2,1),C(2,end),N);
```

```
% dL(3,:)=L(1,3).*linspace(C(3,1),C(3,end),N);
% dL(4,:)=L(1,4).*linspace(C(4,1),C(4,end),N);
% dL(5,:)=L(1,5).*linspace(C(5,1),C(5,end),N);
% dL(6,:)=L(1,6).*linspace(C(6,1),C(6,end),N);
% dL(7,:)=L(1,7).*linspace(C(7,1),C(7,end),N);

for i=1:length(p)
    figure(1)
    subplot(2,1,1)
    plot(C(i,:),F0, 'd', 'linewidth',1.5);
    hold on
    grid on
    xlabel('k [%]');
    ylabel('F [N]');
    t=['Force vs. Contractions - Experimental data'];
    title(t,'fontsize',12,'fontweight','bold');
    legend_parameters=['\fontsize{8}p = ',num2str(p(i)) '\fontsize{8}bar'];
    lgnd(i,1:length(legend_parameters))=legend_parameters;
    legend(lgnd);
    legend('Location','best');

    subplot(2,1,2)
    plot(L(i,:),F0, 'd', 'linewidth',1.5);
    hold on
    grid on
    xlabel('L [mm]');
    ylabel('F [N]');
    t=['Force vs. Lengths - Experimental data'];
    title(t,'fontsize',12,'fontweight','bold');
    legend_parameters=['\fontsize{8}p = ',num2str(p(i)) '\fontsize{8}bar'];
    lgnd(i,1:length(legend_parameters))=legend_parameters;
    legend(lgnd);
    legend('Location','best');
end
\end
```

D.11 Shadow Robot Muscle - SET1 vs. SET2

```
%SET 1 vs SET 2
%pressures 2, 4 and 6
clear all
close all
clc

%Gometric Data
D_muscle = 20; %[mm]
W = 40; %[g] weight approx.
n=2.5; %number of turns
A=243.8; %[g] rod weight
N=200;

%Forces
F0 = round([1066+A 1066+1074+A 1066+1074+1101+A
                    1066+1074+1101+1017+A
                    1066+1074+1101+1017+1044+A].*9.81.*10^-3); %[N]

%Pressures
p=[1.0 2.0 3.0]; %bar

%Characteristic length
L_0 =[22.9 24.6 24.8 24.9 25].*10; %[mm]
%muscle length
L_active=L_0(1,end); %[mm]
C_0=(1 - L_0./L_active).*100; %[%]


%SET1
%Length variation
Ls1=zeros(length(p),length(F0));
Ls1(1,:)=[18.9 18.95 18.98 19.2 19.4].*10; %[mm]
Ls1(2,:)=[17.9 18 18.05 18.2 18.3].*10; %[mm]
Ls1(3,:)=[17.6 17.7 17.75 17.8 17.85].*10; %[mm]

%Contractions
Cs1=zeros(length(p),length(F0));
Cs1(1,:)=(1 - Ls1(1,:)./L_active).*100; %[%]
Cs1(2,:)= (1 - Ls1(2,:)./L_active).*100; %[%]
Cs1(3,:)= (1 - Ls1(3,:)./L_active).*100; %[%]

%SET2
%Length variation
Ls2=zeros(length(p),length(F0));
Ls2(1,:)=[18.6 18.9 19.2 19.4 19.6].*10; %[mm]
Ls2(2,:)=[17.9 17.95 18.1 18.2 18.3].*10; %[mm]
Ls2(3,:)=[17.4 17.5 17.6 17.7 17.75].*10; %[mm]
```

```
%Contractions
Cs2=zeros(length(p),length(F0));
Cs2(1,:)=(1 − Ls2(1,:)./L_active).*100; %[%]
Cs2(2,:)=(1 − Ls2(2,:)./L_active).*100; %[%]
Cs2(3,:)= (1 − Ls2(3,:)./L_active).*100; %[%]

%PLOT SET1
for i=1:length(p)
    figure(1)
    subplot(2,1,1)
    plot(Cs1(i,:),F0, 'd', 'linewidth',1.5);
    hold on
    grid on
    xlabel('k [%]');
    ylabel('F [N]');
    t=['Force vs. Contractions − SET1 vs. SET2'];
    title(t,'fontsize',12,'fontweight','bold');
    legend_parameters=['\fontsize{8}SET1: p = ',num2str(p(i)) '\fontsize{8}bar'];
    lgnd(i,1:length(legend_parameters))=legend_parameters;
    legend(lgnd);
    legend('Location','best');

    subplot(2,1,2)
    plot(Ls1(i,:),F0, 'd', 'linewidth',1.5);
    hold on
    grid on
    xlabel('L [mm]');
    ylabel('F [N]');
    t=['Force vs. Lengths − SET1 vs. SET2'];
    title(t,'fontsize',12,'fontweight','bold');
    legend_parameters=['\fontsize{8}SET1: p = ',num2str(p(i)) '\fontsize{8}bar'];
    lgnd(i,1:length(legend_parameters))=legend_parameters;
    legend(lgnd);
    legend('Location','best');

    %determinazione polinomio contrazioni
    c_F1(i,:)=polyfit(Cs1(i,:),F0,3);
    k_vett1(i,:)=linspace(Cs1(i,1),Cs1(i,end),N);
    F1(i,:)=polyval(c_F1(i,:),k_vett1(i,:));

    %determinazione polinomio variazioni lunghezze
    L_F1(i,:)=polyfit(Ls1(i,:),F0,3);
    L_vett1(i,:)=linspace(Ls1(i,1),Ls1(i,end),N);
    F_L1(i,:)=polyval(L_F1(i,:),L_vett1(i,:));
end

%PLOT SET2

for i=1:length(p)
    figure(1)
```

```
99      subplot(2,1,1)
        plot(Cs2(i,:),F0, 'd', 'linewidth',1.5);
101     hold on
        grid on
103     xlabel('k [%]');
        ylabel('F [N]');
105     t=['Force vs. Contractions - SET1 vs. SET2'];
        title(t,'fontsize',12,'fontweight','bold');
107     legend_parameters=['\fontsize{8}SET2: p = ',num2str(p(i)) '\fontsize{8}bar'];
        lgnd(i+3,1:length(legend_parameters))=legend_parameters;
109     legend(lgnd);
        legend('Location','best');
111
        subplot(2,1,2)
113     plot(Ls2(i,:),F0, 'd', 'linewidth',1.5);
        hold on
115     grid on
        xlabel('L [mm]');
117     ylabel('F [N]');
        t=['Force vs. Lengths - SET1 vs. SET2'];
119     title(t,'fontsize',12,'fontweight','bold');
        legend_parameters=['\fontsize{8}SET2: p = ',num2str(p(i)) '\fontsize{8}bar'];
121     lgnd(i+3,1:length(legend_parameters))=legend_parameters;
        legend(lgnd);
123     legend('Location','best');

125     %determinazione polinomio contrazioni
        c_F2(i,:)=polyfit(Cs2(i,:),F0,3);
127     k_vett2(i,:)=linspace(Cs2(i,1),Cs2(i,end),N);
        F2(i,:)=polyval(c_F2(i,:),k_vett2(i,:));
129
        %determinazione polinomio variazioni lunghezze
131     L_F2(i,:)=polyfit(Ls2(i,:),F0,3);
        L_vett2(i,:)=linspace(Ls2(i,1),Ls2(i,end),N);
133     F_L2(i,:)=polyval(L_F2(i,:),L_vett2(i,:));
    end
135
        for i=1:length(p)
137     figure(1)
        subplot(2,1,1)
139     plot(k_vett1(i,:),F1(i,:), '--k', 'linewidth',1.5);
        hold on
141     grid on
        legend_parameters=['\fontsize{8}SET1: p = ',num2str(p(i)) '\fontsize{8}bar'];
143     lgnd(i,1:length(legend_parameters))=legend_parameters;
        legend(lgnd);
145     legend('Location','best');

147     subplot(2,1,2)
        plot(L_vett1(i,:),F_L1(i,:), '--k', 'linewidth',1.5);
```

```
149     hold on
        grid on
151     legend_parameters=['\fontsize{8}SET1: p = ',num2str(p(i)) '\fontsize{8}bar'];
        lgnd(i,1:length(legend_parameters))=legend_parameters;
153     legend(lgnd);
        legend('Location','best');
155
        subplot(2,1,1)
157     plot(k_vett2(i,:),F2(i,:), 'k', 'linewidth',1.5);
        hold on
159     grid on
        legend_parameters=['\fontsize{8}SET2: p = ',num2str(p(i)) '\fontsize{8}bar'];
161     lgnd(i+3,1:length(legend_parameters))=legend_parameters;
        legend(lgnd);
163     legend('Location','best');

165     subplot(2,1,2)
        plot(L_vett2(i,:),F_L2(i,:), 'k', 'linewidth',1.5);
167     hold on
        grid on
169     legend_parameters=['\fontsize{8}SET2: p = ',num2str(p(i)) '\fontsize{8}bar'];
        lgnd(i+3,1:length(legend_parameters))=legend_parameters;
171     legend(lgnd);
        legend('Location','best');
173 end
    clear legend_parameters, clear lgnd, clear t;
```

D.12 Articulated Mechanism - Modeling

```
clear all
close all
clc

%Dati INPUT
L_muscle=400; %mm
p=[100, 200, 300, 400, 500, 600]; %kPa
ck=[0 3 8 8 8 8]; %coeff. contrazione:
%definisce forza massima e minima ottenuta dalla contrazione utile
N=500; %punti approx
np=3; %pressione di lavoro bar (scegliere 1-6 bar)

%Body Data Age 30
g = 9.81; %m/s^2
body_mass=70; %Kg
body_size=1.72; %m
theta_max=180; %degree
dtheta=200*pi/180; %rad/s
ddtheta=dtheta/0.2; %rad/s^2

%Calcutation of Arm Moment
[Mdtg, theta, Ixx, Iyy, Izz]= muscleFM(body_mass, body_size,
        g, N, theta_max, dtheta, ddtheta); %[Nm]
Mdtg=Mdtg;

theta=linspace(0,theta_max,N).*pi./180; %rad

% %Dati molla
% np=5; %numero molle in parallelo
% dy=10; %mm
% dy_r=3; %mm
% k=12; %N/mm
% y_e=linspace(dy,dy_r,N); %mm
% F=np.*k.*y_e; %N

%coeff. caratteristica muscolo
a1=0.11210;
a2=263.700;
a3=-0.35150;
a4=-0.08619;
a5=2.62400;
a6=-245.60;

% Contrazioni Originali
ko(1,:)=linspace(0, 5.96, N);
ko(2,:)=linspace(0, 16, N);
ko(3,:)=linspace(0, 20.96, N);
ko(4,:)=linspace(0, 23.33, N);
```

```
ko(5,:)=linspace(0, 24.75, N);
ko(6,:)=linspace(0, 25.70, N);

%sistema 1: biella manovella
r=0.06; %m
l11=0.08; %m
beta=asin(r./l11.*sin(theta)); %rad
dbeta=dtheta.*(r./l11).*(cos(theta)./cos(beta)); %rad/s
ddbeta=(dbeta.^2.*l11.*sin(beta)-dtheta.^2.*r.*sin(theta))./(l11.*cos(beta));
%rad/s^2
y_B_max=l11+r-(l11-r); %m
y_B=(r+l11)-(r.*cos(theta)+l11.*cos(beta)); %m
dy_B=r.*dtheta.*sin(theta)+l11.*dbeta.*sin(beta); %m/s
ddy_B=ddtheta.*r.*sin(theta)+dtheta.^2.*r.*cos(theta)+ddbeta.*l11.*sin(beta)
        +dbeta.^2.*l11.*cos(beta); %m/s^2

%sistema 2: mecc. traslazione
gamma1_max=48; %degree
gamma1=linspace(0,gamma1_max,N).*pi./180; %rad
l12=y_B_max./sin(gamma1_max.*pi./180); %m
x_C=linspace(0,l12-l12.*cos(gamma1_max.*pi./180),N); %m
dB=l12.*cos(gamma1); %m
dC=l12.*sin(gamma1); %m
dgamma=dy_B./dB; %rad/s
dx_C=dy_B.*dC./dB; %m/s
ddgamma=ddy_B./dB; %rad/s
ddx_C=ddgamma.*dC; %m/s^2

%sistema 3: mecc. pressa
l13=0.07; %m
l23=0.07; %m
x_D=x_C; %m
dx_D=dx_C; %m/s
ddx_D=ddx_C; %m/s^2
phi1=asin(x_D./l13); %rad
[phi1_max, phi1_p]=max(phi1); %rad
dphi1=dx_D./(l13.*cos(phi1)); %rad/s
ddphi1=(ddx_D+l13.*dphi1.^2.*sin(phi1))./(l13.*cos(phi1)); %rad/s^2
phi2=asin(x_D./l23); %rad
[phi2_max, phi2_p]=max(phi2); %rad
dphi2=dx_D./(l23.*cos(phi2)); %rad/s
ddphi2=(ddx_D+l23.*dphi2.^2.*sin(phi2))./(l23.*cos(phi2)); %rad/s^2
y_D=l13.*cos(phi1); %m
dy_D=-dphi1.*l13.*sin(phi1); %m/s
ddy_D=-ddphi1.*l13.*sin(phi1)-dphi1.^2.*l13.*cos(dphi1); %m/s^2
y_F=l13+l23-(l13.*cos(phi1)+l23.*cos(phi2)); %m
dy_F=l13.*dphi1.*sin(phi1)+l23.*dphi2.*sin(phi2); %m/s
ddy_F=l13.*ddphi1.*sin(phi1)+l13.*dphi1.^2.*cos(phi1)+l23.*ddphi2.^2.*sin(phi2)
        +l23.*dphi2.^2.*cos(phi1); %m/s^2
[y_Fmax,y_Fpmax]=max(y_F); %m
```

```
[y_Fmin,y_Fpmin]=min(y_F); %m
Dy_F=linspace(0,y_Fmax-y_Fmin,N); %m

%calcolo variazione lunghezza per contrazione massima utile del muscolo
k_max=(y_Fmax-y_Fmin)*1000*100/L_muscle; %mm
k=zeros(length(p),N);

%Contrazioni utili (range utile di lavoro del muscolo)
k(1,:)=linspace(ko(1,end)-k_max-ck(1), ko(1,end)-ck(1), N);
k(2,:)=linspace(ko(2,end)-k_max-ck(2), ko(2,end)-ck(2), N);
k(3,:)=linspace(ko(3,end)-k_max-ck(3), ko(3,end)-ck(3), N);
k(4,:)=linspace(ko(4,end)-k_max-ck(4), ko(4,end)-ck(4), N);
k(5,:)=linspace(ko(5,end)-k_max-ck(5), ko(5,end)-ck(5), N);
k(6,:)=linspace(ko(6,end)-k_max-ck(6), ko(6,end)-ck(6), N);

%variazione utile lunghezza muscolo
dL_muscle_useful=L_muscle*k/100;
lg=1; %contatore per leggenda
for i=1:length(p)
    if (ko(i,end)-k_max)>0
     for j=1:N
          F(i,j) = (a1*p(i)+a2)*exp(a3*k(i,j))+(a4*p(i)*k(i,j))+a5*p(i)+a6;
          if F(i,j)<0
               F(i,j)=0;
          end
     end

          figure(1)
          plot(k(i,:),F(i,:),'linewidth',1.5);
          hold on
          grid on
          xlabel('Contraction [%]');
          ylabel('Force [N]');
          t_uc=['Force vs. Useful contraction -
        Active length = ',num2str(L_muscle) ' [mm]'];
          title(t_uc,'fontsize',12,'fontweight','bold');
          legend_parameters=['\fontsize{8}p = ',num2str(p(i)) '\fontsize{8}kPa'];
          lgnd(lg,1:length(legend_parameters))=legend_parameters;
          legend(lgnd);
          legend('Location','best');

          [dLm_MAX, dLm_MP]=max(dL_muscle_useful(i,:));
          [dLm_min, dLm_mp]=min(dL_muscle_useful(i,:));
          dLm=dLm_MAX-dLm_min;

          figure(2)
          plot(dL_muscle_useful(i,:),F(i,:),'linewidth',1.5);
          hold on
          grid on
          xlabel('\DeltaL [mm]');
```

```
            ylabel('Force [N]');
150         t_ul=['Force vs. Useful length variation
        Muscle active length = ',num2str(L_muscle) '[mm]'];
152         title(t_ul,'fontsize',12,'fontweight','bold');
            legend(lgnd);
154         legend('Location','best');
            lg=lg+1;
156         fprintf('Muscle length variation %g mm for p = %g kPa\n',dLm, p(i));
        else
158     end
    end
160 clear legend_parameters, clear lgnd, clear t;

162 %componenti utili
    Oc=F(np,:).*(tan(phi1)+tan(phi2)); %N
164 Vb=Oc.*tan(gamma1); %N

166 %Momento resistente su sistema biella manovella
    Mr=Vb.*r.*sin(theta).*(1+r.*cos(theta).
168         /(l11.*sqrt(1-(r./l11).^2.*(sin(theta)).^2))); %Nm

170 theta=theta.*180./pi;
    figure(3)
172 plot(theta,Mr,'linewidth',1.5);
    hold on
174 grid on
    plot(theta,Mdtg,'linewidth',1.5);
176 xlabel('\theta [degree]');
    ylabel('M [Nm]');
178 t=['Torques vs. Angle'];
    title(t,'fontsize',12,'fontweight','bold');
180 legend('Torque compensation', 'Moment due to gravity', 'Location','best');

182 Mgc=Mdtg-Mr;

184 figure(4)
    plot(theta,Mgc,'linewidth',1.5);
186 hold on
    grid on
188 xlabel('\theta [degree]');
    ylabel('Result moment [Nm]');
190 t=['Result torque vs. Angle'];
    title(t,'fontsize',12,'fontweight','bold');
192
    figure(5)
194 subplot(3,1,1)
    plot(theta,y_B,'k','linewidth',1.5);
196 hold on;
    grid on;
198 xlabel('\theta [degree]');
```

```
ylabel('y_B [m]');
title('Point B displacement','fontsize',12,'fontweight','bold');
subplot(3,1,2)
plot(theta,dy_B,'b','linewidth',1.5);
hold on;
grid on;
xlabel('\theta [degree]');
ylabel('dy_B [m/s]');
title('Point B velocity','fontsize',12,'fontweight','bold');
subplot(3,1,3)
plot(theta,ddy_B, 'r', 'linewidth',1.5);
hold on;
grid on;
xlabel('\theta [degree]');
ylabel('ddy_B [m/s^2]');
title('Point B acceleration','fontsize',12,'fontweight','bold');

figure(6)
subplot(3,1,1)
plot(theta,y_F,'k','linewidth',1.5);
hold on;
grid on;
xlabel('\theta [degree]');
ylabel('y_F [m]');
title('Point F displacement','fontsize',12,'fontweight','bold');
subplot(3,1,2)
plot(theta,dy_F,'b','linewidth',1.5);
hold on;
grid on;
xlabel('\theta [degree]');
ylabel('dy_F [m/s]');
title('Point F velocity','fontsize',12,'fontweight','bold');
subplot(3,1,3)
plot(theta,ddy_F, 'r', 'linewidth',1.5);
hold on;
grid on;
xlabel('\theta [degree]');
ylabel('ddy_F [m/s^2]');
title('Point F acceleration','fontsize',12,'fontweight','bold');

% figure(3)
% plot(y_e,F,'linewidth',1.5);
% hold on
% grid on
% xlabel('y [mm]');
% ylabel('Fm [N]');
% t=['Elastic force vs. desplacement'];
% title(t,'fontsize',12,'fontweight','bold');
```